5-17-2013

Through Wafer 3D Vertical Micro-Coaxial Probe for High Frequency Material Characterization and Millimeter Wave Packaging Systems

Justin Boone
jboon007@fiu.edu

DOI: 10.25148/etd.FI13080505

FLORIDA INTERNATIONAL UNIVERSITY

Miami, Florida

THROUGH WAFER 3D VERTICAL MICRO-COAXIAL PROBE FOR HIGH FREQUENCY MATERIAL CHARACTERIZATION AND MILLIMETER WAVE PACKAGING SYSTEMS

A dissertation submitted in partial fulfillment of

the requirements for the degree of

DOCTOR OF PHILOSOPHY

in

ELECTRICAL ENGINEERING

by

Justin Boone

2013

To: Dean Amir Mirmiran
College of Engineering and Computing

This dissertation, written by Justin Boone, and entitled Through Wafer 3D Vertical Micro-Coaxial Probe for High Frequency Material Characterization and Millimeter Wave Packaging Systems, having been approved in respect to style and intellectual content, is referred to you for judgment.

We have read this dissertation and recommend that it be approved.

Stavros Georgakopoulos

Jean Andrian

Kinzy Jones

Lorenzo Ponce de Leon

James Mihelcic

Shekhar Bhansali, Major Professor

Date of Defense: May 17, 2013

The dissertation of Justin Boone is approved.

Dean Amir Mirmiran
College of Engineering and Computing

Dean Lakshmi N. Reddi
University Graduate School

Florida International University, 2013

DEDICATION

This is dedicated to my sister, grandmother, and parents for their unconditional love and inspiration.

ACKNOWLEDGMENTS

I would like to thank my major professor, Dr. Shekhar Bhansali, for providing with the excellent opportunity to work on my Doctorate degree. His innovative ideas, motivation, and support were a tremendous help in developing me into the researcher I am today. I would also like to give special thanks to my mentor, Dr. Subramanian Krishnan, who deserves all of the credit for guiding me throughout this entire process; whether it was providing recommendations for next steps in my research, to fully supporting and motivating me during the most difficult times. I have learned a lot from him both professionally and personally and will forever be thankful. I would also like to thank Dr. Stavros Georgakopoulos, Dr. Kinzy Jones, Dr. Jean Andrian, and Dr. Lorenzo PoncedeLeon for serving as my committee members. I would also like to thank Dr. James Mihelcic for serving on my committee as well as providing me with unconditional support since my undergraduate studies.

Special thanks go to my friends the "Fantastic Four" from Southern University A&M College – Brandon, Eric, and Frank. We have learned so much over the years from one another and I couldn't imagine surviving this process without them. We had a lot of good times and will always have memories to share for a lifetime. I want to also acknowledge the Florida Georgia LSAMP Bridge to Doctorate Award HRD #0929435, National Science Foundation's GRDS Awards ECCS #0925968 and #1203001, and Alfred P. Sloan Minority Ph.D. Program for their financial support during my graduate studies. I am also grateful for the entire Bridge to Doctorate family for their guidance and support.

Words cannot express my love and appreciation for my wonderful mother who continued to motivate me throughout this process and stood by me with patience during rough times. I also want to give special gratitude to my father, stepfather, brother, and best friend who continued to encourage me to strive for excellence. I am indebted to my entire family for their unconditional love, support, and sacrifice. If not for them, I would not have become the man I am today.

ABSTRACT OF THE DISSERTATION

THROUGH WAFER 3D VERTICAL MICRO-COAXIAL PROBE FOR HIGH FREQUENCY MATERIAL CHARACTERIZATION AND MILLIMETER WAVE PACKAGING SYSTEMS

by

Justin Boone

Florida International University, 2013

Miami, Florida

Professor Shekhar Bhansali, Major Professor

This work presents the development of an in-plane vertical micro-coaxial probe using bulk micromachining technique for high frequency material characterization. The coaxial probe was fabricated in a silicon substrate by standard photolithography and a deep reactive ion etching (DRIE) technique. The through-hole structure in the form of a coaxial probe was etched and metalized with a diluted silver paste. A co-planar waveguide configuration was integrated with the design to characterize the probe. The electrical and RF characteristics of the coaxial probe were determined by simulating the probe design in Ansoft's High Frequency Structure Simulator (HFSS). The reflection coefficient and transducer gain performance of the probe was measured up to 65 GHz using a vector network analyzer (VNA). The probe demonstrated excellent results over a wide frequency band, indicating its ability to integrate with millimeter wave packaging systems as well as characterize unknown materials at high frequencies.

The probe was then placed in contact with 3 materials where their unknown permittivities were determined. To accomplish this, the coaxial probe was placed in contact with the material under test and electromagnetic waves were directed to the surface using the VNA, where its reflection coefficient was then determined over a wide frequency band from dc-to -65GHz. Next, the permittivity of each material was deduced from its measured reflection coefficients using a cross ratio invariance coding technique. The permittivity results obtained when measuring the

reflection coefficient data were compared to simulated permittivity results and agreed well. These results validate the use of the micro-coaxial probe to characterize the permittivity of unknown materials at high frequencies up to 65GHz.

TABLE OF CONTENTS

LIST OF TABLES

TABLE PAGE

LIST OF FIGURES

FIGURE PAGE

CHAPTER 1

INTRODUCTION

1.1 High Frequency Material Characterization for Microwave Electronics

The responses of materials to electromagnetic fields are determined by the displacement of free and bounded electrons and by the orientation of their atomic moments (magnetic fields) [1]. Furthermore, by applying microwave signals to materials under test, electrical properties of these materials can be determined at higher frequencies [2]. As a result, characterizing materials properties at high frequencies using microwave methods has a long history dating back to the early 1950's and has now been used in a variety of applications ranging from communication devices to military satellite services such as: antennas, micro-sensor systems, ground penetrating radars (GPR), printed circuit board (PCB) applications, etc [3-8]. In recent years, the development of high-speed, high-frequency circuits and systems require complete understanding of materials functioning at high frequencies [1]. Additionally, as communication and broadband technologies rapidly evolve, traditional FR-4 materials may no longer behave well in the high frequency range due to the increase in signal loss and transmission delays [3]. These numerous aspects make the characterization of materials properties at high frequencies an important field of study in microwave electronics. Figure 1.1 illustrates the concept of material characterization using microwave methods [9].

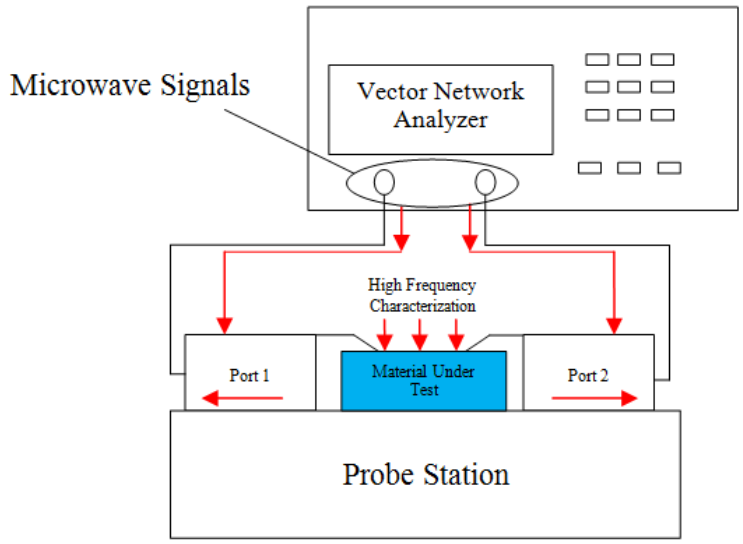

Figure 1.1 Illustration of High Frequency Material Characterization using Microwave Methods.

1.2 Current Methods of Microwave Material Characterization

Microwave methods for materials characterization generally fall into two categories: non-resonant methods and resonant methods. Figure 1.2 (a) and (b) illustrates examples for the two methods of material characterization at microwave frequencies. Non-resonant methods are often used to get general knowledge of electromagnetic properties over a frequency range [10]. Resonant methods are used to get accurate knowledge of dielectric properties at a single frequency or several discrete frequencies [11]. The two methods are also often used in combination for complete accuracy. By modifying the general knowledge over a certain frequency range obtained from the non-resonant method with the accurate knowledge at several frequencies obtained from the resonant method, accurate knowledge of materials properties over a frequency range can be obtained. However, this work is focused on the non-resonant method due to the increasing demand for determining the electromagnetic properties of materials at high frequencies over a wide bandwidth.

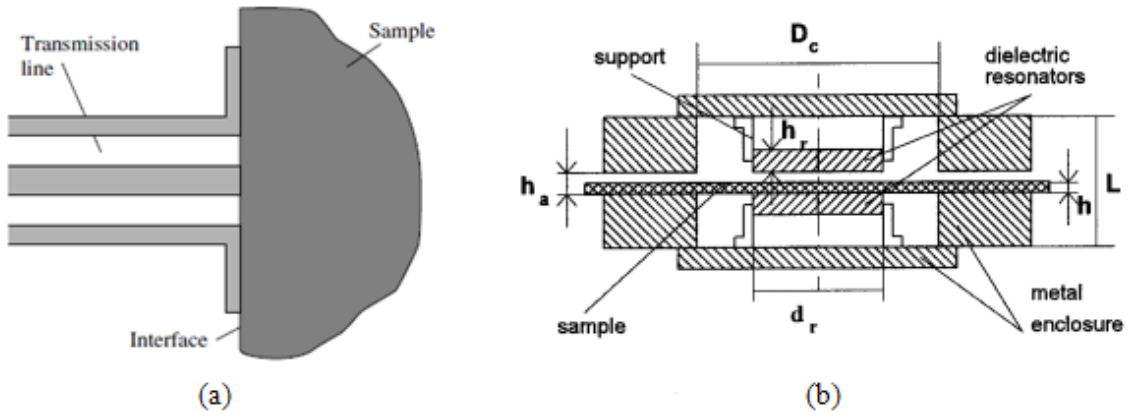

Figure 1.2 Example illustrations of (a) Open Circuit Reflection Method [1](Non-Resonant) and (b) Split Resonator Method [12] (Resonant) for microwave material characterization.

1.2.1 Non-Resonant Methods

The non-resonant methods for microwave material characterization consist of reflection and transmission/reflection. In the reflection method, electromagnetic waves are directed to a material under test (MUT), and its properties are deduced from the reflection coefficient at a defined reference plane. In the transmission/reflection method, the material under test is placed in a piece of transmission line and its properties are deduced from the reflection of the material and transmission through the material. Under the reflection method either the permittivity or permeability of a material can be determined; whereas in the reflection/transmission method both permittivity and permeability can be deduced. Only the reflection coefficients of the MUT's in this work were deduced; therefore the reflection method was utilized.

To determine the reflection coefficient of a MUT, researchers have developed the use of coaxial probes [13, 14]. These probes consist of an inner diameter made of a conductor and an outer diameter made of a dielectric. A final outer conductor is also used which surrounds the outer dielectric and acts as a ground connection. Figure 1.3 shows an example of a coaxial probe being used for high frequency material characterization. In this approach, the coaxial probe is placed on the MUT and the reflection coefficient is determined by applying a signal to the inner

conductor from a microwave source. Although this probe method does provide an ease of measurement and durability when applied to rough surfaces due to its non-invasive approach, it has produced the need for improvement in several different aspects. For example, reducing the size of the probe can increase the frequency range of characterization, but can create extreme fabrication issues on the device. Other areas suggest the need for improvement of the probes when determining the properties of a material over larger surface areas; which would increase the need for larger input/output ratios of coaxial probes within a device structure [15]. Another important aspect is the high cost for current material characterization methods; which requires companies to pay an expensive rate for each measurement taken due to the high cost of equipment. These areas of improvement introduces the need to develop a low-cost coaxial probe on the micro/nano scale, that can be easily fabricated, capable of producing high I/O ratios, and compatible with commercial devices. In addition, designing the probe to also be used in millimeter wave packaging systems introduces its dual capabilities for a variety of future commercial application. A detailed overview on different coaxial probe techniques used for high frequency material characterization is presented in the next chapter.

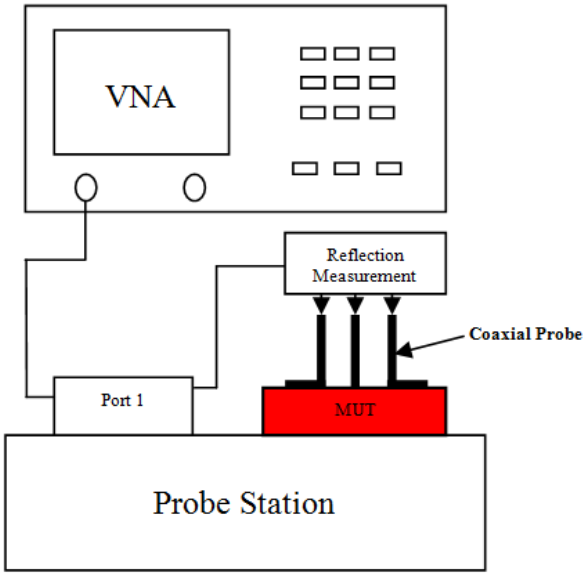

Figure 1.3 Illustration of Coaxial Probe being used for high frequency material characterizations.

1.3 Goals and Objectives

The primary objective of this research work is to develop through wafer 3D Vertical Micro-Coaxial Probe for high frequency material characterization and millimeter wave packaging systems. The following goals were identified as being pertinent to achieving the objective.

(a) To determine a suitable model and design for the vertical micro-coaxial probe. A probe design has to be developed based on the calculated RF specifications for its selected range of frequency. To function at high frequencies, the electrical length of the probe should be kept as short as possible.

(b) To simulate the behavior and RF characteristics of the coaxial probe. The reflection coefficient and transducer gain of the coaxial probe has to be simulated over the desired frequency band using a software simulator. Understanding the RF performance of the probe will provide more accurate measurements of the unknown materials.

(c) To fabricate the micro-coaxial probe using standard photolithography techniques. In order to fabricate the probe, processing techniques will be used such as: Deep Reactive Ion Etching, Photolithography, Electron Beam Deposition, and a novel metallization process.

(d) To perform RF characterization of probe by determining its signal transmission capabilities – The reflection coefficient and transducer gain of the probe has to be measured using microwave methods and instrumentation. The measurement setup will include a probe station, 67 GHz coplanar waveguide probes, a V-band cable, and a vector network analyzer. These results will verify the probes ability to be used as vertical transitions and integrated with millimeter wave packaging systems.

(e) To integrate the micro-coaxial probe with unknown high frequency materials for characterization. In order to determine the permittivity of the unknown materials, the probe has to be coupled to the materials and its reflection coefficients can be deduced from measuring. Once

the reflection data of the materials are determined, the permittivity of the unknown materials is extracted using a cross-ratio variance method.

To accomplish the aforementioned goals, a 3D vertical micro-coaxial probe with an inner and outer diameter of 100μm and 300μm was designed in a 300 μm thick silicon substrate. Ansys's High Frequency Structure Simulator (HFSS) [16] was used to model and design the coaxial probe. HFSS was also used to simulate the RF characteristics and electrical behavior of the probe; where the reflection coefficient and transducer gain was evaluated from dc-to-67 GHz with a center frequency at 60 GHz. The fabrication of the coaxial probe was achieved using standard photolithography techniques; while the metallization of the probe was accomplished by implementing a novel via filling process. Additionally, a high frequency measurement setup was used verify the probes signal transmission abilities and to measure the reflection data of the unknown materials.

1.4 Dissertation Organization

A brief overview of material characterization followed by a theoretical background of coaxial probes and simulation, fabrication, and measurement techniques for high frequency material characterization is presented in detail.

In Chapter 2, a detailed background study on high frequency characterization of various materials is discussed and the current state of the art for coaxial probes is presented in Chapter 3. In addition, the need for an improved coaxial probe design that can characterize materials at higher frequencies that includes dual capabilities is addressed.

In Chapter 4, the model and the design of the probe are presented; including the theory, simulation, and fabrication of the coaxial probe. The actual probe design and fabrication techniques used in this research are discussed in detail. This chapter also discusses in detail the

RF characterization of the probe including its reflection coefficient and transducer gain using a high frequency setup.

Chapter 5 describes the application of the micro-coaxial probe with unknown materials for high frequency characterization, including the design and explanation of how materials will be characterized using the coaxial probe. The data interpretation of reflection measurements using the cross ratio invariance technique is also discussed in this chapter along with the simulation results of the probe in contact with chosen materials. It also describes the material characterization measurement setup and reports the final results on the measured reflection coefficient of the materials and the extracted permittivity.

Chapter 6 concludes the research work by summarizing the development of the vertical micro-coaxial probe and provides suggestions for future direction of the through wafer probe for material characterization and high frequency packaging applications.

CHAPTER 2

BACKGROUND OF LITERATURE

The concept of using coaxial probes in contact with a variety of materials to characterize its electrical properties at high frequencies has been highly investigated in the past due to the concept of using probes in a non-invasive method [17]. More specifically, this approach has been advantageous in the development of broadband methods used to determine the permittivity of materials at microwave frequencies. Furthermore, this approach of material characterization has led to major research advancements in areas such as: biological tissue characterization, soil characterization, food material characterization, and high frequency material characterization [18-21]. By integrating an open-ended coaxial probe with various tissues and materials, the permittivity of these materials are determined and then used for the development of future commercial applications. This chapter provides detailed descriptions of coaxial probes being used to characterize different materials for a variety of applications.

2.1 Coaxial Probes for Biomedical Material Characterization

In the past, researchers have developed a continuing interest in methods for measuring the permittivity of biological materials at high frequencies. In particular, the characterization of biological tissues and human blood and epidermis at microwave frequencies, has been in high demand as a means to improve diagnosis, detection, and treatment of hazardous cells such as breast cancer [22]. Additionally, knowing the dielectric properties of these biological tissues can be critical for biomedical applications in determining its interaction with electromagnetic waves.

For example, in previous work, researchers used a coaxial probe for broadband microwave characterization of biological tissues in animals and humans [23]. In this work to determine the permittivity, the technique required using distilled water as a reference material. This design utilized an open-ended coaxial line with an outer diameter of 1.45 mm for measuring,

and the MUT was placed on the probe tip for an *in vivo* approach. Next, the probe system was calibrated using the standard open, short, and load to remove all reflections present in the cable over a broad frequency range from 2-to-18 GHz. Then the reflection coefficient of the cable was measured to normalize the system, followed by the calibration of Methanol and distilled water. After calibration, the researchers measured commercial beef and chicken materials to demonstrate the sensitivity of the system prior to testing biological tissues. Lastly, the complex permittivity of normal and malignant breast tissues from the human body were measured between 2 and 18 GHz and then compared to results obtained by previous researchers. The complex permittivities of normal tissues from animals were also measured in this work. Their results confirmed that the measurement technique was successful when compared to other researchers; however, some discrepancies were seen at lower frequencies due to the potential porosity in the normal biological substance. More importantly, the researchers developed a cost effective, non-invasive and easy to use technique for diagnostic and therapeutic applications of microwaves in biomedicine [23]. With this advancement, the researchers produced a fast detecting technique that accurately differentiated between the dielectric properties of normal and cancerous biological tissues.

In [24], researchers analyzed an open-ended coaxial line as a sensor for *in vivo* measurements of the complex permittivity of biological substances. This method integrated the coaxial probe as a sensor with a computer-controlled network analyzer to offer a convenient and accurate measurement technique. The coaxial probe used in their design was selected with an outer diameter of 0.83 cm and was placed in contact with the MUT in a non-destructive manner. Next, to improve the accuracy of the reflection coefficient measurements, the coaxial line sensor was calibrated using a standard error correction procedure [25]. For the probe to be compatible with *in vivo* measurements, the ground plane surrounding the line opening had to be eliminated. This was accomplished placing a flexible metal foil at the end of the line, backed by a thick piece of rubber slab. In this work, distilled water and methanol were also measured as references to

evaluate their method and to estimate any uncertainties in permittivity data. Then, the researchers measured the biological tissues of a female feline (cat) under anesthesia from 10 MHz to 1 GHz. For measuring purposes, various tissues of the cat were surgically exposed such as: skeletal and smooth muscle, liver, kidney, spleen, and pancreas. Results from the obtained permittivities agreed well when compared with reference data. With this design, researchers were able to develop a high speed measurement method for the permittivity of biological tissues, which assisted in the future determination of energy deposition in living subjects. This discovery was essential in evaluating effective and controllable induction of local hyperthermia in the treatment of cancer [24].

Previous researchers have also studied the dielectric properties of freshly excised normal and diseased breast tissue specimens using open ended coaxial probes [26]. This work investigated the sensing volume of two flange-free coaxial probes with diameters of 2.2 mm and 3.5 mm. Both probes were analyzed for low and high-water-content tissue using standard liquids that demonstrated permittivities similar to breast tissues. These tissues were characterized using the coaxial probes in a conventional *in vivo* approach over a microwave frequency range from 1-to-20 GHz. Rather than used traditional solid breast tissue specimens, modeled liquid tissue stimulants such as ethanol, methanol, and deionized water represented low, intermediate, and high values of expected permittivities for breast tissues. To reduce error levels from the measured reflection coefficients of the modeled tissues, an innovative graphical technique was used based on Cole-Cole diagrams. Researchers discovered that tissue specimens with thicknesses of at least 3.0 mm yielded the most accurate measurements with the 3.58-mm-diameter probe. Furthermore, the 2.2-mm-diameter probe demonstrated the most accurate measured results when the specimen thickness was at least 1.5 and 5 mm, respectively. These results revealed that for each probe design, between 1-20 GHz, the above mentioned specimen thicknesses should be used in order to eliminate permittivity errors greater than 10% [26]. Therefore, by employing radio waves or

microwaves to detect the electrical properties of breast tissues via coaxial probes, an even faster and more accurate method to detect the low and high-water-content of a variety of biological tissues was developed. Improving this technology has lead to a more positive approach for the treatment of breast cancer cells.

In other work, the electrical characterization of human blood using an open ended coaxial line was investigated to improve the interaction with biological tissues for diagnosis [27]. This method utilized an equivalent electrical circuit model to represent the coaxial line for measuring. The circuit model was designed to be equivalent to an open ended coaxial probe with inner and outer radii of 1.5 mm and 5 mm respectively. The filling of the probe was chosen to be Teflon, with a dielectric constant of 2.1 and a characteristic admittance of 0.02S. This circuit mainly included capacitances which represented the fringing field effects in the material used to fill the line and in the biological tissue. First, the circuit performance was investigated in regards to frequency and permittivity and then used to measure the performances of human blood from 1 MHz-to-1 GHz. The results obtained when analyzing the behavior of the circuit model revealed the highest error of percentage on the permittivity of the tissues would be 16%. For the conductivity of the tissues, the highest precision level was 8% respectively. This established the variance in the data that might have been seen when characterizing the tissues. Next, the elements of the electrical equivalent circuit were determined using reference liquids such as water, methanol, ethanol, and glycerol. Later, measurements were made on fresh heparined human blood (8000 units per 20ml) at 21˚C using the open ended coaxial line [27]. Results agreed well with the model and demonstrated that precise measurements of dielectric parameters of human blood could be made using the coaxial line with minimal percentage error from 1 MHz-to-1 GHz. These results assisted in the improvement of consistently measuring biological tissues and liquids of human blood at microwave frequencies.

Other advancements in biological tissue characterization using open ended coaxial probes included broadband permittivity measurements of human epidermis (the epidermis: the outer skin layer) [28]. In this approach, a 1 mm diameter coaxial probe was used to help increase measurement bandwidth and to enhance the spatial resolution. This probe dimension allowed the human epidermis to be characterized using microwave measurements up to 110 GHz. Using HP vector network analyzers the measurement system was first calibrated based on cross-ratio transformation with three standard materials: distilled water, methanol, and air. Researchers then used pork to discriminate the permittivities between muscle tissue and fat tissues. To improve the accuracy of the measured tissues, the influence of sample thickness was then studied, where it revealed that the sample thickness should at least be double the length of the coaxial probe. Lastly, the skin permittivity of a human palm and wrist were measured using the 1 mm coaxial probe up to 110 GHz. Both parts of the skin were completely dried for measurements and a total of 10 measurements were taken for the palm and wrist, to provide mean values. Their results revealed that a higher permittivity was obtained for the human wrist than the palm; although, the main difference between the material data was due to their water content and the thickness of the epidermis, which was revealed using a Cole-Cole parameter method. The achieved results helped predict that in order to measure the permittivity of a biological tissue thinner than 1mm a coaxial probe with reduced dimensions is recommended. This work helped explain the reasons for high water content in cells that exist beneath thin epidermis of the wrist and palm skin, which further advanced research for determining the electrical properties of these biological tissues for diagnosis.

2.2 Coaxial Probe for Permittivity of Food Materials

Research advancements have also been made when using the coaxial probe to determine the permittivity or dielectric properties of food materials. Determining these electrical

characteristics proved to be important to investigate these materials when they were exposed to electromagnetic fields during microwave cooking, other RF processes, and microwave dielectric heating [29]. In this work, characterizing these food materials was accomplished using an open-ended coaxial-line probe combined with sample temperature control equipment. By integrating the probe with the temperature equipment, researchers were able to measure the permittivities of liquids, semisolid, and pulverized food materials as a function of frequency and temperature. The permittivities of these materials were measured over a wide frequency range up to 10 GHz from 5˚C to 100˚C using a Hewlett Packard dielectric probe. Each sample was placed in a stainless steel sample cup, 18.95mm inside diameter and 19mm deep, which controlled the temperature of the materials. Next, the permittivities of a homogenized macaroni and cheese dinner, ground whole wheat, and apple juice where measured. The measured results revealed diverse frequency and temperature dependent behavior of the food materials. Furthermore, determining the electrical behavior of these materials, proved to be valuable for further investigations on the influence different forms of water had on food materials, when measurements were taken over wider ranges of frequency and temperature.

2.3 Coaxial Probe for Soil Permittivity Measurements

Another important area of research where coaxial probes have proven to be useful is in determining the permittivity of ground soil, which has been vital for many applications such as precision agriculture [30], geophysics [31], and subsurface sensing [32]. By removing soil samples from the ground and conducting reflectance measurements, researchers are able to determine accurate permittivities at relatively shallow depths.

For example, in previous work, researchers used an in-situ approach with a novel probe design to measure the complex permittivity of soils without removing the samples from the ground [33]. In this method, by eliminating the removal of the soils from the ground, researchers

were able to reduce sample preparation time, cost, and errors due to changes in the soil density. To accomplish this, a pilot hole with a diameter of 1 inch was created in the soil using an auger, and a coaxial probe with the same diameter, was then inserted into the hole at the desired depth to measure the permittivity. To calibrate the measurement system, a cross-ratio invariance technique was used, which required determining the dielectric properties of three known standard materials prior to measuring the soil samples. During calibration however, a thin water layer formed over the soil due to the depth of the hole. This affected the calibration because when the probe was placed at the bottom of the hole, additional reflections appeared from the water layer. To prevent this error, the coaxial opening was placed to the side of the probe were the side wall of the soil which did not have any water present, was measured. Next, the permittivities of soil samples were determined using the coaxial probe from 10 MHz to 1 GHz. The dielectric constant of the soil was determined when a sample was taken inside the small 1-2 inch bored hole. The results revealed that by implementing an improved calibration method, the accuracy of the extracted soil permittivity values improved as well. This improved system can be important for future developments in ground material characterization.

In other efforts, a novel in-situ coaxial probe, created using multi-conductor transmission line, was used to measure the electric and magnetic properties of Hawaiian volcanic soil for ground penetrating radar (GPR) applications in a broadband frequency range from 50 MHz to 1 GHz [34]. The probe was first made by combining two monopole antennas with parasitic elements, into one device to achieve reflection and transmission measurements. The TEM transmission line inside the probe consisted of five conducting rods, two ground plates, and two coaxial feed connectors. The center conductors of both coaxial connectors were coupled by a metal rod with a diameter of 1/8 inch. Unlike traditional calibration methods for an in-situ measurement approach, the probe system then used the S-parameters from sample free and loaded devices to reduce any reflection errors during measuring. Next, soil samples collected at a typical

volcanic red soil are in Oahu, Hawaii were completely dried, and prepared for measuring. A vector network analyzer was then connected to the two-port probe to measure the reflection of the materials over the broad frequency range. Following the reflection measurements, the S-parameters of the soil were converted into complex permittivity values using a unique post processing algorithm. Lastly, the measurement technique and post processing algorithm were both verified and evaluated by numerical simulations, which verified the permittivity results obtained from the volcanic samples. By developing a successful measuring technique combined with a unique processing algorithm to characterize soil materials, advancements have been made that will assist in the investigation of underground environments and objects.

2.4 Coaxial Probe for High Frequency Material Characterization

Additionally, research studies have also been done in the past on the characterization of materials at high frequencies [35, 36]. With the need to determine the electrical properties of materials at microwave frequencies increasing, the ability to generate high frequency data on these samples have became a critical asset for RF designers and microwave products [37]. Characterizing these materials provides information on its temperature tolerance, humidity level, thickness, dielectric constant, and attenuation [38]. Furthermore, being able to measure the dielectric constants of various materials as the frequency range increases, has improved material functionality in applications such as broadband circuit designs, electronic device modules, and micro-electro-mechanical systems sensors.

To accomplish this, researchers have again used a coaxial probe as a method to determine the electrical properties of materials. For example, an open-ended coaxial probe was used to conduct non-destructive measurements on the complex permittivity and permeability of microwave absorbing materials [39]. Researchers used a new frequency-varying method, in which the frequency was varied to measure the reflection coefficient and then to extract its

permittivity. The probe had a diameter of 1.22 mm and consisted of a flange on the end which was used to contact the microwave absorbing sheets. To remove any frequency responses in the test setup, the cross-ratio transformation technique was implemented where the probe system was calibrated using a short-open-liquid calibration procedure. In this process, distilled water was used as a liquid during calibration. The calibration results were then verified by measuring the permittivity of a non-magnetic methanol liquid. Following this, the feasibility of the frequency-varying method was tested by measuring the permittivity of two radar absorbing sheets over a broad frequency range from dc-to-20 GHz. The results proved that the frequency-varying method was successful when measuring the electrical properties of the microwave absorbing materials over a broad frequency range. The success of this study was of vital importance for applications that needed to determine the permittivity of magnetic materials such as ferrite.

In summary, using coaxial probes to characterize materials in areas such as biological tissues, food characterization, soil material characterization, and high frequency material characterization have been investigated and reported. The success of these studies has led to advance development in early cancer cell detection, identifying behavior of food materials when exposed to electromagnetic fields, soil materials for GPR applications, and material characterization for RF and microwave products.

However, this work is mainly focused on using coaxial probes to characterize materials at high frequencies, which will be used in a variety of applications ranging from communication devices to military satellite services such as: antennas, micro-sensor systems printed circuit board (PCB) applications. By applying a microwave signal to the material surface, the electrical properties of each material were determined at high frequencies. The method in this work differs from those mentioned in the above sections, because majority of the coaxial probes used to measure material permittivities were commercially designed and consisted of lengths and diameters in the millimeter range. The 1.2mm probe diameter prevented the probe systems from

measuring beyond 30 GHz, limiting its frequency range of operation. Furthermore, the wide coaxial structure reduced the probing surface area of the material when attempting to measure its electrical behavior. The coaxial probe presented in this work however, was designed in low-cost silicon substrate on a micrometer scale in terms of its length and inner and outer diameters. By reducing the size of the probe, the frequency range of detection increased tremendously, reaching nearly 65 GHz. Additionally, this allowed multiple devices to be fabricated on a single substrate and then used to measure the reflection coefficient of materials at several locations on the surface. This provided a more accurate determination of the materials since its average reflection coefficient values over the entire surface were being used to extract the permittivity. The next chapter discusses in detail, vertical coaxial probes previously designed on a micrometer scale that operate at high frequency levels.

CHAPTER 3

CURRENT STATE OF THE ART

Several vertical coaxial probes have been designed over the past years, as researchers have implemented them in multi-level packaging systems as interconnects and/or transitions. The purpose of the probes in these systems is to successfully transmit RF signals from one package layer to the next. In doing this, the probe device allows the systems to maintain electrical connection in between layers. However, the design of a vertical coaxial probe for use as an interconnect/transition as well as a device to characterize materials at high frequencies, has yet to be investigated.

3.1 Previous Coaxial Probe Designs

For example, a vertical quasi-coaxial structure was designed for 3-D packages using anodized aluminum substrates [40] as shown in Figure 3.1. In this paper, researchers designed a 3-D coaxial structure to evaluate its high frequency performance up to 25 GHz. The design included a coax made of 200μm thick anodized aluminum within a 500μm thick aluminum substrate as the dielectric, and copper as the conductor. The dimensions of the coax included an inner diameter of 300μm and outer diameter of 1mm with a depth of 150μm. This design however, did not include metal on the outer surface of the aluminum. To properly connect the input signal from port 1 directly to port 2, a microstrip-to-coaxial via hole transition was used, which avoided any wire bonding or lead line. The device included two microstrip lines attached to the center metal of the coax and served as the input and output ports. It is important to note that both the coaxial vias and the microstrip lines were formed using electroplating. The design also included a microstrip line on an additional bottom aluminum substrate, which was used to properly transmit an RF signal between ports. This bottom microstrip line was then connected to

port 1 and 2 using solder balls, whereas the top and bottom substrate layers were connected using flip-chip bonding and conductive epoxy.

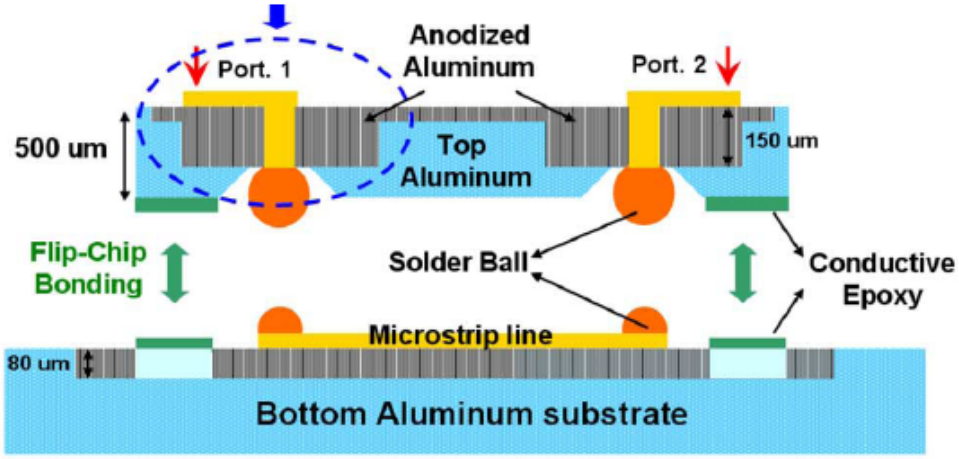

Figure 3.1 Illustration of quasi-coaxial structure designed for multilayer packaging applications [40].

The measured results in this work ranged from 0.1-to-25 GHz and the reflection coefficient along with the transducer gain of the device was determined. A result comparison was done between the design dimensions mentioned earlier and an inner and outer diameter of 300µm and 1.2mm. The results demonstrated that the coaxial structure with the smallest inner diameter had a better transducer gain (-0.75dB) but exhibited poor reflection coefficient (-12.4dB). Although the results proved to be sufficient for packaging use, the device did not reach a high frequency level for signal transmission and was not compatible for use in material characterization. Also, the use of solder balls, flip-chip bonding, and epoxy created the need for thermal compression on the substrate which may have damaged the surface and reduce the device performance. Therefore, a vertical coaxial device that could avoid these design issues would be critical for this area of work.

Previous work has also demonstrated the design of a vertical coaxial probe integrated in a bulk silicon wafer [41]. In this work, a 3D coaxial probe was designed on a 150µm thick silicon substrate and evaluated up to 80 GHz. To reduce the diameter ratio of the probe,

benzocyclobutene (BCB), a polymer, was included in the silicon substrate and used as the dielectric material which included an outer diameter of 240µm. The inner diameter was made of gold to reduce metal losses and was 75µm. The coax structure had a characteristic impedance of 44 Ohms which corresponded to a diameter ratio of 3.2. A 12µm layer of BCB was also added on the top side of the substrate as well as a layer of gold. The gold layer was placed over the entire top side of the substrate and not within the coaxial center. This layer was used to include the microstrip line on top of the probe which was designed to transmit an electromagnetic signal, and served as the ground conductor for the coaxial structure. The figure below shows the vertical coaxial probe design used in this work.

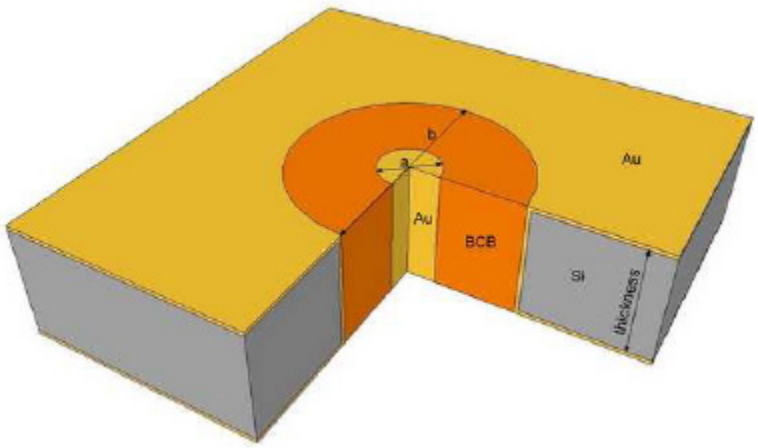

Figure 3.2 Vertical coaxial probe with integrated BCB polymer material as dielectric [41].

The results demonstrated a transducer gain less than -0.2dB up to 80 GHz and a reflection coefficient less than -15dB over the entire frequency range from dc-to-80 GHz. These results were excellent proving the ability to transmit an RF signal successfully; however, the data was only simulated and not measured. The device was in the process of being fabricated, but without the measured data, the performance of this device is only an estimation of its full capability. Furthermore, the design was not fully a coax because the researchers used a thin layer of gold on top of the surface as an outer conductor.

Additionally, previous researchers have also used a novel flip chip approach to develop a vertical coaxial probe [42]. Figure 3.3 shows the flip-chip probe design which was used to integrate with packaging systems as interconnects. This work included the use of C-shaped ground bump pads to complete the desired coaxial structure. The design consisted of a substrate and a chip with separate gold C-shaped ground bump pads and wall thicknesses of 50μm at a height of 30μm, which were used for ground connections. The substrate was made of a 254μm thick Alumina layer and the chip material was gallium arsenide with a thickness of 100μm. The two C-shaped ground bump pads included 50μm gold inner conductors which provided the signal, and an outer conductor of 120μm. The C-shaped ground bumps were then placed in opposite directions of one another to ensure full ground and signal connection, which formed the vertical coaxial structure. Both the chip and the substrate included coplanar waveguide (CPW) lines that were used during measuring to determine its performance at high frequencies. The width of the CPW lines were 50μm and the gap distance was 24μm for the substrate and 34μm for the chip. Port 1 of the model was probed at the CPW feed of the substrate and port 2 was at placed at the feed line of the chip, which provided S-parameter measurements for the structure. The inner to outer conductor ratio of 5 served as the best performance of the system demonstrating a reflection coefficient better than -25dB and a transducer gain less than -0.4dB up to 40 GHz.

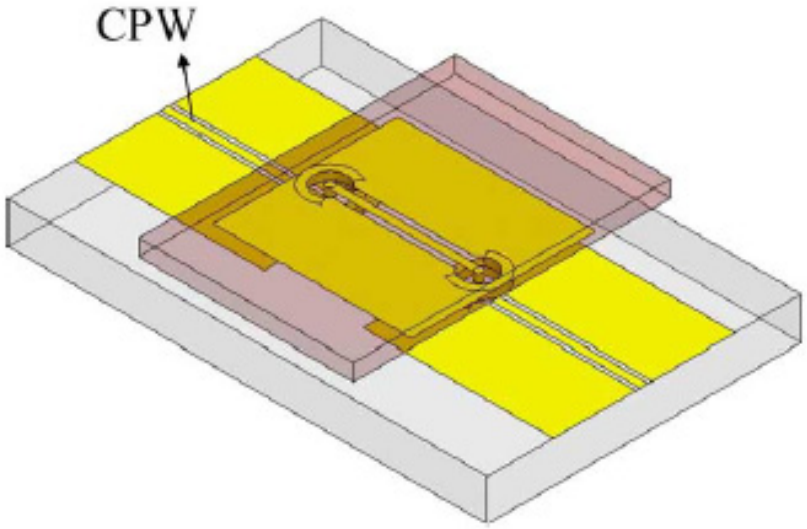

Figure 3.3 Novel vertical coaxial probe design used for flip-chip interconnect applications [42].

Although results demonstrated the probe having good signal transmission abilities, however, the thermo-compression method used during bonding caused deformation in the bump designs. This included a reduction in the bump height and a shift in the inner and outer conductor radii. These discrepancies played a major role on the operating frequency range of the probe which only reached up to 40 GHz.

Furthermore, a vertical coaxial probe design with an integrated wire bond approach was developed in [43] for system-in-package applications up to 20 GHz. In this work, the system was designed to interface with standard wire bond pad configurations and included a coaxial inner diameter of 79μm and outer diameter of 254μm. The inner conductor consisted of silver-plated copper clad steel with an insulating layer of polytetrafluoroethylene, while the outer conductor was created with a solid tubular layer of copper. Researchers designed two topologies for the coaxial cables; placing them adjacent from one another and stacked on top of one another. The top and bottom silicon substrates included sets of metal coplanar trace lines (ground-signal-ground). The center lines served as the signal trace and the two outer lines served as the ground traces. The silicon substrates included etched trenches in front of the traces which held the coaxial cables in contact with the coplanar lines. The outer metal of the cables were then etched back to

allow the center metal to stick out for center line connection. The outer metal then connected with the outer ground trace lines within the trench. The wire bonds were then used to connect the 3 trace lines together on both of the stacked and side by side silicon substrates. However, the stacked topology required the coaxial cables to be curved under in order to make a good electrical connection. Figure 3.4 below shows the vertical coaxial probe designs used in this work with integrated wire bonding.

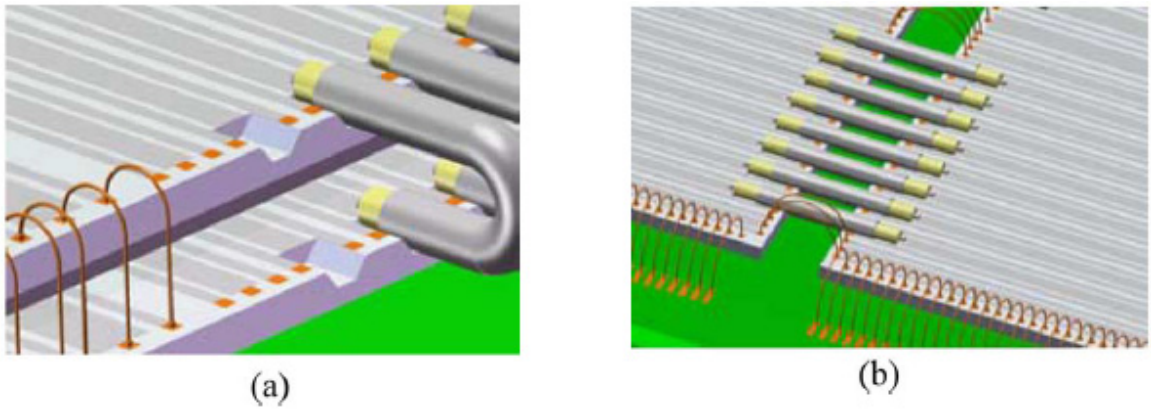

Figure 3.4 Three-dimensional vertical coaxial probe designs used for system-in-package applications. (a) Stacked dies and (b) Adjacently placed dies [43].

The design was able to achieve a transducer gain of less than -0.7dB from 0-to-20 GHz and a reflection coefficient less than -23dB; which demonstrated good behavior compared to traditional wire bond techniques. However, in order to connect the inner conductor to the signal trace line, and to connect the outer conductor to the ground trace lines, an epoxy was used. This could have reduced the performance of the system because the strength of the connection was not very reliable due to the connection method; which prevented the device from behaving even better. Furthermore, losses present in the cable from bending the line for substrate connection, as well as losses in the wire bonding technique reduced the operating frequency of the device, causing it to perform well only up to 20 GHz.

As an improvement to previously designed coaxial probes, in this work, a low-cost through-wafer vertical micro-coaxial probe has been developed. This design includes a coaxial probe designed in a 300μm thick high resistivity silicon substrate. The use of this substrate allowed the probe to be design and fabricated at a lower cost than previous work, while increasing its ability to easily integrate with commercial devices by utilizing a well known dielectric. To reduce the propagation of first order modes, the probe was designed with an inner and outer diameter of 100μm and 300μm, corresponding to a 1:3 inner/outer diameter ratio. Although the dimensions of the probe are of similar size when compared to the previous designs, however, by reducing the component size on the silicon surface, the coaxial probe achieved a higher density of I/O connections than most. By introducing more coaxial probes on the surface, the signal transmission quantity of the probe increased. Most importantly, this reduction in component size allowed the probe to operate a higher frequency range with successful transmission abilities up to 65 GHz, while surpassing that of previous designs. Furthermore, unlike previous work where thermo-compression and/or solder bonding were required, this work eliminates the need for that process by implementing coplanar waveguide (CPW) feeds on both sides of the substrate; allowing the coaxial probe to be removable and re-used for simultaneous connections on multiple devices. The elimination of these processes has prevented the coaxial probe from experiencing any deformation in the design topology, as well as providing it with a strong resistance to structural failure. Lastly, while all of the coaxial probes mentioned above where designed to be used as interconnects/transitions in multi-level packaging systems, the micro-coaxial probe in this work was designed to characterize materials unknown materials at high frequencies as well as integrate with packaging technologies. The table below provides a comparison between previous coaxial probe designs and the micro-coaxial probe in this work.

Table 3.1 Comparison of Previous Coaxial Probe Designs

References	Probe Dimensions (Diameter)	Frequency Range	Application
[40]	Inner: 300µm Outer: 1mm Length: 500µm	dc-to-25GHz	3D Packaging Technologies
[41]	Inner: 75µm Outer: 240µm Length: 150µm	dc-to-80GHz (simulated)	MM-Wave 3D Integration Technologies
[42]	Inner: 50µm Outer: 120µm Length: 254µm	dc-to-40GHz	Flip Chip Interconnects
[43]	Inner: 79µm Outer: 254µm Length: 549µm	dc-to-20GHz	System-in-Package (SiP) Applications
Our Design [44]	Inner: 100µm Outer: 300µm Length: 300µm	dc-to-65GHz	High Frequency Material Characterization Packaging Systems (Dual Application)

From the chart, it can be seen that the dimensions of the probe design presented in this work are comparable to those of previous designs. However, our probe design does surpass the frequency range of operation for majority of the designs with the exception of [41]; which was designed to operate up to 80GHz but only provided simulated data for verification. Therefore, it's still difficult to determine its limitations of operation. Most importantly, the design in this work is not only to be used in high frequency packaging systems, but mainly to characterize materials at high frequencies. This micro-coaxial probe design was a contribution to the current state of the art because it included a dual application which enhanced the capabilities of previous designs. The table below shows the advantages and disadvantages of the previous coaxial probe designs compared to those of this work.

Table 3.2 Advantage and Disadvantage Comparison of Probe Designs

References	Advantages	Disadvantages
[40]	Novel embedded anodized aluminum design. Easier and cost effective fabrication method. Good signal transmission abilities.	Performance decreased beyond 10Ghz. Large design reduced operating frequency range and density of I/O connections.
[41]	Short length and high frequency range of operation. Cost effective materials. Good signal transmission up to 80GHz.	Not verified w/measured data. Difficult fabrication method due to multiple materials being integrated.
[42]	Novel vertical coax flip-chip design. Small coax structure increased I/O connections. Fairly high operating frequency.	Thermo-compression during bonding caused deformation in device geometry and reduced performance.
[43]	Novel stacked and adjacent die-to-die design. Increased signal speeds for SiP applications. Can easily integrate in packages.	Long design reduced operating frequency range. Required use of epoxy to make connection. Topology reduced I/O connection on surface.
Our Design [44]	Novel design flushed in silicon. Dual functionalities. Easier fabrication method and cost effective. High frequency range of operation. Miniaturized coax provided higher density of I/O connections. Can integrate with all commercial packaging applications.	Signal transmission ability needs improvement. Probe length reduced operating frequency range.

3.2 Impact of Metal Mining for Micro-Coaxial Probe

As mentioned earlier, the micro-coaxial probe in this work is made of two well known metals: silver and gold. Although these metals were specifically chosen because of their reputation as good conductors, a more detailed investigation must be included on the impact these metals have on the environment and on people (social). The direct impact of these metals on the community comes from the small-scale mining (SSM) industry. It has been discovered that several health and safety problems arise in the environment, which impact human life due to low-tech operations that are employed by unskilled and poverty-stricken workers [45]. These problems include areas such as: excessive pollution, chemical contamination, inadequate mine safety, and disease [46-48]. For example, several gold mining sites globally have significantly

impacted environmental pollution in communities due to acid mine drainage from waste rock dumps and piles, being 3 times the amount in Australia and 1.5 times in Canada [49]. In addition, the release of green house gas emissions has also become a major environmental issue for gold mining due to the extensive use of fossil fuels such as diesel; which typically release about 21.7 $kgCO_{2\text{-}e}$/t ore or about 11.5$tCO_{2\text{-}e}$/kg Au [49]. As a means for improvement, in recent years, mining industries have used environmental indicators such as the Life Cycle Assessment (LCA) to assess their performance, which allows them to evaluate their environmental performance associated with their process and helps support decision making [50]. However, from a social perspective, mining these metals brings employment, land rent, royalties, and has provided educational facilities and development projects for the community; but also brings hazardous diseases that directly affect the people [51]. These effects from both an environmental and social perspective are discussed in detail in the following sections.

3.2.1 Environmental Impact

To many residents, mining is viewed as a very dangerous activity which is accompanied by even more risky environmental impacts. Although residents in urban areas are considered the largest consumers of mining in the country, their view of mining in this aspect is the strongest [52]. People in rural communities however, view mining as an alternative source of employment and welcome it more than others. However, all residents believe that if mining is located in the community, it should be practiced in a healthy environment with everyone sharing equal benefits. To accomplish this goal, three fundamental considerations must be included: the environmental impacts should not pose unacceptable risk to associated communities; the mining company and the community must be transparent and effective with communications; and mine development must bring a complete benefit to the community [53]. In doing this, citizens must be willing to share their opinions in areas that directly affect their futures, which can help mining companies avoid sustainability risk of both their operations and the community. It's also important that when

mining companies include the community in planning, development, and operation and post-closure, they select a diverse group to ensure all aspects of the group is covered [53]. Nevertheless, mining companies eventually pose problems for communities when these factors are overlooked.

In most countries with flourishing small-scale gold mining industries, the most significant problem reported by the community was mercury (Hg) pollution due to complications in mineral contamination. For example, in 1999, the U.S. Department of Health and Human Services recognized mercury as a main global contaminant known to cause deleterious neurological, developmental and other health effects [54]. This Hg contamination occurs as a result of a process known as amalgamation; where mercury is applied to gold-aggregated sediment and then burned in open air, resulting in the release of inorganic mercury into the environment [55]. This then transforms the mercury into toxic methylmercury, which is deadly to plant and aquatic life, and harmful to human health. Furthermore, it is one of the few pollutants that cause human death due to food contamination, and based on studies in 1992, it was estimated that over 1,400 humans died from Hg poisoning while over 20,000 were afflicted in the last 40 years; equaling mortality rates ranging from 7% to 11% [56]. Therefore, the seriousness of Hg contamination has led to more advanced studies aiming to control this emission issue, which has resulted in a decrease in global Hg inputs to the environment. For instance, in the early 1970's estimates of anthropogenic Hg emissions ranged from 10,000 to 30,000 $t.yr^{-1}$; however, in the late 1980's emission estimates decreased to 6,000 to 13,500 $t.yr^{-1}$, indicating the impact of effective Hg control policies [56]. Another important problem reported is environmental degradation in small-scale mining because it requires a continuous amount of pitting and trenching. This causes an abundant of forest tracts to be removed while rivers are diverged in search for ore. When this occurs, most of the excavated land is not broken properly and it results in potholed landscapes, which poses a risk to people and homes in nearby communities due to possible landslides and the development of large

sink holes. Lastly, there is also a major problem with the declining health and safety of industry workers due to poor environmental conditions such as poor ventilation, lightning, hygiene and sanitation, and excess dust in shafts [45]. This is because workers are more willing to place themselves in a higher degree of personal risk in order to maximize profits; which bring a higher pay grade and a more hopeful sense of employment security. For example, underground mine workers face extreme risk because of poor ventilation and roof supports, which result in cave-ins and fires ignited by lanterns.

Therefore, major efforts must be made to improve the environmental management of mining practices across the country. Without improvement, the industry will continue to seem detrimental to further development needed to sustain a healthy environment. It will take assistance from both the community and government to control the situation before it becomes unsolvable.

3.2.2 Social Impact

The type of impact that mining these metals have on the people is both a positive and negative viewpoint when related to the community. While SSM does provide an abundance of jobs in developing communities and make significant contributions to educational projects, it does however create an extremely unsafe environment for people living in these rural areas. In most cases, these sites are responsible for wide spreads of waterborne diseases due to the excessive trenching and pit construction [57]. This occurs because minimal reclamation is done on site, allowing water to accumulate in potholes and ditches, which becomes contaminated and serves as breeding grounds for disease carrying mosquitoes. Furthermore, due to the lack of women rights, females are continuously overworked and underpaid in most poverty stricken countries [58]. Most importantly however, the exploitation of child labor is the biggest issue that

mining industries are faced with today. Where conditions are the most sever, children are more likely to become involved in SSM activities; while educational opportunities are limited.

Consequently, although mining industries has the ability to assist with the development of small areas, it also puts the people directly in the path of harmful diseases and unlawful working conditions. To reduce the environmental and social impacts of mining these metals in communities, an extreme amount of preparation has to be done at a very fast pace. For this work, developing a method to recycle the metals being used (silver and gold), would assist in reducing the amount of drilling and trenching taking place in mining communities.

3.2.3 Designing Coaxial Probe with Recyclable Metals

To eliminate the amount of adverse environmental and social issues that mining has over its life cycle, devices such as the one in this research must be designed for end-of-life; having the ability to be disassembled and recycled with a design that can be used over an extended period of time. This end-of-life design concept was adopted from Principle 11 of The 12 Principles of Green Engineering which states, “Products, processes, and systems should be designed for performance in a commercial “afterlife” [59].” In this strategy, next-generation designs are encouraged in its early stages, to be based on recovered components with known properties, reducing the need for acquiring and processing raw materials. By incorporating this commercial process into this initial design, the processes, products, and systems can be recycled and reused as functional components at their highest value level [59]. This concept would also immediately reduce the amount of trenching and digging needed for manufactures, by developing products using remanufacturing and refurbished metals. This can be accomplished by doing the following: (1) using recyclable metals in the current market; (2) avoiding polluting elements that interfere with the recycling process; (3) avoiding threaded metal inserts in plastic; and (4) avoiding plated metals [60]. By addressing these ways to possibly reuse metals in the coaxial probe device, it

would extend its projected lifetime, decrease the need for virgin metals, and consequently decrease the need for a new product [61].

CHAPTER 4

DESIGN AND RF CHARACTERIZATION OF MICRO-COAXIAL PROBE

Proper modeling has to be done to determine the RF characterization of a coaxial probe, the electromagnetic distribution within the inner and outer coax, and the impedance at the device input. The modeling and design of the micro-coaxial probe presented in this chapter were done using HFSS. The finite element method solver provided simulation results on the electromagnetic distribution and the RF behavior of the coaxial probe. Using coplanar waveguide feeding mechanisms, the reflection coefficient and transducer gain of the probes were evaluated over a wide frequency band. In this frequency range, the probes needed to demonstrate excellent signal transmission between two ports. The verification of the probes was extremely important for implementation in the high frequency material characterization presented in Chapter 4 and future packing systems applications. Thus, in this chapter the modeling, simulation, fabrication, and characterization of the probes are presented.

4.1 Modeling of Micro-Coaxial Probes for RF Characterization

As mentioned above, the key to successfully characterizing materials at high frequencies is the ability to utilize a miniature open ended coaxial probe to determine their RF performance. Doing this provides the electrical properties of materials at low and extremely high frequencies. To ensure the best coaxial performance, it is recommended that a high resistive material be used as the outer dielectric to reduce substrate losses and surface wave propagation [62]. For this reason, this coaxial probe was designed flush in a high-resistive (3,000 Ωcm) 300μm thick silicon substrate to surround the probe in a low-loss environment. This material was also chosen due to its low-cost and easy integration abilities with commercial applications. Figure 4.1 illustrates the 3D model of the vertical micro-coaxial probe flushed in the silicon substrate.

The inner conductor of the micro-coax, which provides the signal to the system, was made of silver. The outer conductor was also made of silver at 150µm width and was used as a metal ground to complete the probes metal/dielectric/metal topology. This particular metal was chosen because of its high level of conductivity which easily allows the flow of electrical current, generating an efficient RF signal flow. The ground width had to be optimized in order to achieve accurate signal transmission. By adjusting the radius of the outer conductor layer, the probes can operate at V-band frequencies.

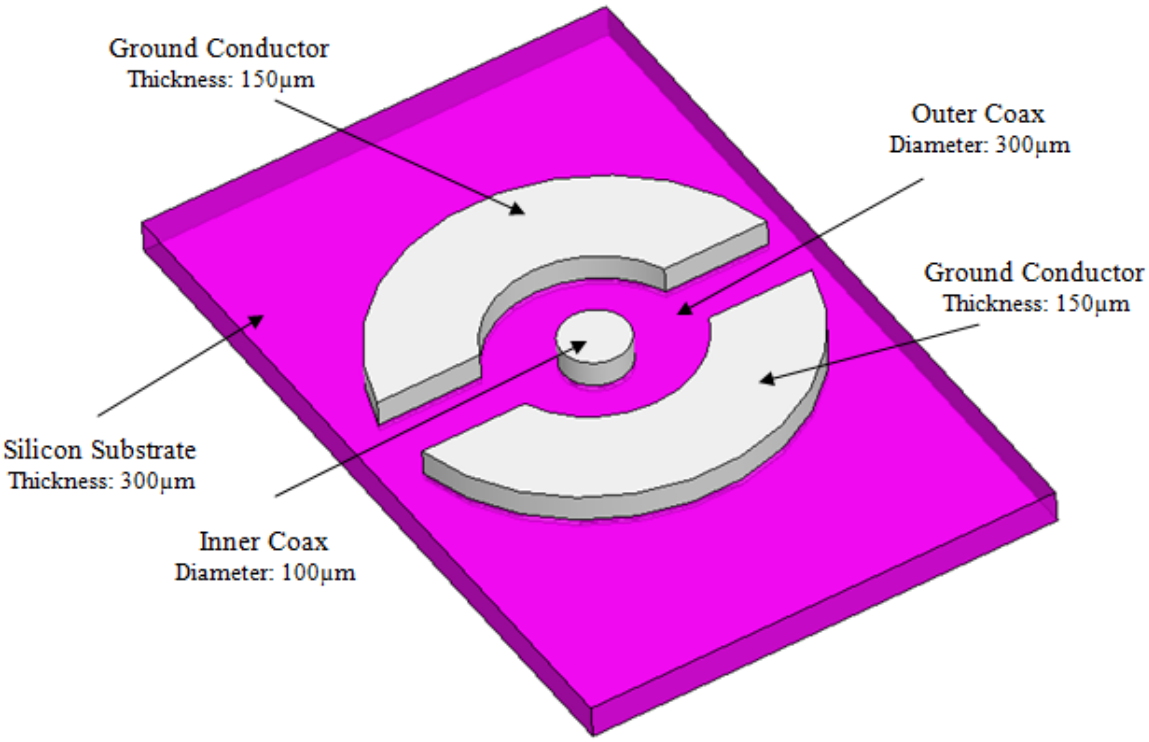

Figure 4.1 3D Vertical Micro-Coaxial Probe flush through silicon substrate.

4.2 Coaxial Probe Design Theory

When using silicon as a dielectric however, the inner/outer coaxial ratio must be carefully determined to avoid frequency limitations and to achieve desired performance. These frequency limitations are due to the propagation of TE_{nm} modes which are caused by the probes circular waveguide structure. The first higher order mode to propagate in the coax is the TE_{11}; where n=1 refers to the number of circumferential variations and m=1 refers to the number of radial

variations. Within the probe, this mode then becomes the dominant circular waveguide mode to appear [63]. To reduce the propagation of this mode, the ratio of the coaxial probe has to be significantly reduced. In this case, the coax was designed with an inner and outer diameter of 100μm and 300μm. This ratio was chosen because HFSS simulation results proved the micro-coax achieved proper signal transmission through the desired extremely high frequency band. The inner/outer conductor ratio was also determined in order to calculate the characteristic impedance of the coaxial probe. This impedance takes into account not only the fixed dielectric ratio but also the dielectric constant of the known material; which in this case was silicon. According to [41], the equation below can be used to determine the characteristic impedance of a coaxial line with a known dielectric constant. Corresponding to a 1:3 inner/outer diameter ratio within a silicon dielectric, characteristic impedance (Z_o) of 19.3Ω was calculated for the micro-coaxial probe:

$$Z_o = \frac{60}{\sqrt{\varepsilon_r}} \ln \frac{R_{out}}{R_{in}} \tag{4.1}$$

where ε_r is the dielectric constant of silicon, R_{out} is the radius of the outer dielectric, and R_{in} is the radius of the inner conductor. In this equation, a dielectric constant of 11.7 was used to represent high resistivity silicon. The value that is calculated from the characteristic impedance equation is important as it demonstrates a mismatch that can occur between the source used during measuring and the coaxial probe. Although the characteristic impedance of the coaxial probe is lower than that of the 50Ω source impedance, it is not guaranteed that it will create signal loss due to its electrical length. In order to reduce the possible impedance mismatch, it is suggested that the electrical length of the probe be kept as short as possible [64]. This length is mainly controlled by the depth and effective wavelength of the coaxial probes. Since this probe was designed flush in a silicon substrate, the thickness of the substrate helped determine the depth of the coaxial device.

For this reason, a substrate thickness of 50μm was originally chosen for this work, but had to be changed to 300μm because of its ease of fabrication and metallization. Using this

physical length (thickness) and the effective wavelength of silicon at 60 GHz, its electrical length was then determined. Using Equation 2 below, an electrical length of 72˚ was calculated for the micro-coaxial probe. This length however, is not as short as preferred, but due to issues and limitations that arose during the metallization of the probes, it was chosen as a more feasible thickness.

$$E_{eff} = \frac{d}{\lambda_{eff}} \times 360° \tag{4.2}$$

In the equation above, d represents the physical length of the coax and λ_{eff} is the effective wavelength of silicon at 60 GHz. A center frequency of 60 GHz was chosen for the micro-coaxial probe due to its ability to possibly integrate with a 60 GHz passive millimeter wave antenna in future work. The effective wavelength of the probe is extremely important because it takes into account not only the substrate of use at this frequency, but also the complex surface impedance of the metal [65]. This determination allows the probes to respond better at higher frequencies due to

$$\lambda_{eff} = \frac{c}{f\sqrt{\varepsilon_r}} \tag{4.3}$$

its shorter wavelengths. The equation below was used to calculate the effective wavelength of silicon to be 1.5mm at its center frequency. In this equation c represents the speed of light in free space, f is the center frequency, and ε_r is the dielectric constant of silicon.

While increasing the electrical length of the probe did improve its metallization abilities, however, it reduced the overall input impedance of the coaxial system. As stated before, the coaxial probes characteristic impedance was 19.3Ω which was mismatched to the source impedance but was minimized by implementing a short length. However, when the probes are connected to the 50Ω vector network analyzer (VNA) using a length of 300μm, the overall input impedance of the coaxial probes is expected to decrease due to impedance mismatching, which

reduces the performance of the entire system causing major signal losses to occur. The figure below illustrates an equivalent circuit model of the coaxial probe with its given length, connected to a 50Ω load.

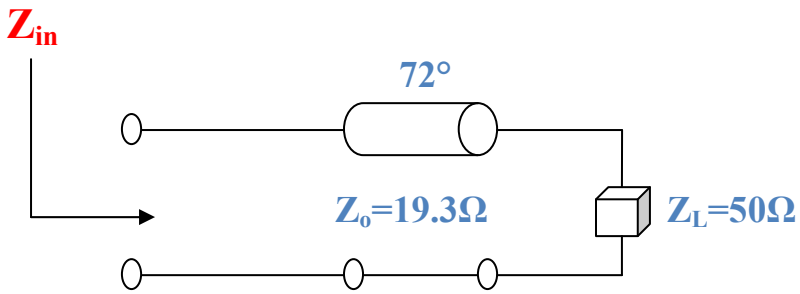

Figure 4.2 Equivalent Circuit Model of Coaxial Probe connected to 50Ω load.

Typically, the closer the device under test is matched to the source impedance, the more accurate the results. From the equivalent circuit model shown above, Equation 4 below was used to calculate the input impedance of the coaxial probe when connected to a 50Ω load.

$$Z_{in} = Z_0 \frac{Z_L + jZ_o \tan(72°)}{Z_o + jZ_L \tan(72°)} \tag{4.4}$$

Where Z_o is the characteristic impedance of the transition (19.3Ω) and Z_L is the 50Ω load, an input impedance of 10 Ω was calculated. This calculated value was not purely real and extremely low compared to the source impedance, and increased the probability of losses being present at the input. This created a major concern for the RF performance of the coaxial probe because major losses could reduce the operational bandwidth of the probe. However, it was decided to design the probe with a length of 300µm and determine its performance using HFSS results.

4.3 Coplanar Waveguide Addition to Micro-Coaxial Probes

In order to perform RF characterization on the micro-coaxial probe in this work, an efficient feeding mechanism was used to achieve minimal loss during measuring. For this reason, Coplanar Waveguide (CPW) lines were implemented in this design to make a proper connection

with the coaxial structure and to measure its RF performance. Figure 4.3 illustrates the CPW line integration with the vertical micro-coaxial probes that will be used for RF characterization. These lines are being widely used today due to their ability to provide electrical contacts for high frequency MMIC applications [66]. Their ground-signal-ground (G-S-G) topology made of a conductive metal allows electrical current to pass through its signal line and is then connected to the device to measure its RF performance.

The key to designing the proper CPW lines for a device is being able to control the capacitance that exist between the signal and ground lines. This gap distance is mostly based on the thickness of the substrate being used, the width of the signal line, and the frequency of operation. Controlling these factors is critical to achieve a characteristic impedance of 50Ω. Usually, as the thickness of the substrate decreases, so does the gap distance of the CPW lines; and the opposite applies for an increased substrate thickness. The width of the signal line is also important in achieving the desired 50Ω match because it is designed for a chosen center frequency; which is a constant that helps establishes the initial gap distance. Considering all of the above mentioned design characteristics enhances the probability of having minimal losses when transmitting a signal throughout a device.

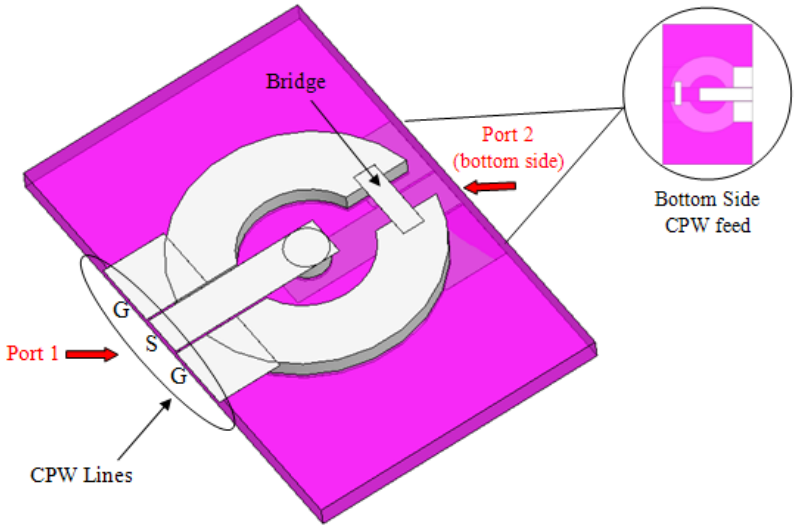

Figure 4.3 3D Vertical Micro-Coaxial Probe with CPW Line Integration for RF Characterization and inset of bottom side CPW feed with additional bridge connection.

In order to characterize the Micro-Coaxial probe between two ports, CPW lines were integrated at the top and bottom of both the center and outer conductors as shown in the above image. The width of the signal lines were 100μm and the ground lines were 160μm. The signal lines were connected to the center conductor and transmitted the RF signal, and the ground lines provided a reference for the outer conductor. However, to account for the open circuit that appeared in the outer conductors, silver bridges were implemented to complete top and bottom ground connections. The gap distance between the signal and grounds line was optimized to control the capacitance, and 5μm provided the best results over the desired frequency band. The CPW line configuration was carefully designed to match 50 Ω avoiding any impedance mismatching with the wave ports during simulation. By matching the CPW lines to 50Ω wave port, the lines matched the impedance of the 50Ω load shown in the equivalent circuit model. This allowed the coaxial probes to have minimal losses present at the integration of the coaxial system and the source during measuring.

4.4 Vertical Micro-Coaxial Probe Simulation

By implementing CPW lines at both ports, G-S-G probes can be used to measure micro-coaxial probes performance. The return loss, transducer gain, and electromagnetic distribution within the probe, will be used to for its RF characterization. The conditions used in the simulation setup (boundary conditions and wave ports) are shown in Figure 4.4 (a) below, followed by the reflection coefficient results of the probe results in Figure 4.4(b). In Figure 4.4 (a) it can be seen that a radiation box was used for the boundary conditions of the probe simulation. The probe simulation was excited using two wave ports placed at the edges of the radiation box for accurate results.

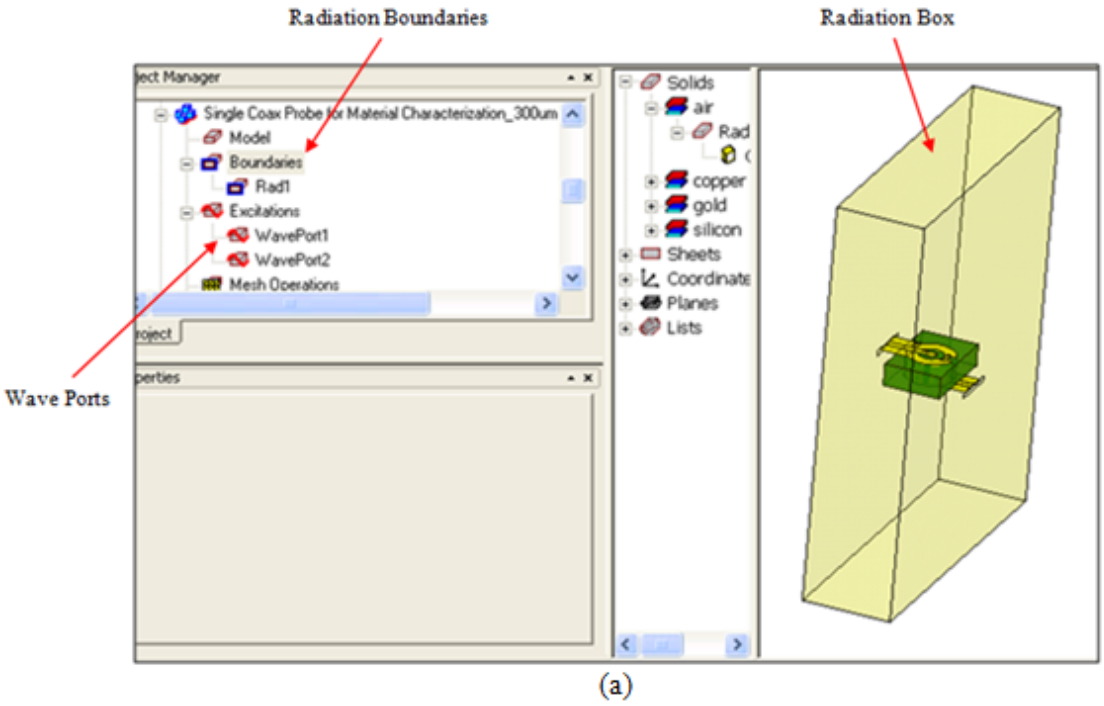

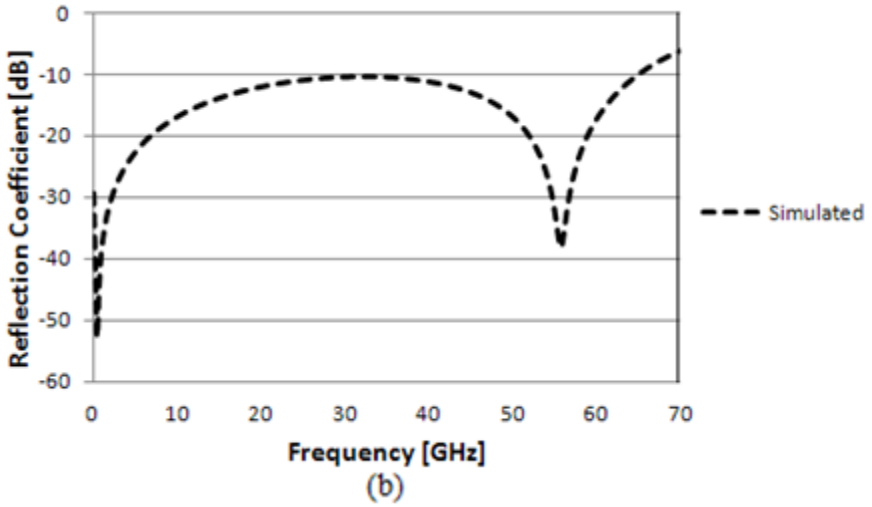

Figure 4.4 Micro-Coaxial Probe Simulation. (a) Conditions and (b) Reflection Coefficient results.

The simulated results indicate that the probe has a reflection coefficient lower than -10dB from dc-to-65 GHz. Results also show a resonance near 60 GHz which is due to the probe length being close to a λ/4 or 90˚. This was achieved because when the probe was designed, a center frequency of 60 GHz was chosen with a length of ~70˚ as mentioned above; which allowed the

reflection behavior to resemble that of a λ/4 design. With this performance, this proves that the probe is well matched to 50Ω over a wide band and will have minimum reflected power at port 1. This is true because S_{11} measures the RF signal seen at port 1, received from port 1. Therefore, the reflection coefficient data is much lower than 0dB over the frequency band, indicating that the signal is being fully transmitted from port 1 and not reflecting back. The above results prove that this probe can provide accurate measurement results when used for high frequency material characterization up to roughly 70 GHz. The data also shows that it can be successfully integrated as multi-layer transitions for mm-wave packaging systems up to 65 GHz. This probe also has a resonant frequency at ~58 GHz, which is important for future use as a measuring device for the passive 60 GHz antenna as mentioned in earlier chapters. The figure below illustrates the transducer gain obtained during simulation.

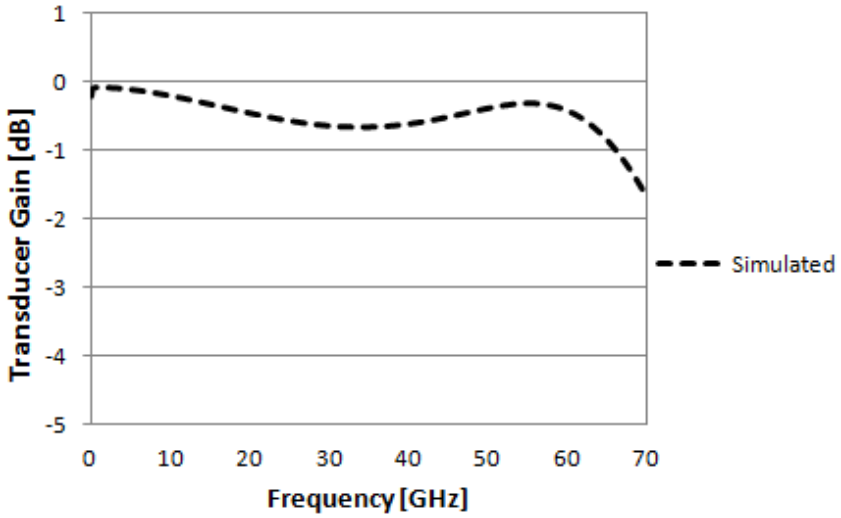

Figure 4.5 Simulated Transducer Gain for the Vertical Micro-Coaxial Probe.

The results above indicate that the probe achieved a transducer gain of less than -0.8dB from dc-to-65 GHz and -0.4dB at 60 GHz. This proves that the probe has excellent signal transmission over a wide frequency range by having minimal reflections present at port 1 and receiving maximum signal at port 2. This is the case because S_{21} measures the RF signal seen at

port 2, received from port 1. Therefore, the transducer data is as close to 0dB as possible, indicating that most of the signal transmitted from port 1 is being received at port 2 without any losses. The closer the transducer gain is to zero, the better the coaxial probe will perform. It is also important to observe the electromagnetic behavior within the coax as the signal is being transmitted. This observation was also done using the HFSS software. The EM distribution within the probe is shown below in Figures 4.6 (a) and (b).

(a)

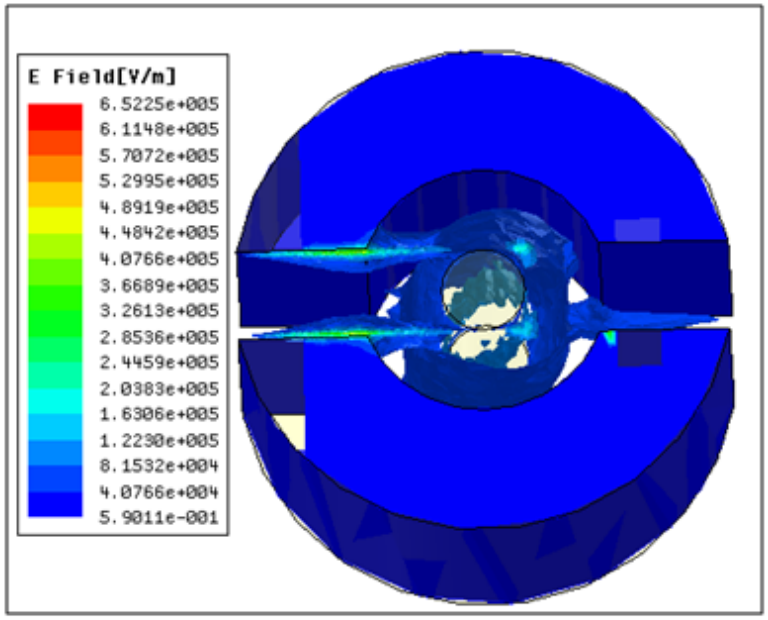

(b)

Figure 4.6 Simulated electromagnetic distribution. (a) Along the coaxial probes signal lines and (b) Inside the Micro-Coaxial Probe.

The illustrations above demonstrate the E-fields traveling within the electric field of the coax and CPW lines. The ports provide the excitation of current, allowing it to travel through the coax from one signal line to the next. The lighter colored regions indicate maximum E-fields through the transmission lines. These lines are behaving as inductors and the gaps in between the CPW lines produce capacitance. The focus of the electromagnetic field however, is within the coaxial region as shown in Figure 4.6 (b). To verify the necessity of the bridge gap in the coaxial conductor, a surface stress analysis was performed on the micro-coaxial structure without the opening in the conductor using COMSOL. The simulated results from the stress analysis are shown in Figure 4.7 below.

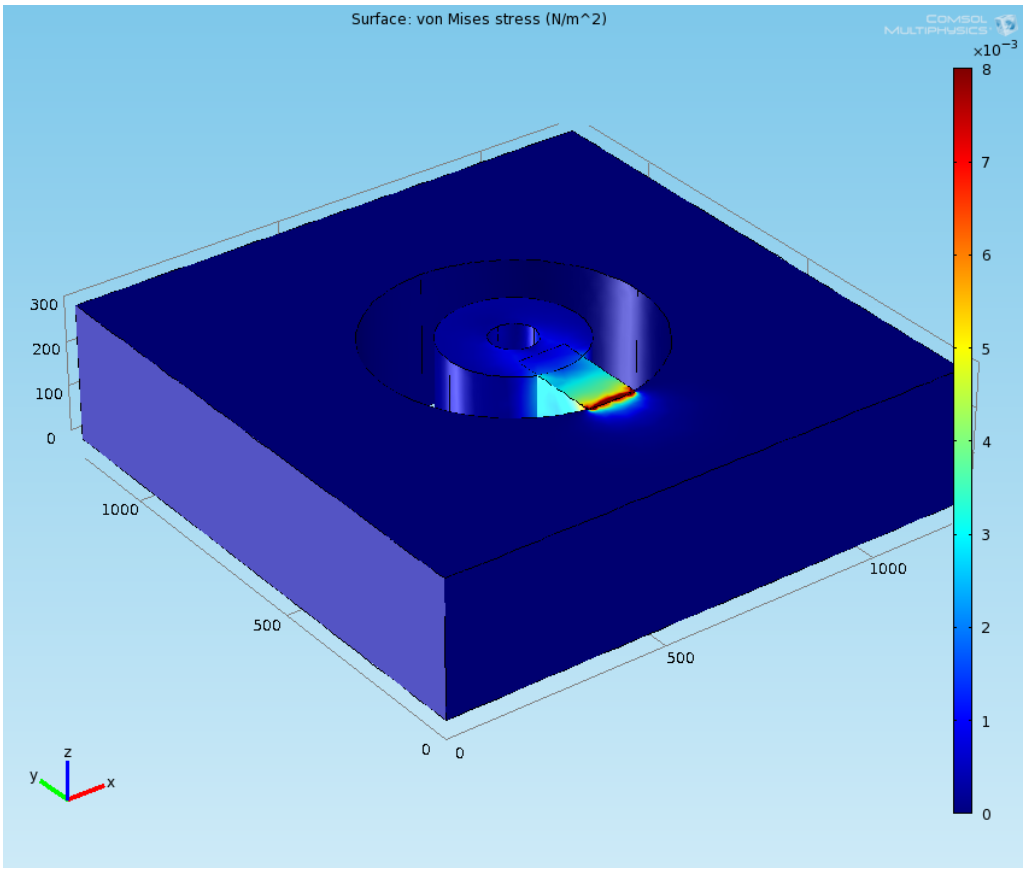

Figure 4.7 Surface stress simulation on coaxial probe structure.

The figure above shows that when a force was applied on the structure, majority of the stress occurred on the substrate areas surrounding the coaxial probe. This proved that when the force was applied to the device, the coaxial area collapsed within the silicon surface due to a lack of support between the through holes and the substrate. Without the conductor gap, the through holes fell through the surface and presented the need of a base to rest on. This analysis proved that by creating a gap between the conductor, the probe would be able to properly rest in the substrate. The figure below is an ADS equivalent circuit model of the micro-coaxial probe.

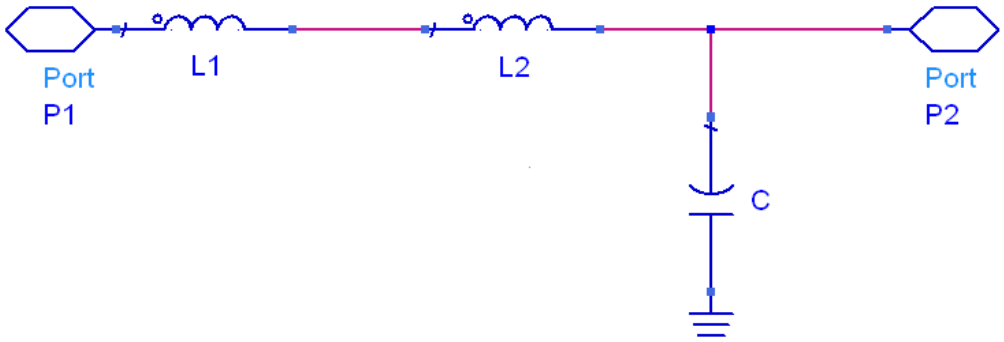

Figure 4.8 Basic equivalent circuit model of the vertical Micro-Coaxial Probe.

In this model, the first inductor (L_1) represents the CPW signal lines included on the top and bottom surface of the transition. Inductor L_2 is the inductance within the inner conductor of the coax. This inductance also has resistance due to the resistivity of the conductor being used. Lastly, the capacitance in the circuit models the capacitance existing between the inner conductor and the outer dielectric.

4.4.1 Effect of Varying Probe Outer Coaxial Diameter

Although the dimensions of the design presented in the earlier section was chosen, several variations in the outer coaxial region were considered to in order to achieve maximum performance. This specific region of the design is critical because by adjusting the outer diameter

of the coax, its characteristic impedance will change, causing a change in the impedance matching with the rest of the system during measuring. When this happens, the additional CPW lines connected to the probe will have a different impedance value at the interface. This variation in dimension is also important because it affects the presence of the dielectric in the design which can drastically change the behavior of the device due to the adjustment of the outer/inner diameter ratio. These variations include a frequency shift in the overall bandwidth and a change in the reflection coefficient and transducer gain. Since this variation in diameter has a large impact on the performance of the system, several different dimensions must be simulated to determine which adjustments provide the optimum results.

As mentioned in previous sections, the outer diameter of the coax was chosen to be 300µm. However, to perform this study, the inner diameter of the coax remained constant at 100µm while the outer diameters of the coax were changed to 200µm, 250µm, 350µm, and 400µm, where their reflection coefficients and transducer gain were determined. The diameter variation was chosen to be every 50µm because at the micron level, the coaxial probe will demonstrate a change in its RF characteristics when a minimal adjustment is made to the outer diameter. The figure below illustrates the behavior of the coaxial probe when adjustments to the outer coaxial area were made.

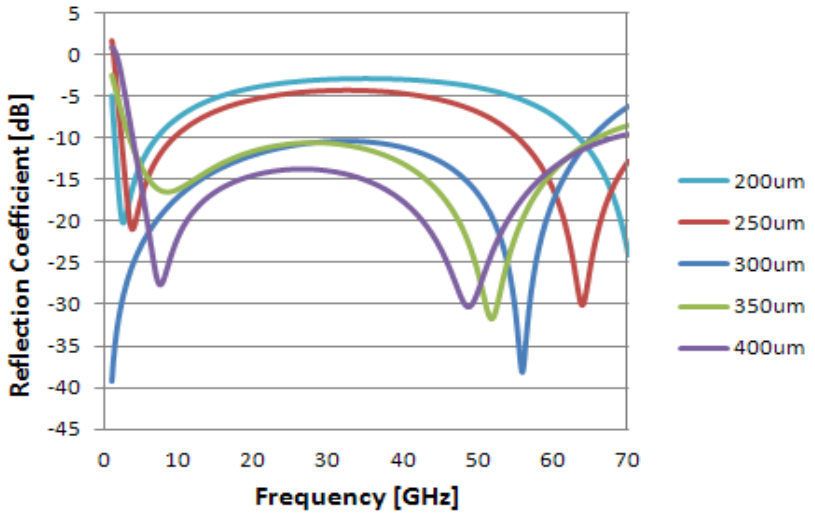

Figure 4.9 Simulated Reflection Coefficients of coaxial probe when adjusting coax outer diameter.

From the figure above it can be seen that when adjusting the dimension of the outer diameter, it directly impacts the reflection coefficient of the device. It is important to note that the reflection values at dc are greater than 0dB making them non-physical. At dc, the reflection coefficient should be low and could have been affected due to a simulation issue. The results indicate that the outer diameter of the coax can be used to optimize the reflection coefficient response. This proves that as the dimensions of the outer diameter are decreased from its original 300µm size, the reflection coefficient value is reduced. This indicates that while increasing the outer coaxial diameter, impedance mismatching will began to occur within the probe because some of the RF signal seen at port 1 is being reflected back, which reduces the overall power transmission of the device. This caused the reflected signal to reach above -10dB over majority of the frequency spectrum, which reduced the bandwidth of the device. A reflection coefficient of -10dB represents 90% signal transmission and is the marker used in simulation to represent the most accurate conditions prior to measuring.

However, when the diameter of the coax was increased from its original 300µm size, the reflection coefficient response did improve. When the diameter was increased to 350µm and

400µm, the probe demonstrated good signal transmission to the opposite port, having minimal reflections seen at port 1. This performance also allowed the reflection data to remain under -10dB over nearly the entire frequency band which increased the overall bandwidth of the device. The table below shows the change in overall bandwidth of the probes when the outer diameter of the coax was increased/decreased from its original 300µm topology.

Table 4.1 Overall Bandwidth Performances with Change in Probe Outer Diameter

Outer Diameter of Coaxial Probe (µm)	Bandwidth of Frequency Response
200	dc-to-8 GHz and 65-to-70 GHz
250	dc-to-10 GHz and 55-to-70 GHz
300	dc-to-66 GHz (null at 30 GHz)
350	dc-to-67 GHz
400	dc-to-70 GHz

The table above proves that when increasing the outer diameter above 300µm, the overall bandwidth of the device was nearly extended across the entire frequency band. However, it can be seen that when the dimensions are decreased, the reflection coefficient rises above the -10dB level over a large portion of the frequency band, allowing them to only be functional at a few frequencies. This is critical because this adjustment would reduce the commercial integration abilities of the probe by operating at specific levels versus being useful over an entire band of frequencies.

The transducer gain of the probe was also investigated when the same adjustments were made to the outer diameter of the coax. This simulated data was equally critical to the device performance as was the reflection coefficient data. This is true because if the probe is demonstrating excellent signal transmission from port 1, it is important that the entire signal is received at port 2. If this signal is not being properly received at port 2, it will immediately be

reflected back to port 1, reducing the overall performance of the probe. The simulated transducer gain data when the outer diameter of the coax was adjusted is shown in Figure 4.10 below.

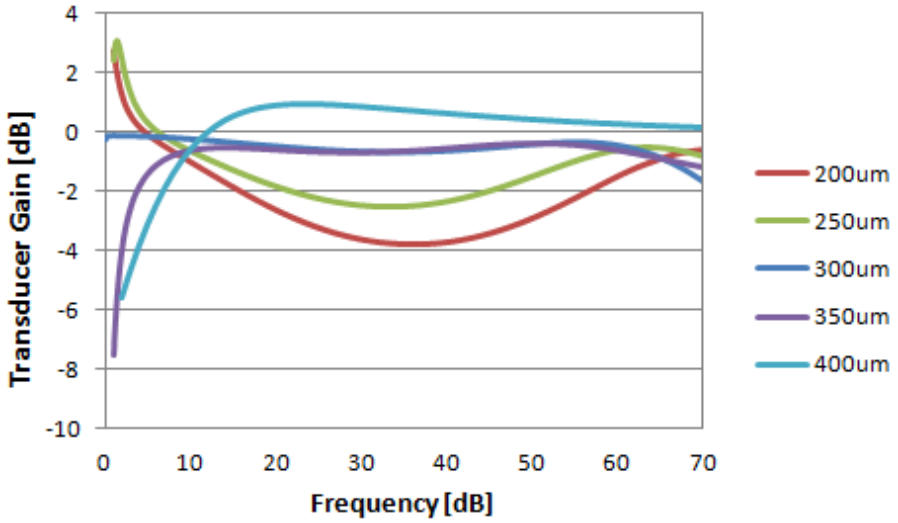

Figure 4.10 Simulated Transducer Gain of coaxial probe when adjusting coax outer diameter.

The results from the above transducer gain study, ignoring the non-physical simulation artifacts observed near DC frequencies due to convergence issues, also proved that when the outer diameter of the coax was decreased, it reduced the performance of the transmitted signal. As mentioned earlier, when analyzing the transducer gain performance of the probe, the closer the data is to 0dB the better because this means that the entire signal is being received at port 2 from port 1, having minimum reflections present. When the outer dimensions were reduced from its original 300µm value, the transducer gain decreased significantly, reaching values between -2 dB and -4 dB through nearly the entire frequency spectrum. These results did improve near the 60 GHz and 70 GHz range, but a notable amount of signal loss can be expected at lower frequency levels. However, when the coax diameter was increased, results indicate that excellent signal transmission can be expected due to the transducer gain data ranging between 0dB and -1.5dB at best. Although substantial signal loss can be seen at very low frequencies such as dc-to-2 GHz, full propagation is still achieved up to 70 GHz.

Following this parametric study of adjusting the outer diameter of the coaxial probe, one can assume that the best device performance can be achieved by increasing the outer diameter to ~ 400μm. However, although results support this argument, by providing the maximum amount of signal transmission over the widest frequency band, this reduction in outer conductor diameter would cause a significant increase in fabrication issues. Most importantly, increasing the diameter of the outer coax, would inversely decrease the diameter of the outer conductor; creating a more narrow circumference to be filled during the metallization process. Trying to metalize such a narrow area could create a less dense fill and increase the risk of the coaxial holes not being filled through the entire wafer. Therefore, it should be again noted that the processing and device fabrication presented in the sections to follow were done for the coaxial probe with an outer diameter of 300μm.

4.5 Processing Techniques for Device Fabrication

The fabrication process of the micro-coaxial probes mainly involved photolithography as well as electron beam deposition. The brief description below gives an overview of the techniques used to develop the micro-coaxial probes.

4.5.1 Photolithography

Photolithography (also termed "optical lithography") is a process that utilizes ultraviolet (UV) light to transfer geometric patterns from a photomask to the surface of a substrate [67]. This process, however, involves several steps that the substrate must undergo before any metallization or depositions can occur. These steps include wafer cleaning, photoresist application, soft baking, mask alignment, exposure and developing, and hard baking [68]. The lithography tool used in this work was the Karl Suss Mask Aligner and is shown in Figure 4.11 below.

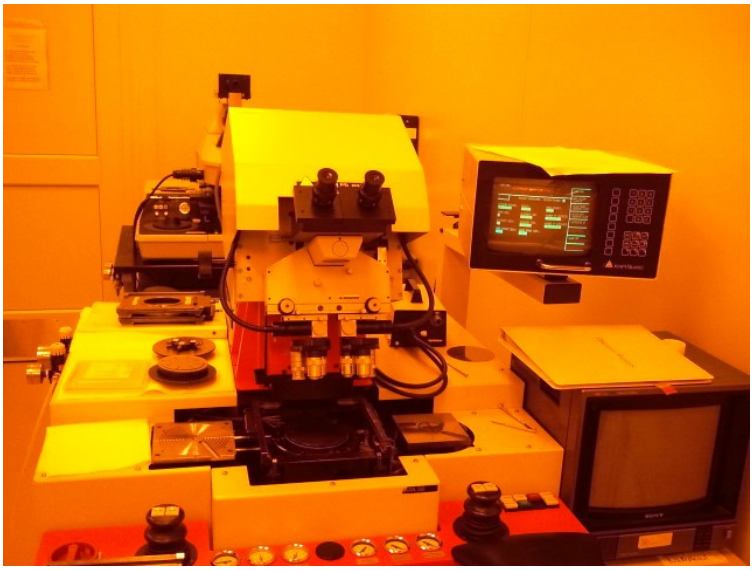

Figure 4.11 Image of Karl Suss Mask Aligner tool used during photolithography.

A brief overview of each step in the photolithography process is presented below:

(a) *Wafer Cleaning and Applying Photoresist:* This is the initial step in the photolithography process. The substrates in use are thoroughly cleaned to remove any particulate matter from the surface. Then photoresist is applied to the surface of the substrate using a technique known as "Spin Coating," which forms a thin layer on the wafer.

(b) *Soft Baking:* Soft Baking is performed once the photoresist has been applied to the surface. This step removes most of the solvents that appear in the photoresist coating. The photoresist then becomes photosensitive, allowing the UV light to penetrate through.

(c) *Mask Alignment and Exposure:* This is one of the most important photolithography processing steps. The spin coated wafer is loaded into the mask aligner and the "photomask" is placed on a holder chrome side facing up. The mask is aligned with the wafer and then the pattern is transferred onto the wafer surface using high-intensity ultraviolet light. Every mask that follows the first one must be aligned to that of the previous pattern.

(d) *Development:* During this process, the wafer is submerged in a developer solution which removes photoresist from areas that were exposed to the ultraviolet light. The areas that

were protected by the mask remain on the substrate after development. If negative resist is used however, the removal of the photoresist is inverted, leaving the areas that were exposed to ultraviolet on the wafer and removing those that were not.

(e) *Hard-Baking:* This is the final step of the photolithography process. This step is used to harden the photoresist on the wafer surface and to improve adhesion.

4.5.2 Electron Beam Deposition

Metal evaporation on a substrate can be done using various methods such as thermal and E-beam techniques. During an E-beam deposition, a target metal is bombarded with an electron beam that is given off by a charged tungsten filament under high vacuum. This electron beam causes atoms from the metal to transform into a gaseous phase; wherein these atoms precipitate into a solid form, coating everything in the chamber with a thin layer of metal [69]. Figure 4.12 below shows an example of the deposition technique. In this work, we have used E-beam deposition to form the CPW lines on the micro-coaxial probe. Figure 4.13 illustrates the actual instrument used to deposit the desired metal.

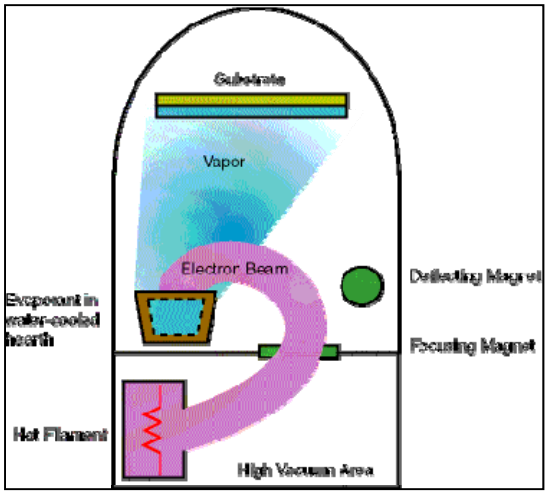

Figure 4.12 Illustration of E-beam Deposition technique [70].

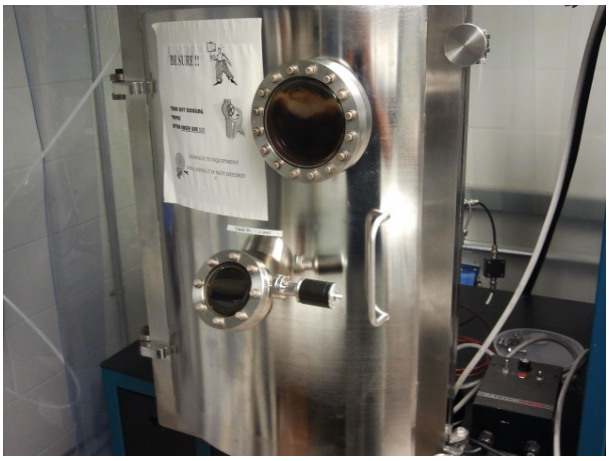

Figure 4.13 Actual E-beam instrument used in this work.

In this deposition technique, the target metal metals were chrome and gold. These metals were bombarded by the e-beam and deposited on the silicon surface by applying current to the electrodes within the chamber. The current is slowly increased to avoid any damaging of the target crucible. A crystal sensor is also located in the vacuum chamber which serves as a thickness monitor, and verifies the amount of metal deposited on a thin layer.

4.6 Fabrication of Vertical Micro-Coaxial Probes

The vertical micro-coaxial probes were fabricated using the photolithography techniques describe in the before mentioned section. Figure 4.14 illustrates the steps involved in fabricating the micro-coaxial probes.

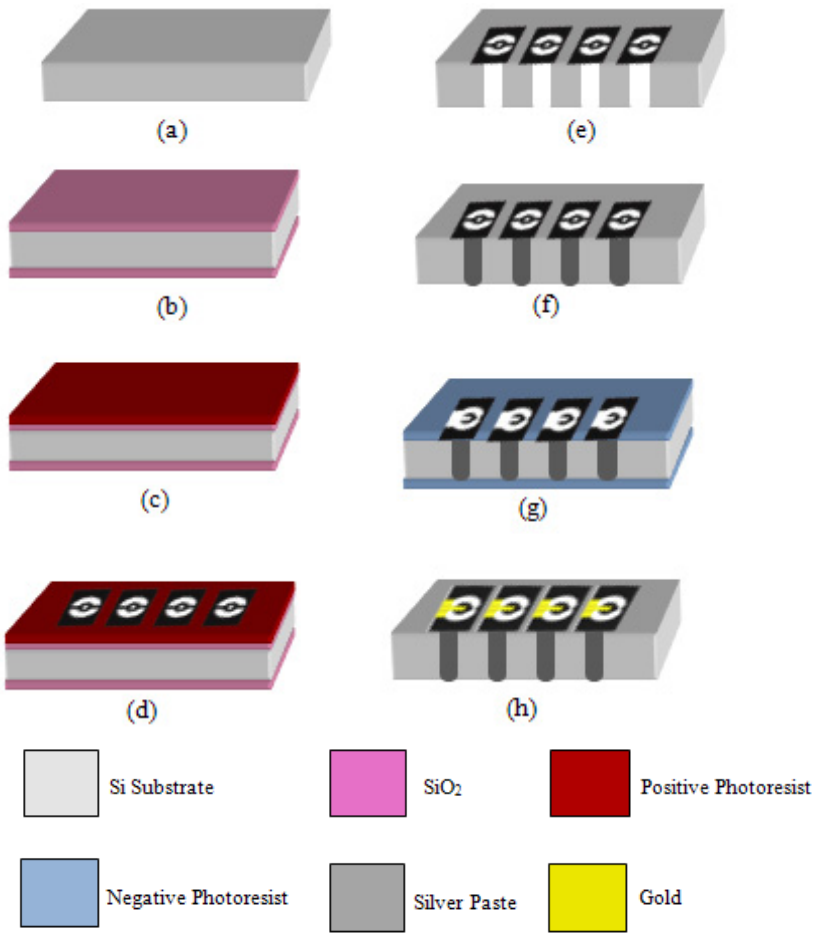

Figure 4.14 Fabrication process sequence for the vertical micro-coaxial transition. (a) Si substrate, (b) SiO_2 grown on the substrate, (c) Photoresist deposited for patterning, (d) Pattern transfer by photolithography, (e) Removal of SiO_2 layer for etching and coaxial vias formed using deep reactive ion etching, (f) Metallization of holes, (g) Pattern transfer for CPW lines, and (i) CPW line metal deposition.

4.6.1 Formation of Coaxial Through Holes

The above probes were realized on a 2" and 300μm thick silicon substrate. Initially, the silicon substrate was thermally oxidized on both sides to grow a 1μm thick SiO_2 layer. This oxidation process was required on the substrate because it served as an etch protective layer to the photoresist during the formation of the through holes. Following the oxide growth process, a photolithography step was performed to pattern the coaxial configuration on the substrate. Using the Laurel Spinner, the substrate was spin coated with photoresist AZ 4620 (10 μm) on the front

side at 500rpm for 10 seconds with an acceleration of 50; followed by an additional spin step at 1000rpm for 60 seconds with an acceleration of 50. This is a very thick resist that has excellent adhesion and provides excellent coating properties. Following resist coating, the wafer was soft baked for 20 minutes at 100°C. After baking, a 24-hour rehydration process was included in preparation for silicon etching that followed. This was necessary because thick resist films (10 μm range) require several hours for rehydration, whereas thinner films (3 μm) completely rehydrate after seconds. Furthermore, with insufficient rehydration, the resist keeps water depleted and reveals a significantly lower development rate as compared to the rehydrated top layer [68]. Therefore, rehydrating the wafer ensured a smooth development stage. Using a photomask, the wafer was then exposed with the mask pattern for 13 seconds at 25mw/cm^2 on the Karl Suss mask aligner. The wafer was then placed in a developer solution (AZ 400K 1:4) for 4-5 minutes. After developing the pattern, the substrate was hard baked for 30 minutes at 100°C. This step allowed the photoresist to harden and remain on the silicon surface the duration of dry etching.

Next, through holes were formed in the silicon substrate using Bosch process for deep reactive ion etching (DRIE) [71]. To accomplish the silicon etching, an Alcatel AMS 100 SDE was used. The DRIE recipe used in this process was: etch step-- SF_6 at 300 sccm with 3 seconds cycle; passivation step—C_4F_8 at 200 sccm and O_2 at 20 sccm with 1.4 seconds cycle; pressure—5.25×10^{-1} mTorr; source generator power—2400 W; substrate holder power—used in pulsed mode, high cycle at 90 W for 20 ms, low cycle at 0 W for 80 ms; substrate holder He pressure—9.75×10^{-3} mTorr. In this process, the wafer was cooled down to -15°C and the 300 μm deep vias where then etched through for 30 minutes; which converted to an etch rate of 10μm/min. During this etching process, the through holes were formed and the photoresist remained on the silicon surface on the remaining substrate areas. The resist provided a protective layer for the excess

silver paste that is present during the metallization process. The figures below illustrate front and backside images of the micro-coaxial probe post DRIE.

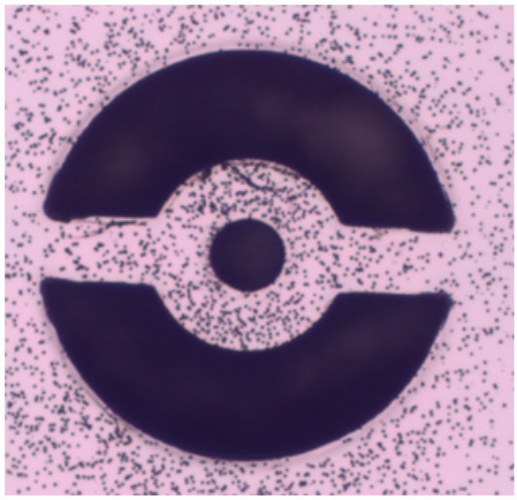

(a)

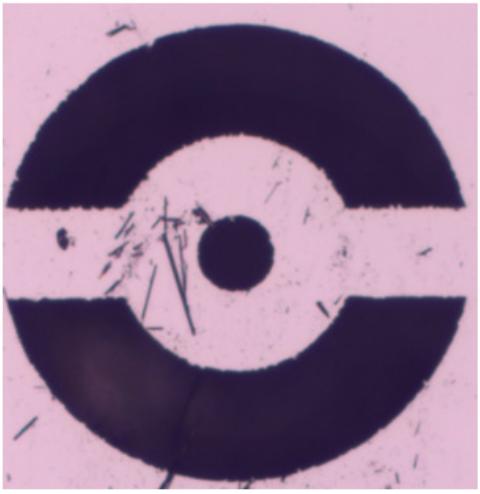

(b)

Figure 4.15 Microscopic images of micro-coaxial probe post through-hole DRIE. (a) Front side and (b) Backside.

It can be seen in the front side image that due to the DRIE process small areas of the photoresist were slightly burnt, which produced tiny black dots on the surface. These dots however, did not play a major effect on the filling process of the holes. Also, in Figure 4.15 (b), a glossy discoloration on the surface of the silicon may appear which is bonding oil that was used to secure the wafer to the 2 inch holder. If enough oil is not applied, the topside of the wafer will

burn completely, damaging the devices. The only disadvantage of the oil was the difficulties of trying to remove it from the surface. This caused a minor issue in future processing steps and will be discussed in later sections.

4.6.2 Through-Hole Metallization Process

After the holes were etched through, a metallization step was performed to fill them with silver paste. This was achieved using diluted silver paste and a sharp razor blade which coursed the metal into the miniature hole. In this process, a thick amount of silver paste was applied to the silicon surface and the razor blade was swept across the holes, evenly distributing the metal inside the formed through holes. This step was performed repeatedly to ensure that the metal was being filled not only through the holes, but also along the edges within coaxial structure. The surface resistance of the paste was also studied over a 5-day period to ensure it would not have an effect on the signal transmission abilities of the coaxial probe. During the study, it was verified that the paste maintained a surface resistance value between 1.2 and 1.3Ohms proving it had no effect on the behavior of the probe. Once this filling was complete, the substrate was submerged in acetone, removing the remaining photoresist and the silver paste from the surface. Figures 4.16 (a) and (b) below illustrate front and backside Scanning Electron Microscope (SEM) images of the micro-coaxial probe following the metallization of the holes using the diluted silver paste. To verify the holes were completely filled through the silicon substrate, a cross-section of the coaxial probe can be seen in the SEM image in Figure 4.17.

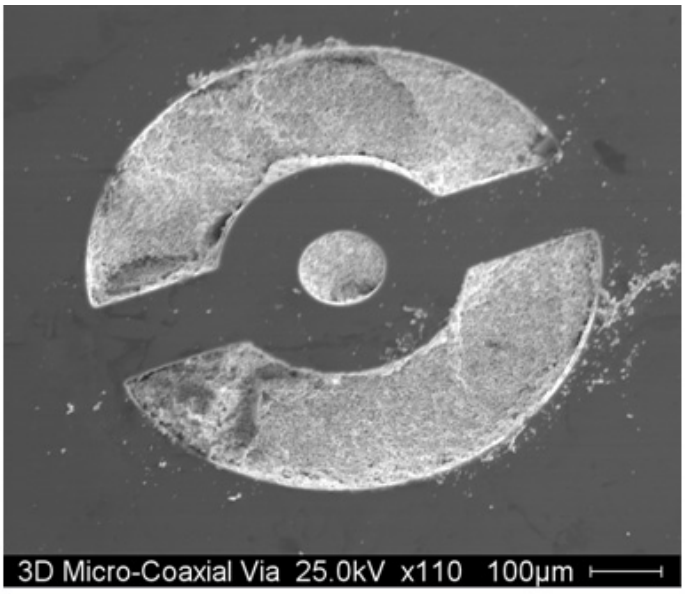

(a)

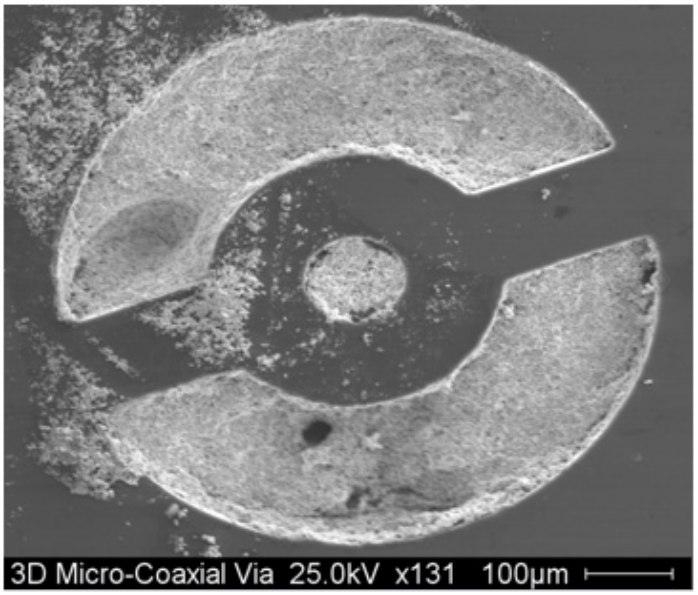

(b)

Figure 4.16 SEM images of micro-coaxial probe post through-hole metallization. (a) Front side and (b) Backside.

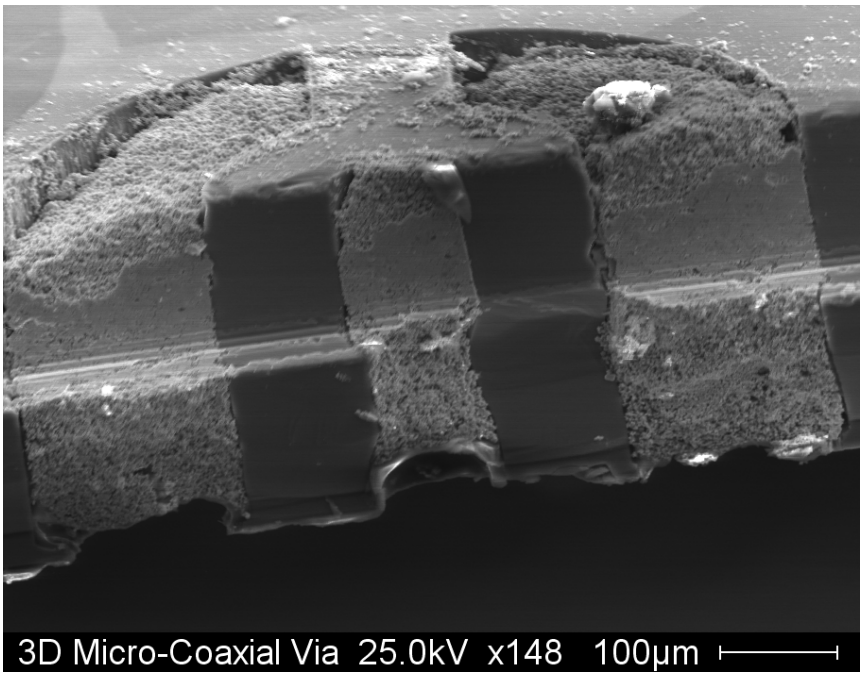

Figure 4.17 Cross-section SEM image of micro-coaxial probe post through-hole metallization.

In the cross-section view above, it can be seen that the inner and outer coaxial conductors are filled through the depth of the substrate, creating the 3-dimensional probe structure. This image was captured by simply dicing the probe directly down the center of its architecture, allowing a side profile view of both conductors.

4.6.3 Fabrication of CPW Lines

Next, an additional photolithography step was performed to pattern the CPW configuration lines on the top and bottom side of the substrate. The wafer with metalized through holes was spin coated with NR9-3000PY negative photoresist at 1000 rpm for 30 seconds at 20 acceleration and then soft baked for 1 minute at 150°C. This is a very thin resist with a fast developing time and works well during liftoff process. The original recipe was modified however, to allow even distribution of the resist across the surface, which helped prevent a poor development and deposition. Next, the wafer was exposed using the Karl Suss mask aligner for 23 seconds at 25mw/cm^2 and hard baked for 1 minute at 100°C. The wafer was then developed in

RD6 for 10 seconds. This developer time had to be reduced due to the unbalanced surface within the coaxial structure, which caused for an additional negative resist layer to be applied. Following this lithography process, an electron beam evaporator was used to deposit the metal on the CPW line patterns. First a chrome (Cr) layer of ~15nm was deposited at a rate of 0.3A/sec and acted as an adhesion layer for the top gold (Au) layer. The Au layer had a thickness of ~300nm and was deposited at a rate of 2A/sec. Finally, a liftoff process was performed by placing the substrate in acetone overnight which removed the remaining Au from the silicon surface. It is important to note that this entire process was repeated to include the CPW lines on the backside of the wafer. Figure 4.18 (a) and (b) illustrates front and backside microscopic images of the fabricated micro-coaxial probes with gold CPW lines.

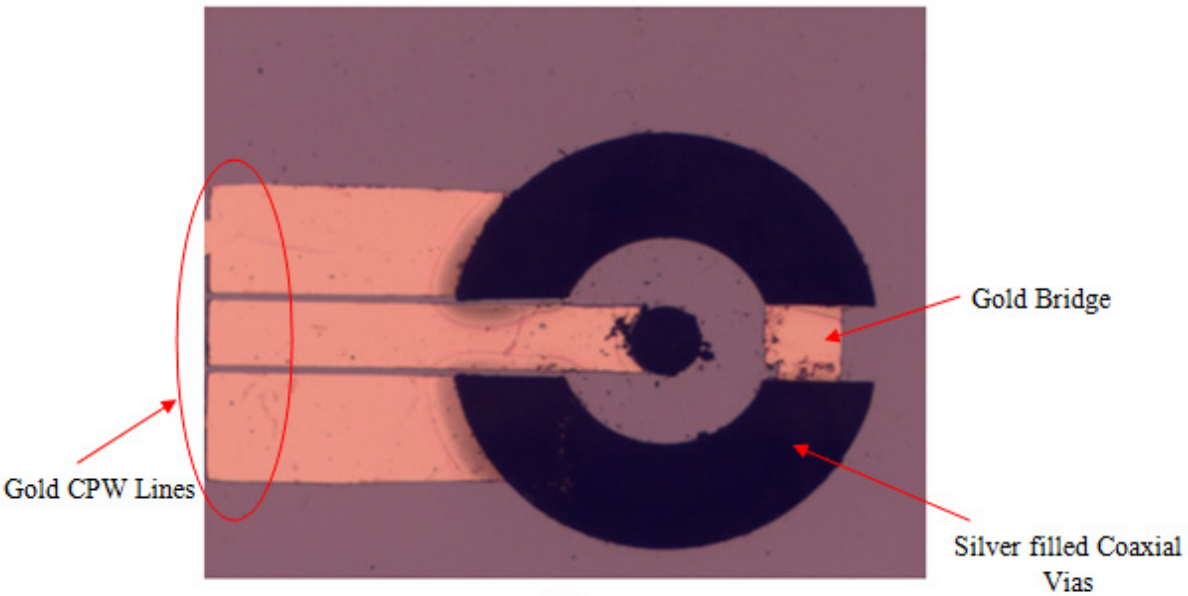

(a)

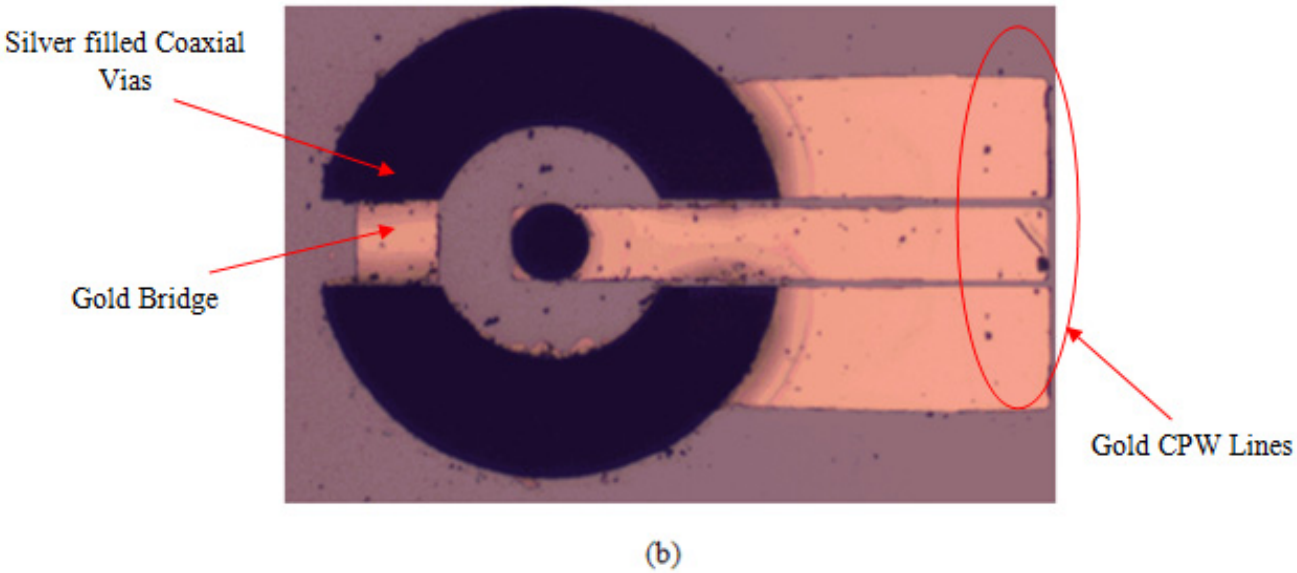

Figure 4.18 Microscopic images of fabricated micro-coaxial probe with gold deposited CPW lines. (a) Front side and (b) Backside.

4.7 RF Characterization Setup and Substrate Orientation

The RF characterization of the coaxial probe is a very crucial part of this work. When the device demonstrates excellent signal transmission at low and high frequencies and over a wide bandwidth, it verifies its use for a two-fold application. These characterization results indicate the frequency range that the probe can operate in when used in millimeter wave packaging systems. Furthermore, demonstrating a good reflection coefficient will provide more accurate measurements on the unknown materials.

There are several device components that were used to perform the required RF characterization of the coaxial probe. Figure 4.19 illustrates test setup utilized during the characterization of the micro-coaxial probe.

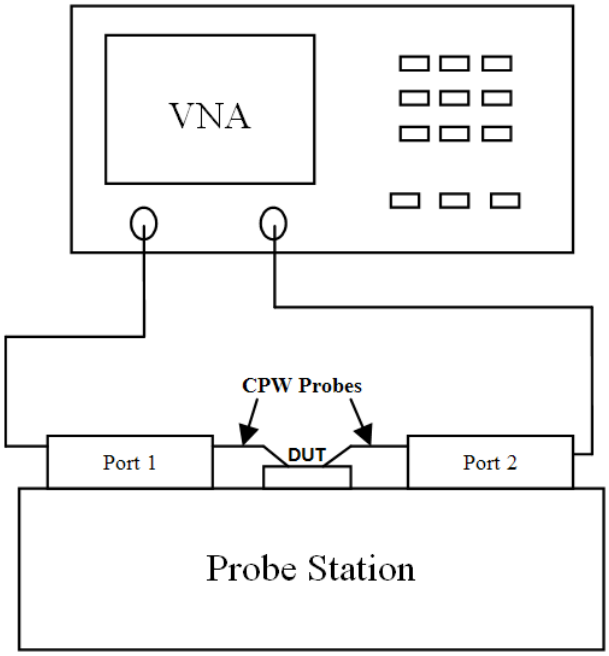

Figure 4.19 Illustration of Test Setup used for RF Characterization of Micro-Coaxial Probe.

The measurement setup in the figure above demonstrates all equipment used during RF characterization. The fabricated micro-coaxial probe (DUT) was first placed on a probe station that contain ports 1 and 2. Each port was then connected to ground-signal-ground (CPW) pitch probes which are used to characterize the device. Next, V-band cables, capable of measuring up to 67 GHz, where connected from the 2 ports of the vector network analyzer (VNA), to the ports located on the probe station. Lastly, a calibration was performed on the probe-to-cable connection to eliminate any parasitic effects that may affect the measurement results. This calibration removes nearly all of the signal loss present from the VNA ports to the tip of the ground-signal-ground pitch probes.

The sections below provide brief descriptions of each RF component used in the characterization test setup:

Cascade Microtech Probe Station:

The micro-coaxial probes were characterized using the Cascade Microtech probe station shown in Figure 4.20. This is a highly-precise manual probe system for wafers and substrates that

supports a wide variety of systems such as device characterization, submicron probing, mm-Wave and sub-THz measurements, etc [72]. Its stable platen is designed to accommodate up to sixteen different positions.

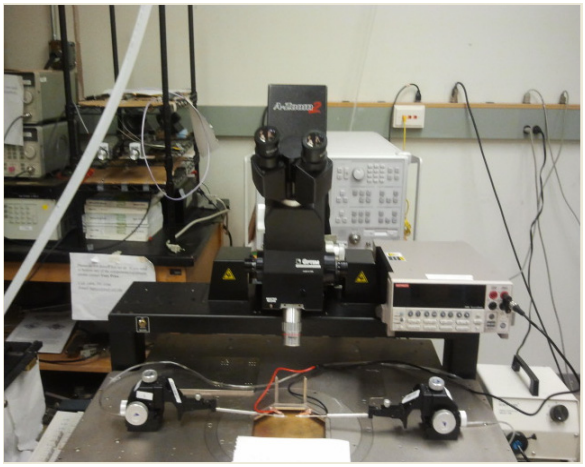

Figure 4.20 Cascade Microtech Probe Station used during micro-coaxial RF characterization.

The devices were probed during measuring using the Micromanipulator High Frequency Picoprobes shown in Figure 4.21 [73]. These probes include ground-signal-ground tip configuration suitable for CPW feeds, and a pitch distance of 150μm. The probes were also passive, not requiring any power supply and are suitable for frequency from dc up to 67GHz.

Figure 4.21 Micromanipulator High Frequency Picoprobes with ground-signal-ground tip configuration used to connect to CPW feed.

The reflection coefficient and transducer gain were determined using an Anritsu 37397 VNA shown in Figure 4.22(a) which is capable of measuring up to 64 GHz and communicated via computer. This communication was achieved by connecting an IEEE 10833B GPIB cable [74] to the appropriate computer port. V-band cables were also used to connect the VNA to the probe tip to convey the measured data and are shown in Figure 4.22(b) below.

(a)

(b)

Figure 4.22 RF Components used to determine reflection coefficient and transducer gain of micro-coaxial probe. (a) Anritsu 37397 Vector Network Analyzer and (b) High Frequency V-band Cable.

4.7.1 V-Band Cable Calibration

In order to eliminate any signal losses present in the V-Band cable, a CS-5 calibration was performed on ports 1 and 2. This allowed the VNA to collect data directly from the devices, by shifting the reference plane to the edge of the probe tips. Figure 4.23 below shows each calibration standard that was measured which included a short, open, load, and thru, also known as "SOLT." Once these standards were measured, the losses in the cable were de-embedded to the reference plane of the devices.

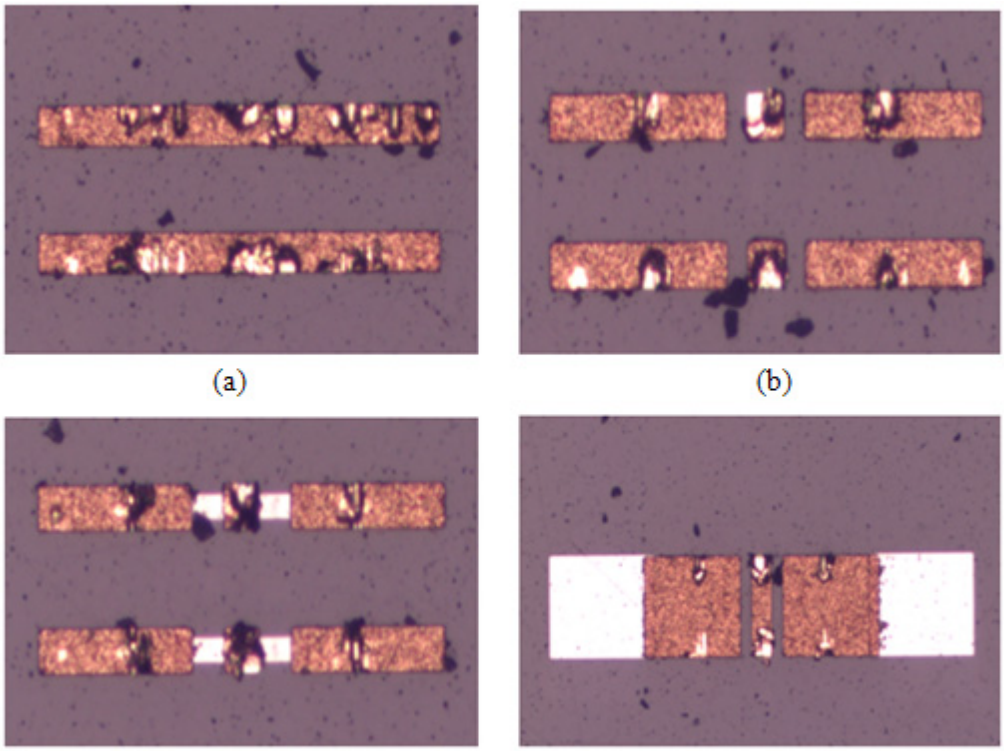

Figure 4.23 CS-5 Calibration Standards used for v-band cables. (a) Short, (b) Open, (c) Load, (d) Thru.

The short standard consists of two gold lines that behave as inductors, whereas the opens have two gaps in between the gold lines which allow capacitance to flow through. The load includes two 100Ω resistors in parallel between the lines which are equal to 50Ω a piece. Lastly,

the thru standard consists of thick open lines that enable ports 1 and 2 to be probed at the same time and connected together via an RF signal.

4.7.2 Additional Substrate Alignment for Bottom CPW Lines

To determine the reflection coefficient and transducer gain of the micro-coaxial probes, a two-port measurement was performed. The probes at port 1 were easily connected to the devices; however, port 2 was impossible to reach. This is true because the CPW lines for port 2 were located on the backside of the silicon substrate, which prevented them from being probed during measuring. To accommodate for measurements at port 2, an additional silicon substrate was used to extend the CPW lines on the bottom of the original substrate. However, getting the CPW lines on both substrates aligned properly became another issue. To properly measure the coaxial probe without any losses present from the CPW line integration, the lines on the backside of the top substrate needed to be carefully aligned to those on the additional substrate. This was achieved by designing two mask layers using AutoCAD [75]: the first mask layer included "local" alignment marks (individual circles) which surrounded the coaxial probe on the top substrate. These local marks were then etched through the substrate and served as windows that allowed a visual to the alignment marks on the additional substrate. Following this, another mask layer was included on the additional substrate which served as "bottom" alignment marks (cross hairs). These mask layers were then integrated by aligning the cross hairs of the "bottom" layer to the circles of the "local" layer. Once these layers were aligned, this verified that the CPW lines were properly aligned to one another and measurements could be made with minimum signal loss present in between lines. These masks layers allowed the coaxial probe to be measured using both ports. Figure 4.24 below illustrates the two mask layers used to align the CPW lines on the top and bottom substrate.

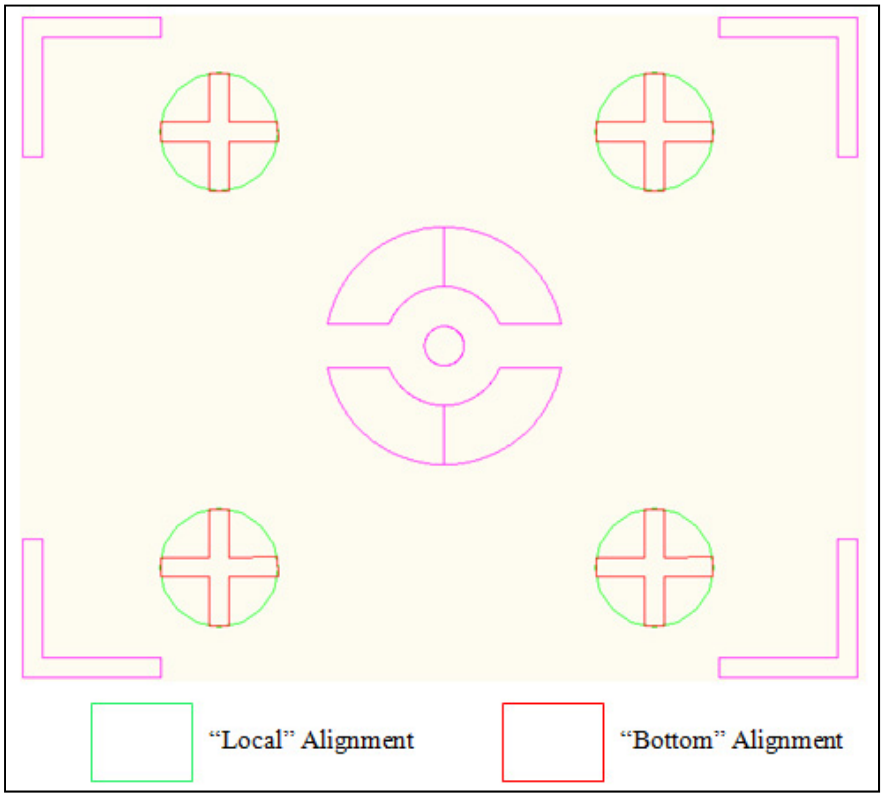

Figure 4.24 Illustration of Mask design with "local" and "bottom" layer alignment marks.

From the image above it can be seen that when the two substrates are integrated together, a clear window will be present allowing the two marks to be properly aligned to one another.

Prior to finalizing the above mentioned mask design the original simulations were optimized to ensure the micro-coaxial probe would behave properly when the additional substrate was integrated. These simulations were also performed using HFSS, which helped determine any additional losses that could be present as the RF signal traveled through the coaxial signal lines to the CPW signal lines. By introducing a sandwich type configuration to the device, the risk of undesirable propagation increases; this is due to the thickness of the silicon substrate being used at high frequencies. The figure below illustrates the design layout of the vertical micro-coaxial probe substrate integration. It should be noted that the additional substrate consisted of the same CPW dimensions as the original, with a thickness of 300µm.

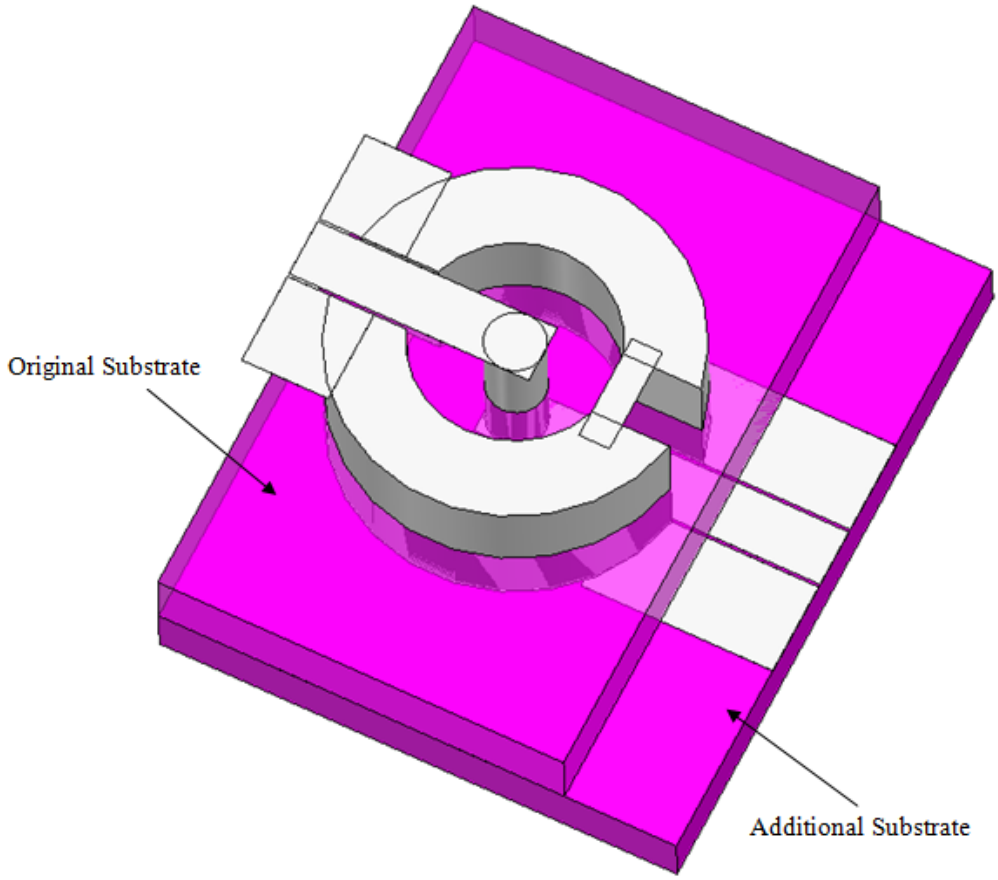

Figure 4.25 Layout of 3D Vertical Micro-Coaxial Probe Integrate with additional substrate for CPW alignment.

The figure above shows that by extending the CPW lines on the additional substrate, the measurement at port 2 can be achieved. The simulated response of the reflection coefficient and transducer gain for the substrate integration is shown in Figures 4.26 (a) and (b). The results are compared to the original simulations and indicate signal loss at some frequency levels which was expected. The losses from the reflection coefficient are mainly present in the device in the range from 20 GHz to 40 GHz and beyond the 60 GHz range. This discovery does affect the behavior of the coaxial probe in some extent but mainly in the application of millimeter wave packaging systems. However, this does not indicate that the device will not function in this range of frequency when measured or when used for high frequency device characterization; it simply

means that it will not achieve maximum performance near that particular spectrum, ultimately limiting its range of performance.

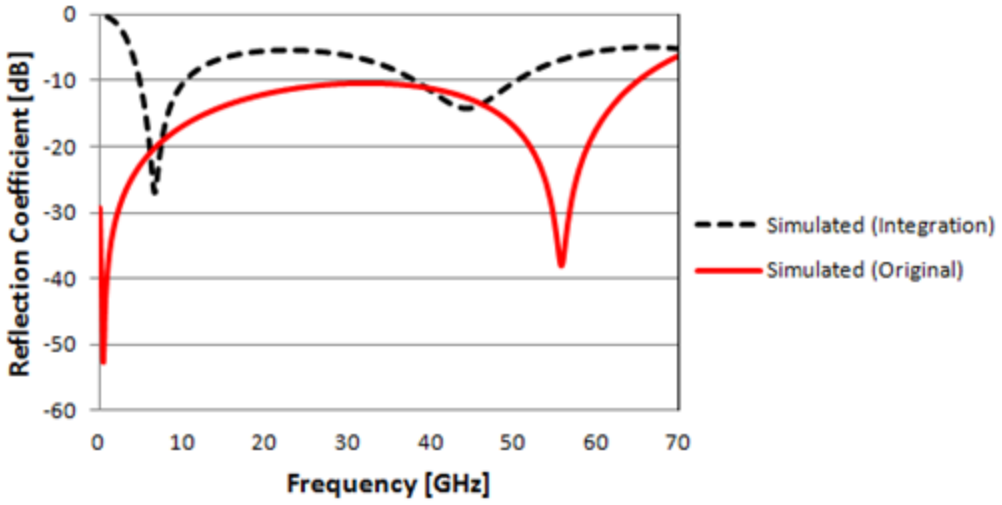

(a)

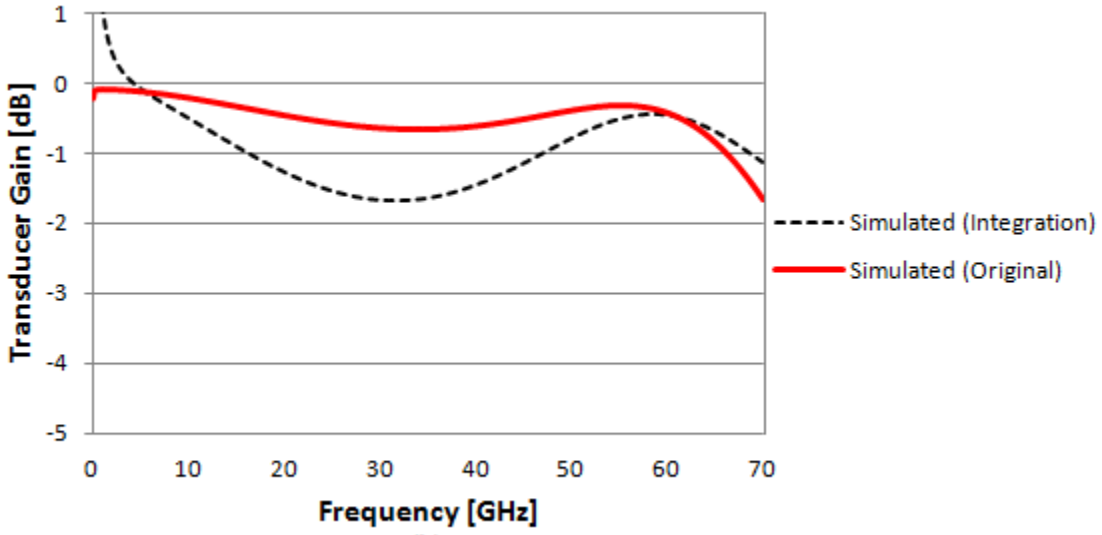

(b)

Figure 4.26 Simulated response of micro-coaxial probe following substrate integration (vs. original). (a) Reflection Coefficient (Fig. 4.9) and (b) Transducer Gain (Fig. 4.10).

The transducer gain presented in the figure above was also compared to the original simulations and indicates additional losses that may be present at high frequencies when integrating the coaxial device with the additional substrate. Aside from the region near DC

frequencies where non-physical simulation artifacts are dominant, the signal decreases from the original near the -2dB range between 20 GHz and 50 GHz but improves near 60 GHz. These results indicate that integrating the substrates can impact the behavior of the probe when used in packaging systems, but not as much when characterizing materials. It is important to note however, that when integrating the probe with commercial packaging applications, the use of an additional substrate will be eliminated and maximum device performance can be successfully recovered.

Figure 4.27 below illustrates a microscopic image of the additional substrate with the CPW line extension and "bottom alignment marks that will be used integrate the substrates. The image shows the same identical gold CPW lines patterned on the additional substrate as those that were patterned on the top substrate.

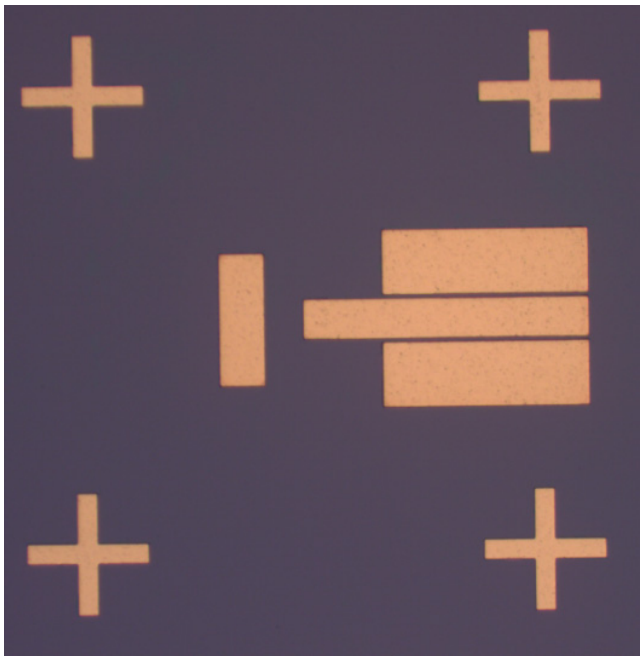

Figure 4.27 Microscopic image of additional substrate with gold patterned extended CPW lines and "bottom" alignment marks used for integration.

A microscopic image of the top substrate with etched local alignment holes can be seen in Figure 4.28. These holes were also etched using the DRIE recipe described in previous sections, and

were aligned to the cross hair marks on the bottom substrate which contained the extended CPW lines for measuring.

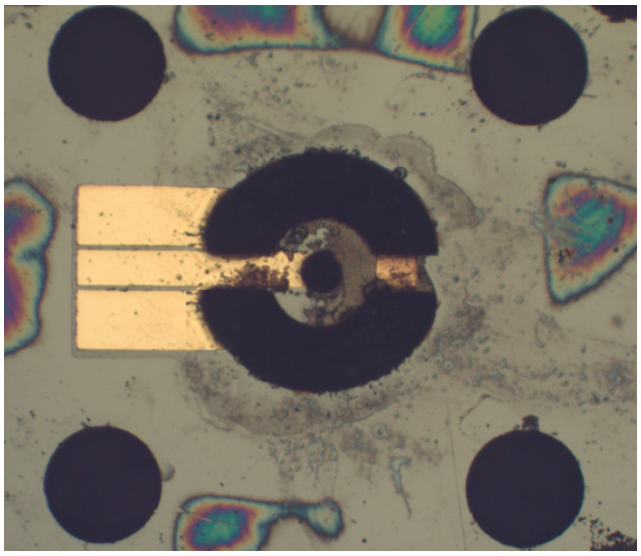

Figure 4.28 Microscopic image of top substrate with etched local alignment holes used to align with bottom cross hairs.

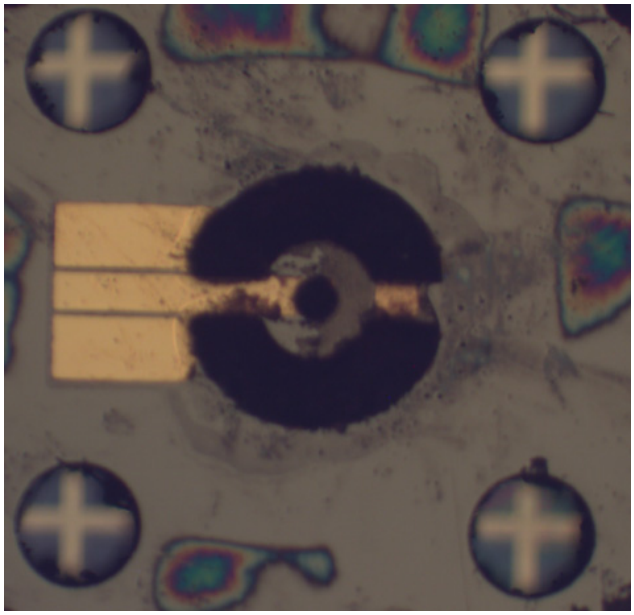

Figure 4.29 Microscopic image of substrate integration with top local alignment holes and bottom cross hairs used to extend CPW lines for RF characterization.

The figure above illustrates the two substrates (top and bottom) being integrated in order to access port 2 during the RF characterization. It can be seen that the local holes on the top

substrate were aligned to the cross hair marks on the bottom substrate. This alignment served as verification that the extended CPW lines on the bottom substrate were nearly aligned to the CPW lines on the backside of the top substrate.

4.8 Micro-Coaxial Probe Characterization and Data Analysis

After properly integrating and aligning the substrates, RF characterization was performed on the coaxial probe. Measurements were performed over a wide frequency range from dc-to-65 GHz. The reflection coefficient and transducer gain of several micro-coaxial probes were measured to get more accurate results. Probe results were compared to the simulated responses obtained during substrate integration because both substrates were included during analysis.

The measured results of the micro-coaxial probes are shown in Figures 4.30 (a) and (b). When measuring the reflection coefficient, most of the probes seem to demonstrate good results compared to simulations with more than -10dB loss difference at high frequencies from approximately 15 GHz-to-57 GHz. At lower frequencies (dc-to-10 GHz) however, majority of the signal received from port 1 was reflected back and passed the -10dB mark, which demonstrates a poor signal transmission. Probes 2 and 3 provided the best results with reflection coefficients greater than -15dB over 20 GHz bandwidth; only decreasing less than -10 dB at 40, 50, and 60 GHz. Probes 1 and 4 had good reflection as well but did not sustain performance over a wide frequency range.

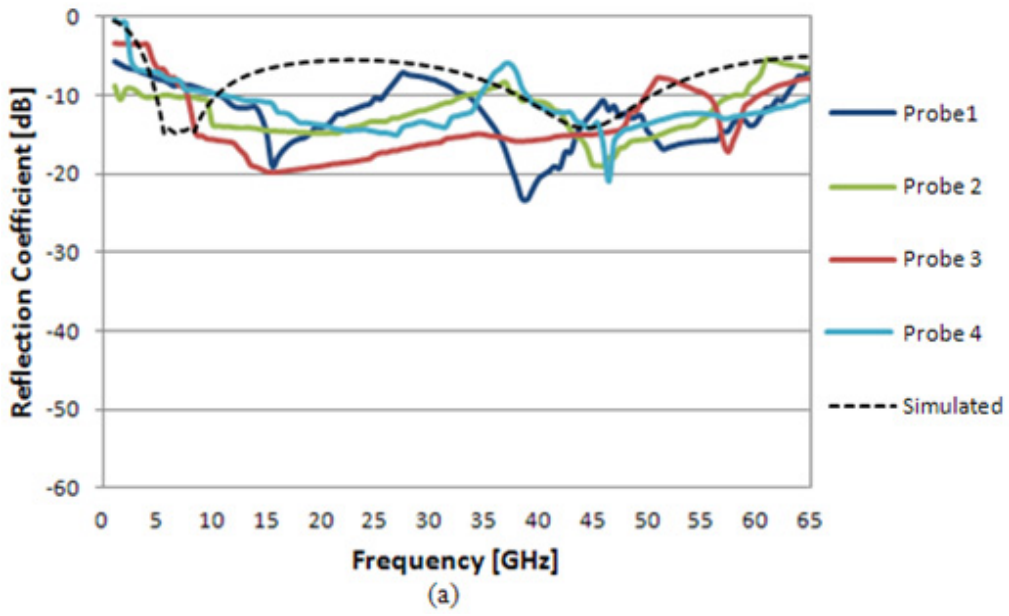

(a)

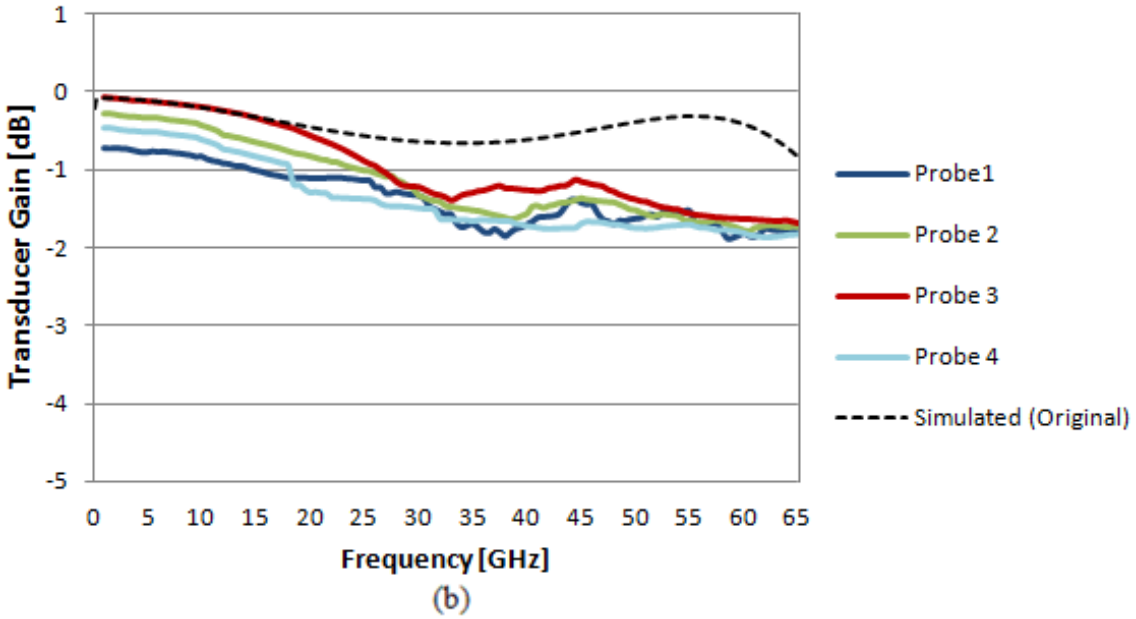

(b)

Figure 4.30 Measured results of micro-coaxial probe vs. simulated response with substrate integration. (a) Reflection Coefficient and (b) Transducer Gain (Fig. 4.10).

The measured results for the transducer gain of the coaxial probes are shown in Figure 4.30 (b) above. It can be seen that all four probes behaved well from dc-to-40 GHz, demonstrating less than -1.5 dB which was very close to the simulated results. This proves that the probes have good signal transmission between the two ports and would provided minimal loss

when integrated with other multi-layer high frequency devices. Beyond 40 GHz however, the probes performance began to decrease nearly reaching -2 dB of transducer gain. This behavior did not agree well with simulation, where the transducer gain increased to nearly -0.5 dB from 50-to-65 GHz. This was a critical discovery because it altered the probes signal transmission abilities at higher frequencies. Since the probe was specifically designed to behave well over a wide range of high frequencies, further studies were conducted to determine the cause of the degrading signal.

During the substrate alignment, it was discovered that even when the local holes are centered with the bottom cross hairs, a slight misalignment still occurred. This is due to the fact that while the probes were being measured, the top substrate shifted slightly because of the pressure of applied from the CPW probes. This minor shift caused the CPW lines on the backside of the top substrate and additional substrate to misalign by about 2-3µm, which is perceived to be what created the discrepancy between the measured and simulated data. To verify this assumption, an additional simulation was performed for the transducer gain when the two substrates were slightly misaligned. The figure below illustrates the transducer gain response when the top and additional substrates were simulated with a 2-3µm misalignment.

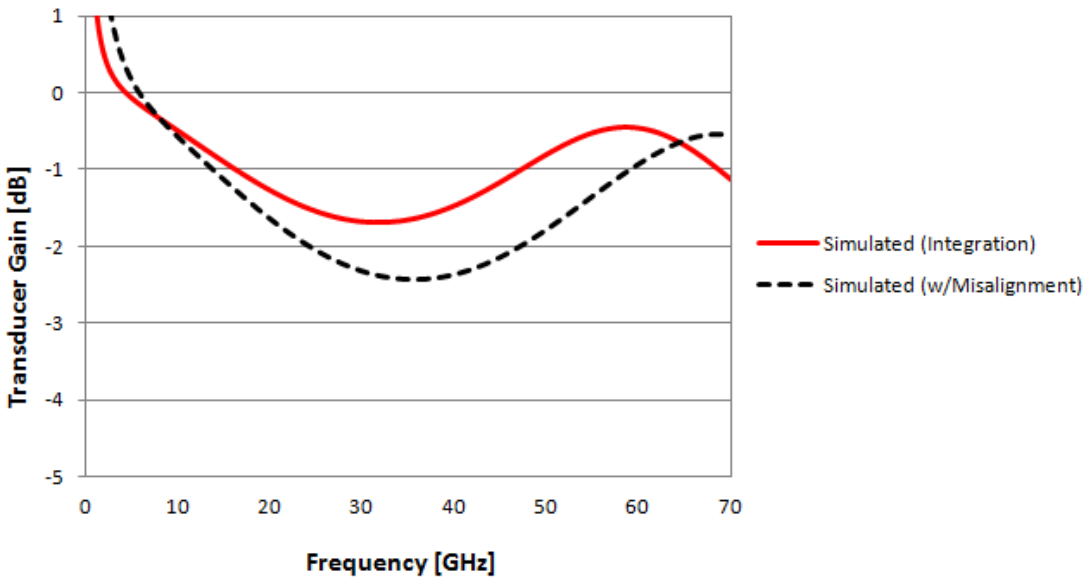

Figure 4.31 Simulated transducer gain (Fig. 4.10) of micro-coaxial probe with additional substrate misalignment.

The results above illustrate the probe response with the substrate misalignment compared to the probe's first integration simulation data. From the results it can be seen that, aside from the region near DC frequencies where non-physical simulation artifacts are dominant, by misaligning the additional substrate with the top substrate, the transducer gain decreased a bit more as it approached higher frequencies. This is occurred because as the signal was transmitted from port 1 to port 2, the slight misalignment between the sets of CPW lines created a significant amount of losses through the deposited metal which consequently impacted the device performance. These results verified the theory that a substrate misalignment occurred during the measuring of the coaxial probes. The simulated misalignment and measured data comparison can be seen in Figure 4.32 below.

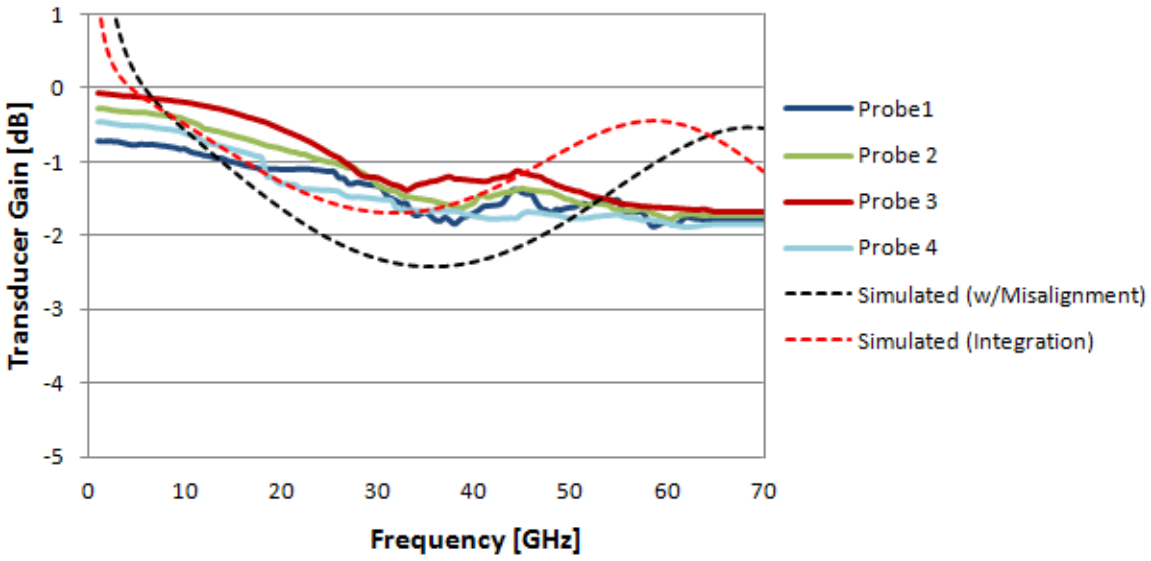

Figure 4.32 (as stated in 4.10) Measured results of micro-coaxial probe compared with additional substrate integration and misalignment.

The figure above shows the measured probe data compared to the substrate integration and misaligned simulated results. It can be seen that the measured data did agree with the misaligned simulated results by decreasing at higher frequencies. The measured results now closely resemble the behavior obtained during the misalignment simulation at high frequencies; therefore, it was determined that the variance between the integrated simulation and measured data was due to a misalignment with both substrates. However, possible voids in the through holes following the paste metallization could have also caused the measured probe results to differ from simulated. Additionally, the gap in the ground conductor where the bridge was located may have also caused the difference in results, due to the coaxial structure being open and vulnerable to unwanted capacitances.

In summary, several through wafer 3D micro-coaxial probes were designed flushed in a silicon substrate. The probes were designed to operate at high frequencies and simulated using HFSS. The fabrication techniques were identified and the probes were developed using photolithography. The probe vias were filled with silver paste using a novel approach and the CPW lines were fabricated using e-beam deposition. Finally, the probes were measured to

determine their reflection coefficient and transducer gain response. Results confirmed that the probes had good behavior when transmitting a RF signal between two ports. These results verified that the micro-coaxial probe can successfully be integrated in millimeter wave packaging technologies as high frequency transitions. By eliminating the need for thermal or compression bonding, the probes present a low-cost and durable design that can produce high input/output ratios that are ideal for commercial products.

CHAPTER 5

MICRO-COAXIAL PROBE INTEGRATION FOR HIGH FREQUENCY MATERIAL CHARACTERIZATION

The characterization of materials electrical properties at high frequencies using a coaxial probe are determined when the unknown material comes in contact with the probe device [34, 76, 77]. This contact provides the unknown material with microwave signals that helps determine its electromagnetic fields; which are then used to deduce the reflection coefficient of the material at a defined reference plane. To accomplish the above mentioned characterization, the micro-coaxial probe in this work was integrated with unknown materials to determine their electrical properties over a broadband at high frequencies. Following the measurement, a data interpretation method was implemented in order to determine the permittivity of the unknown material. The interpolation method will be discussed in detail in the upcoming sections. This chapter includes a detailed description of the micro-coaxial probe's integration with specific materials, the method of data interpretation for determining permittivity, high frequency characterization setup, and a comparison of simulated to measured results.

5.1 Probe Integration Modeling with Unknown Materials

In Chapter 4, the micro-coaxial probe was introduced and to verify its ability to measure materials, RF characterization was performed and discussed in detail. In this chapter, the same probe was used to characterize unknown materials at high frequencies. As mentioned earlier, the inner conductor of the micro-coax, which provides the signal to the system, was made of silver. The outer conductor was also made of silver at 150µm width and was used as a metal ground to complete the probes metal/dielectric/metal topology. To reduce the propagation of higher order modes, the coax was designed with an inner and outer diameter of 100µm and 300µm.

The integration of the coaxial probe with the material for characterization has several factors that play a major role in getting accurate results. When the probe is placed in contact with the unknown material, electromagnetic waves are directed to the material under study using a VNA and the permittivity of the MUT is deduced from its measured reflection coefficient. [78-80]. Additionally, when measuring the electrical properties of materials at high frequencies, the thickness of those being measured begin to influence the permittivity measurements if they are not chosen properly. In [28], it is recommended that the material under study be thicker (double) than the length of the probe to prevent it from influencing any permittivity measurements. Therefore, all materials used in this work were chosen to be 1.3mm. The first 3 materials used in this work were: Rogers 3006 and 3010 High Frequency Laminates [81], and a Rogers FR-4 laminate sheet [82]; and were known materials used to calibrate the measurement system. These materials were chosen due to their use in applications up to 77 GHz, which surpasses the frequency range chosen for this work. Known materials were necessary because in order to determine the permittivity of an unknown material using its measured reflection coefficient data, materials with known electrical properties needed to be included in the data interpretation system. This interpretation system will be discussed in further detail in the next section. Following the selection of the 3 known materials, Silicon [83] and Polydimethylsiloxane (PDMS) [84] were chosen as the unknown materials to be characterized due to their increasing demand in high frequency applications. Figure 5.1 below illustrates an example of the micro-coaxial probe being integrated with an unknown material for high frequency characterization.

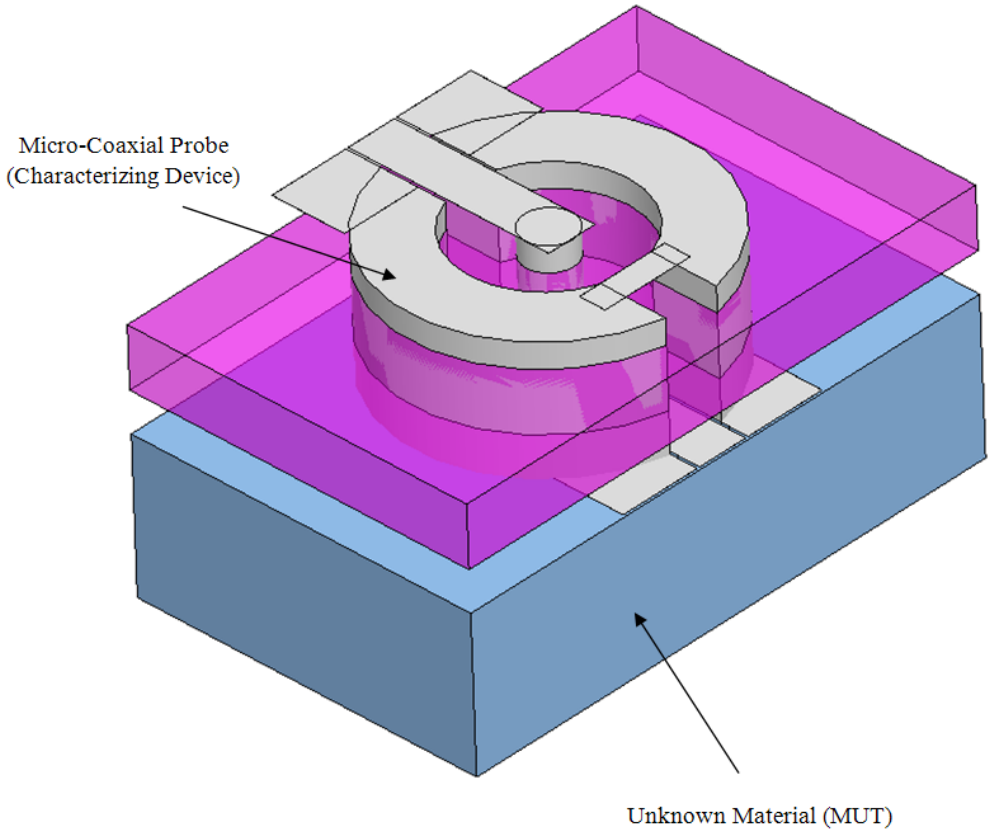

Figure 5.1 Model of 3D Micro-Coaxial Probe being integrated with a bulk unknown material and used as a characterization device.

5.2 Data Interpretation Using Cross-Ratio Invariance Coding Technique

Researchers in the past have used various codes and techniques to determine the permittivity of unknown materials when measuring its reflection coefficient data [85-92]. These techniques consist of numerous variables and equations that allow the permittivity of materials to be determined at high frequencies when measured in contact using a coaxial probe. Nevertheless, this research used a cross ratio invariance coding technique [93]; which utilized theoretical equations and a material calibrated system to deduce the permittivity of unknown materials using its measured reflection coefficients. This method was chosen because it consisted of stationary formulas for open-ended coaxial lines terminated by a semi-infinite medium on a ground plane.

Since the materials were measured using a micro-coaxial probe, these theoretical equations were implemented to determine the permittivity.

After implementing the cross-ratio coding technique, the permittivities of the unknown materials were determined using the following process: The measurement system was first calibrated by measuring the reflection of 3 known materials; which as mentioned previously, were Rogers 3006 and 3010 high frequency laminates, and a Rogers FR-4 laminate sheet. These materials were all chosen to be 1.3mm thick to avoid any propagation through the surface, which would alter the reflection data and ultimately the permittivity results also. Next, the aperture admittance of these values were calculated and they denoted as Y_1, Y_2, and Y_3 in the system calibration equation below [94]:

$$\text{Solve for } Y_s \qquad \frac{Y_s - Y_1}{Y_s - Y_2}\frac{Y_3 - Y_2}{Y_1 - Y_3} = \frac{\Gamma_s - \Gamma_1}{\Gamma_s - \Gamma_2}\frac{\Gamma_3 - \Gamma_2}{\Gamma_1 - \Gamma_3} \tag{5.1}$$

In the equation above, Γ_1, Γ_2, and Γ_3 represent the measured reflection coefficients of the 3 known materials. The reflection coefficient of the unknown material being characterized is then measured and denoted as Γ_s in the equation above. Using the calibrated standards, the equation is then solved for Y_s, the admittance of the unknown material. Lastly, the permittivity of the unknown material is determined by solving for $\boldsymbol{\varepsilon}^*$ in the quasi-static approximation for the aperture admittance of an open-ended coaxial line terminated in a semi infinite-medium [94]:

$$Y_L \approx j - \frac{2\omega I_1}{\left[\ln(b/a)\right]^2}\varepsilon^* - j\frac{\omega^3 \mu_o I_2}{\left[\ln(b/a)\right]^2}\varepsilon^* + \frac{\pi\omega^4 {\mu_o}^{3/2}}{12}\left[\frac{b^2 - a^2}{\ln(b/a)}\right]\varepsilon^{*(5/2)} \tag{5.2}$$

Where a and b are the inner and outer radii of the coax and μ_o is the permeability of free space. The admittance of the unknown material Y_s=Y_L, the angular frequency of the electromagnetic fields is represented by ω, and I_1 and I_2 are constants. The equation is finally solved for the

complex permittivity of the unknown material which is represented by ε^*, and can also be written as the equation below [95]:

$$\varepsilon^* = \varepsilon' + j\varepsilon'' \tag{5.3}$$

Where ε' represents the real part of the materials permittivity and ε'' represents the imaginary. It is important to note that the above equations were solved in detail and the permittivity of each unknown material was deduced using the coding technique in [96]. The entire coding technique is shown in Appendix C.

5.3 Characterizing of Known Materials – Simulated Reflection Coefficients

In this work, the fabricated CPW lines on the top and bottom side of the micro-coaxial probe were used to determine the reflection data from the known and unknown MUT's. By bringing the bottom CPW lines in contact with the MUT, the reflection coefficient of that material over a wide frequency range was determined. Firstly, the reflection coefficients (real and imaginary) of the 3 known materials were simulated when in contact with the micro-coaxial probe using HFSS. This simulation was performed because it provided an expected data range for each known material, which helped verify that the micro-coaxial probe was successfully integrated and in contact with the MUT during measuring. Without performing these simulations, the materials under test would be measured using the coaxial probes and it would be difficult to determine if their reflection coefficient results were realistic prior to inputting the data in the cross-ratio code. The figures below illustrate the real and imaginary simulated reflection coefficients of the 3 known materials. As mentioned earlier, each material simulated in contact with the micro-coaxial probe, had a thickness of 1.3mm to improve the accuracy of results.

It is important to mention that any known and unknown materials with simulated reflection values greater than 1 at lower frequencies, demonstrated non-physical data due to simulation errors that occurred when the probe was placed in contact with the materials. These

errors could mainly be contributed to the fact that the mesh solution in the simulation was converging with the following settings: converged passes-2, minimum passes-5, maximum passes-20, and maximum deltaS-0.02. Therefore, the cause of this non-physical behavior could be due to the need to adjust the convergence criteria to allow the simulation to properly calculate the mesh solution for each adaptive pass. Another possibility is that the properties in the simulation software for each material may have created reflection issues with the probe at low frequencies, causing an error in the data solution. Perhaps editing these material properties could have reduced the amount of reflections present when in contact with the coaxial probe. Also, the thickness of each characterized material could have created issues for the simulated data set. Although a bulk thickness of ~1mm was chosen, this could have been an issue for some of the results.

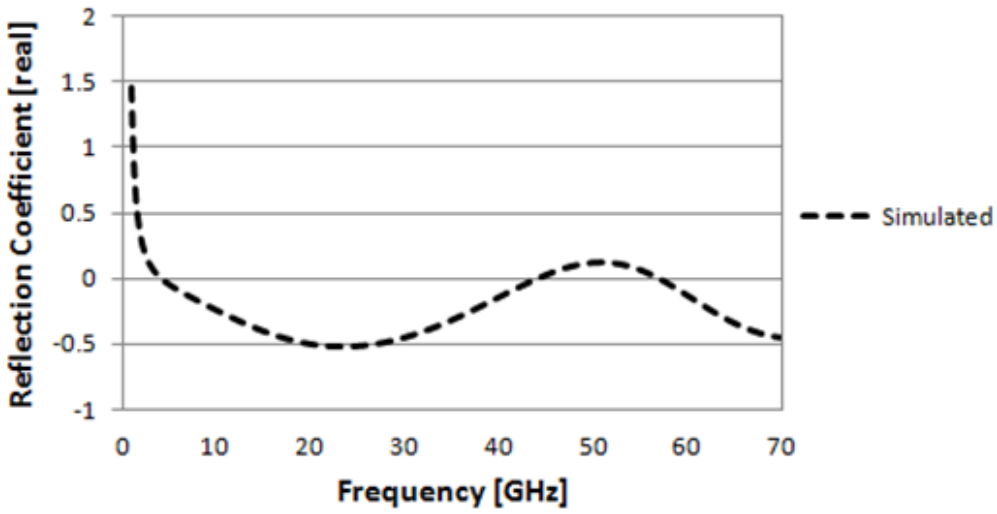

(a)

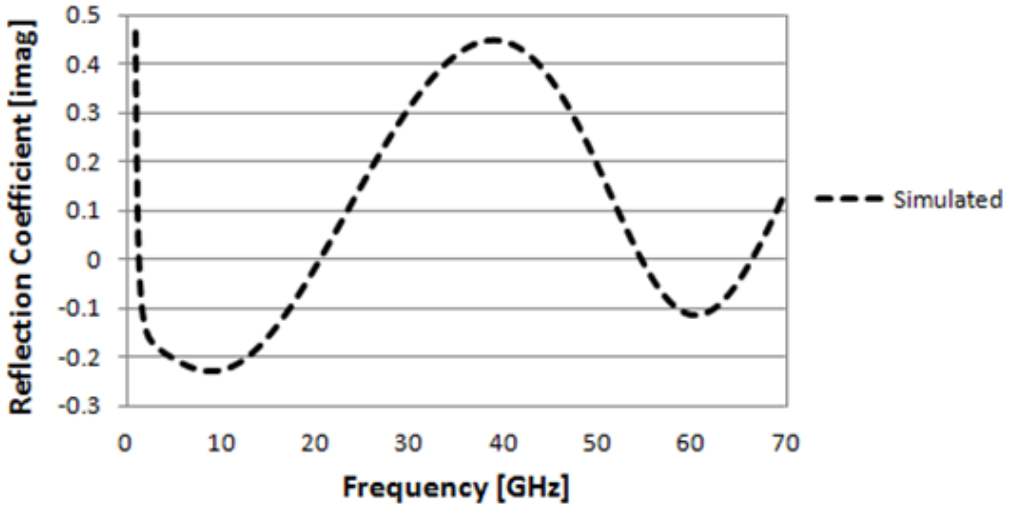

(b)

Figure 5.2 Simulated results of micro-coaxial probe characterizing the Rogers FR-4 laminate sheet at high frequencies. (a) Real Part and (b) Imaginary Part.

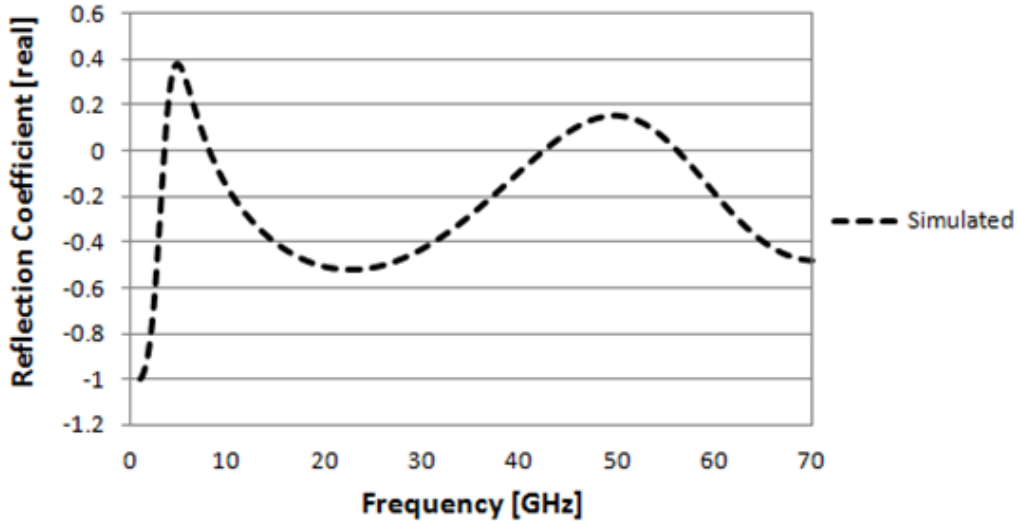

(a)

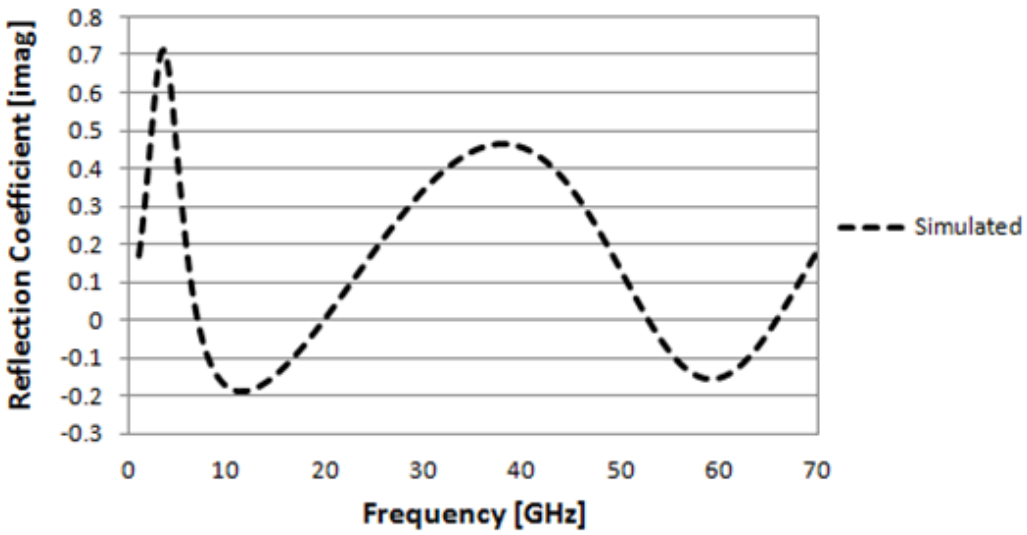

(b)

Figure 5.3 Simulated results of micro-coaxial probe characterizing the Rogers 3006 laminate board at high frequencies. (a) Real Part and (b) Imaginary Part.

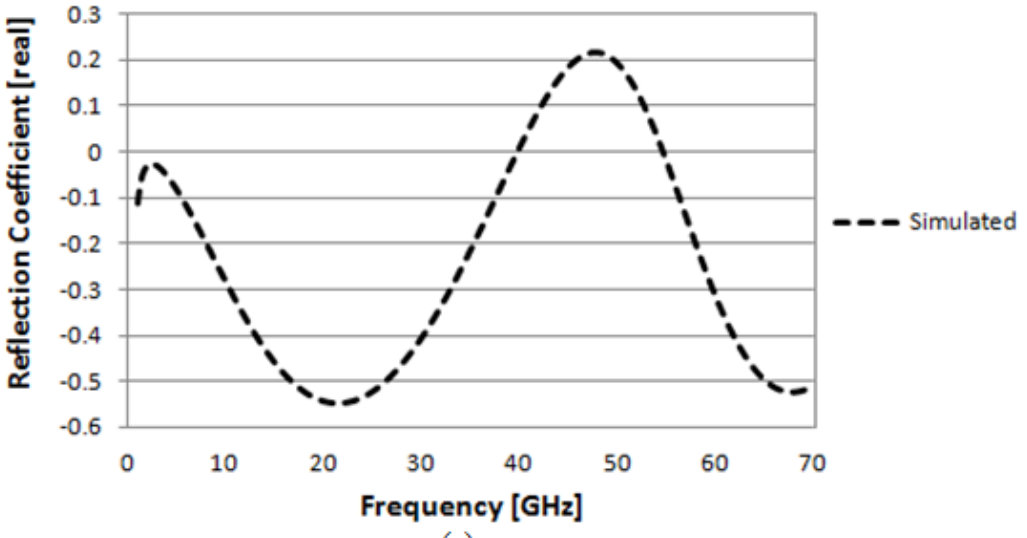

(a)

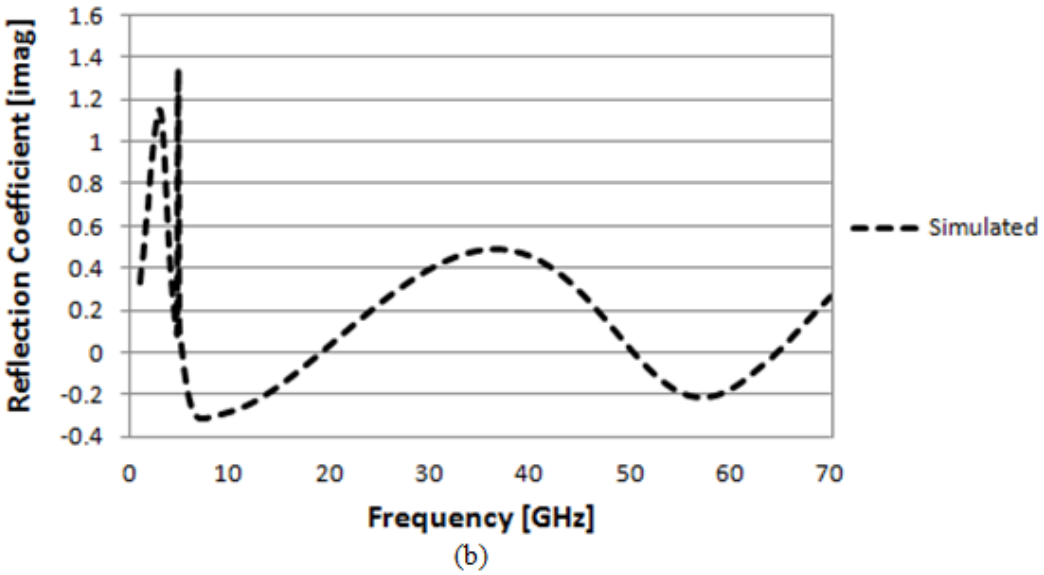

(b)

Figure 5.4 Simulated results of micro-coaxial probe characterizing the Rogers 3010 laminate board at high frequencies. (a) Real Part and (b) Imaginary Part.

During simulation, each known material was placed in contact with the micro-coaxial probe and the reflection coefficient was determined. The results above show the real and imaginary reflection obtained for each material at high frequencies. The results were evaluated over a wide frequency range from dc-to-70 GHz and revealed that at lower frequencies from dc-to-10 GHz, the probe had discrepancies with determining the imaginary part of the reflection of some materials. This was highly due to the fact that the micro-coaxial probe itself behaved like a shorted device at the same frequency range; which disrupted its characterizing abilities at that particular point. These simulated results provided ideal values for the materials real and imaginary parts, and will be used to verify accuracy of the measured results. Furthermore, simulating the reflection coefficients of the known materials allowed the results to be implemented in the cross-ratio variance code as known reflection standards, and the simulated permittivity of the unknown materials (PDMS and Silicon) were then determined.

5.4 Verification of Known Materials Permittivity Value

Prior to deducing the simulated permittivity values of the unknown materials, the permittivity of the chosen 3 known materials needed to be measured to ensure they matched with the data given in the specification sheet. Figure 5.5 illustrates the 3 known materials that were used in the cross-ratio coding technique as calibration standards.

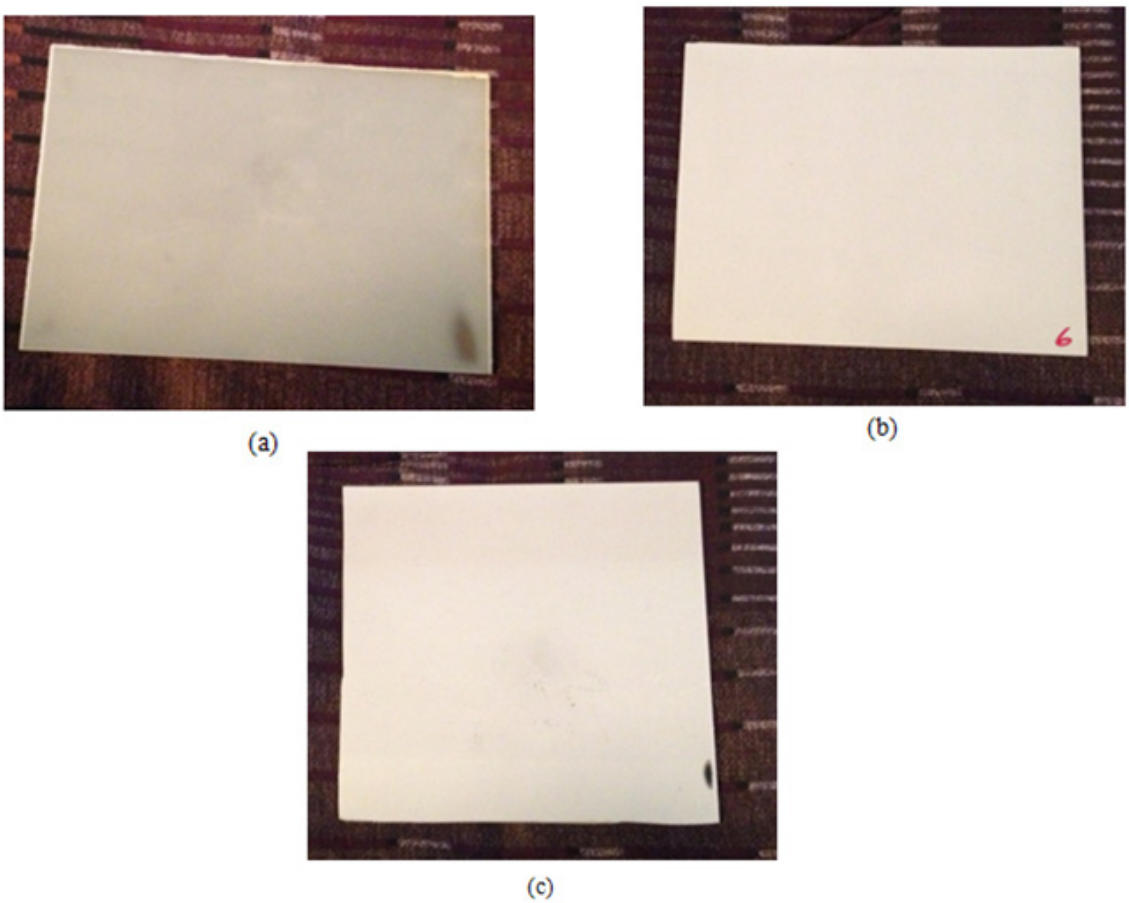

Figure 5.5 Known materials used in the cross-ratio coding technique as calibration standards. (a) Rogers FR-4 Laminate Board, (b) Rogers 3006 Laminate Sheet, and (c) Rogers 3010 Laminate Sheet.

In the data sheet, each material was given a specific permittivity value across a high frequency range under normal operating conditions. These measured values were to be verified, and then included in the coding technique with the simulated reflection coefficients of the same 3

known materials. By including the measured calibration standards and their simulated reflection coefficients in the invariance coding technique, the permittivity of the unknown materials could then be deduced. The materials were measured using a HP 85070B Dielectric Probe Kit. This system was first calibrated using air, an RF short, and diluted water. It is important to note that the probe measuring system only operated up to 14 GHz, therefore the permittivity values could only be verified up to that range of frequency. The measured permittivity results of the 3 known materials are shown in the figures below. The figures include the real and imaginary parts of the materials complex permittivity.

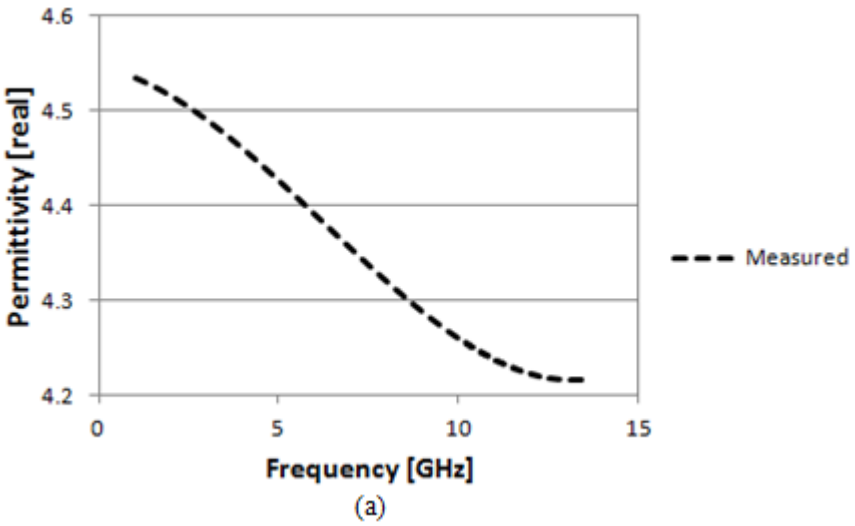

(a)

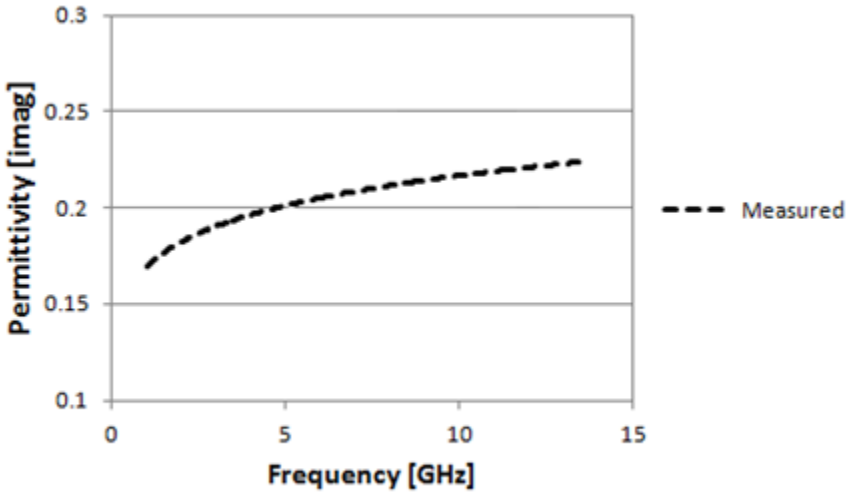

(b)

Figure 5.6 Measured permittivity of Rogers FR-4 Laminate board. (a) Real Part and (b) Imaginary Part.

Figure 5.6 above illustrates the measured complex permittivity of the Rogers FR-4 board up to 14 GHz. Results demonstrated the permittivity starting near 4.5 at ~2GHz and then decreasing to about 4.2 as it approached the 14 GHz limit. These results agreed well with the permittivity provided in [82], which referenced a value of 4.2 up to ~45 GHz. Figure 5.7 (a) and (b) below shows the measured complex permittivity results for the Rogers 3006 high frequency laminate.

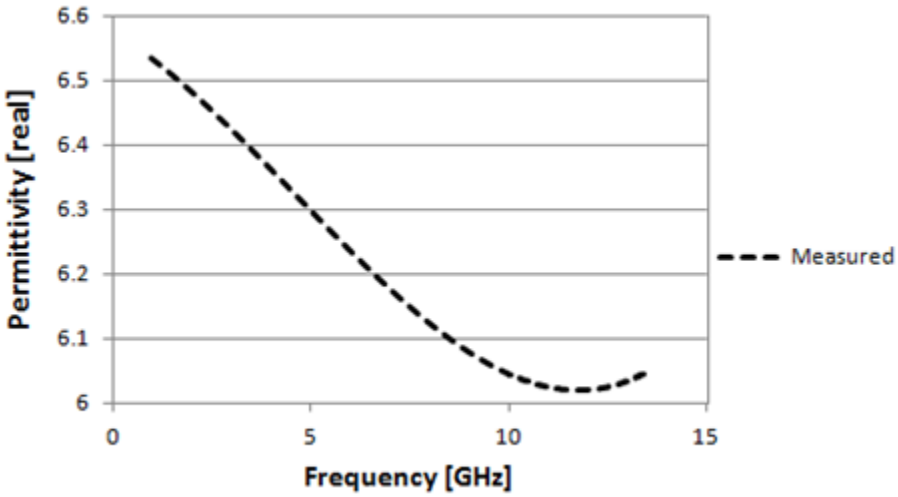

(a)

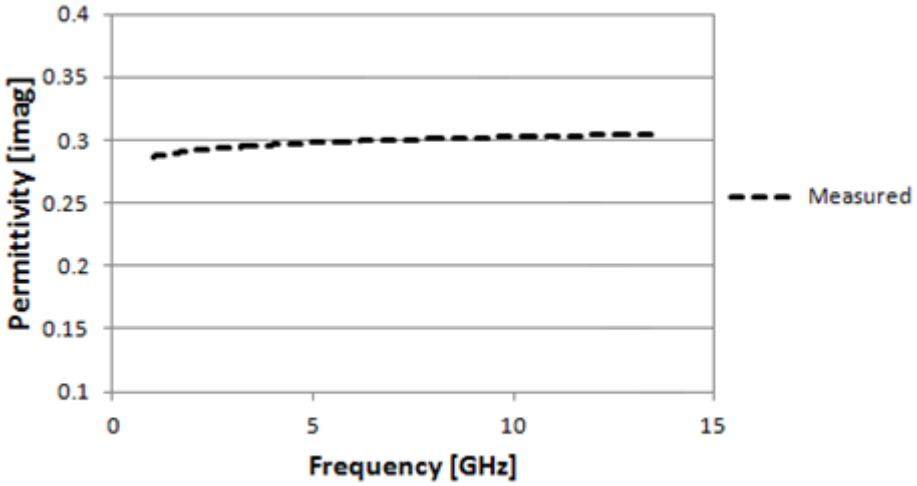

(b)

Figure 5.7 Measured permittivity of Rogers 3006 High Frequency Laminate. (a) Real Part and (b) Imaginary Part.

The figure above illustrates the Rogers 3006 laminate sheet demonstrating a permittivity value near 6.6 at lower frequencies and reaching a constant level between 6 and 6.1 at higher frequencies. These results were a little lower than the referenced value of 6.5 [81], but did measure within a measurement error of +/-5%. The slight alteration in the measured results compared to the permittivity given in the specification sheet could be due to human skin interacting with the reflected materials. This contact between the MUT and the epidermis caused a slight disruption in the probe determining its true permittivity; causing the data to be lower.

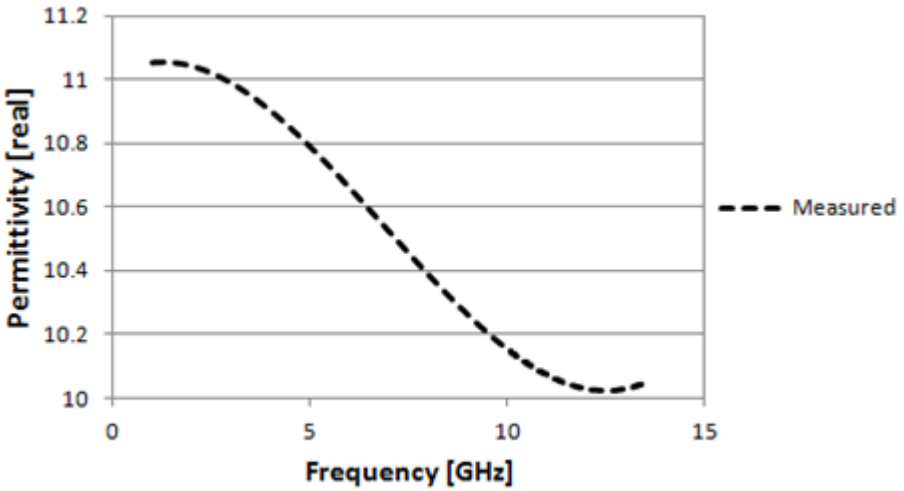

(a)

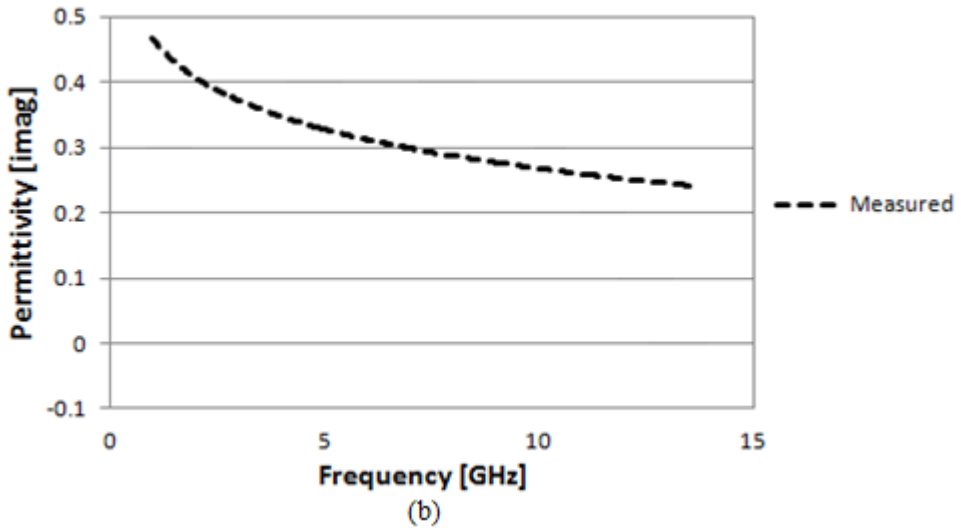

(b)

Figure 5.8 Measured permittivity of Rogers 3010 High Frequency Laminate. (a) Real Part and (b) Imaginary Part.

The figure above demonstrates the measured permittivity for the Rogers 3010 high frequency laminate. The results indicate that the MUT has a permittivity near 11 at lower frequencies and then decreases near 10.1 at higher frequencies. These results were also somewhat lower than the specification sheet which referenced a value of 11.2 at high frequencies [81]. Again, due to the holding mechanism of the MUT when being measured using the probe system, the human skin (epidermis) caused some reflection issues with the material. To prevent this minor error, a metal plate was placed under the MUT to eliminate human contact with the materials. However, this attempt reduced the permittivity values of all materials, making them nearly undetectable. Therefore, the results provided above were used and implemented in the coding technique as the known calibration standards.

5.5 Characterization of Unknown Materials - Simulated Results

Once the permittivity's of the 3 known materials were measured and their reflection coefficients were simulated, the data was then implemented in the invariance coding technique. The measured permittivity values served as 3 calibration standards in the code, and the simulated reflection coefficient values were used as reflection standards in the technique. Using these

values, the permittivity of the unknown materials were evaluated based on simulated reflection coefficient results.

5.5.1 Reflection Coefficient Simulation of Unknown Materials

Using the known simulated reflection values and measured calibration standards, the permittivity of the unknown materials was determined. Before deducing the unknown permittivities using the standards data, the reflection coefficient of each unknown material needed to be simulated when in contact with the micro-coaxial probe as shown in Figure 5.1. The micro-coaxial probe was placed in contact with the MUT and its reflection coefficient was evaluated from dc-to-70 GHz. The unknown MUT's were also simulated with the same thickness of 1.3mm as the known materials. Again, this value was chosen because it was suggested that the MUT be at least twice the length of the probe; which in this case was 300 μm. Following the simulation, the reflection data of the unknown material was implemented in the code as the permittivity to be found. The figure below illustrates the simulated reflection coefficient results for the unknown material PDMS.

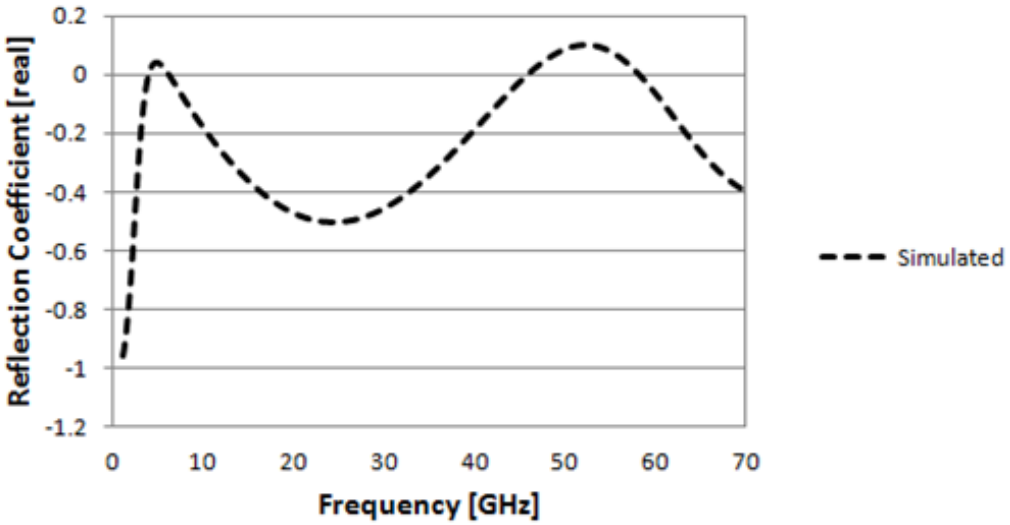

(a)

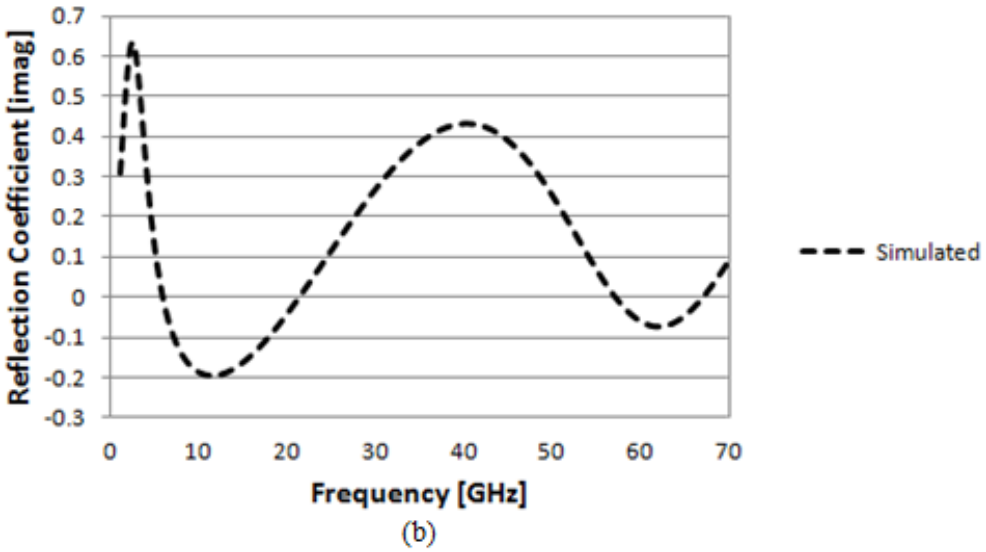

(b)

Figure 5.9 Simulated reflection coefficients of PDMS. (a) Real Part and (b) Imaginary Part.

The results above show the simulated results for the reflection coefficients of the unknown material PDMS. The real and imaginary parts of the data are shown over a wide frequency range up to 70 GHz. These results served as a reference for the unknown material prior to actually measuring its reflection coefficient. By simulating the reflection coefficient of PDMS, expected results were obtained and utilized in the permittivity calculations. The same simulation was performed on the unknown material Silicon over a wide frequency range from dc-to-70 GHz, and its reflection coefficient was determined. Figure 5.10 below shows the simulated reflection coefficient results for Silicon at high frequencies. Again, reflection coefficient values greater than 1 obtained following simulation were contributed to the several errors mentioned in previous sections.

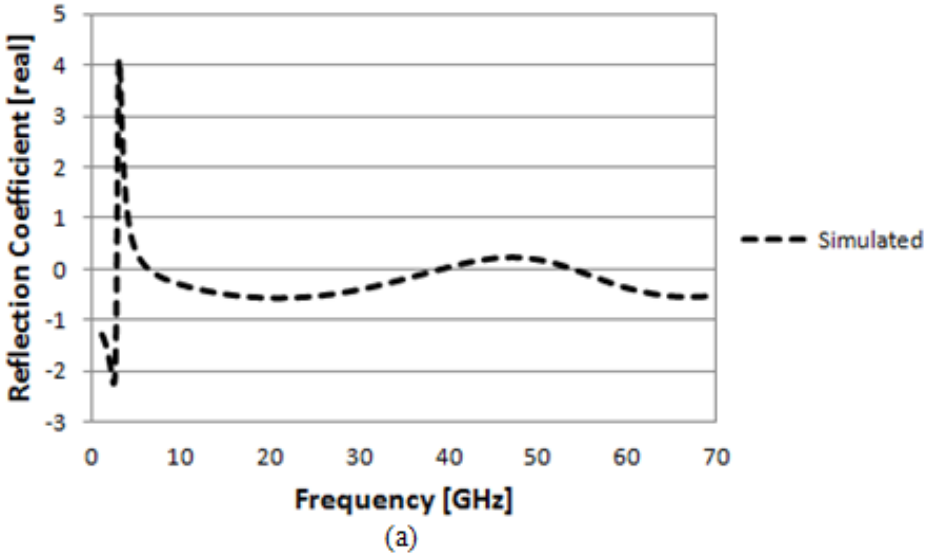

(a)

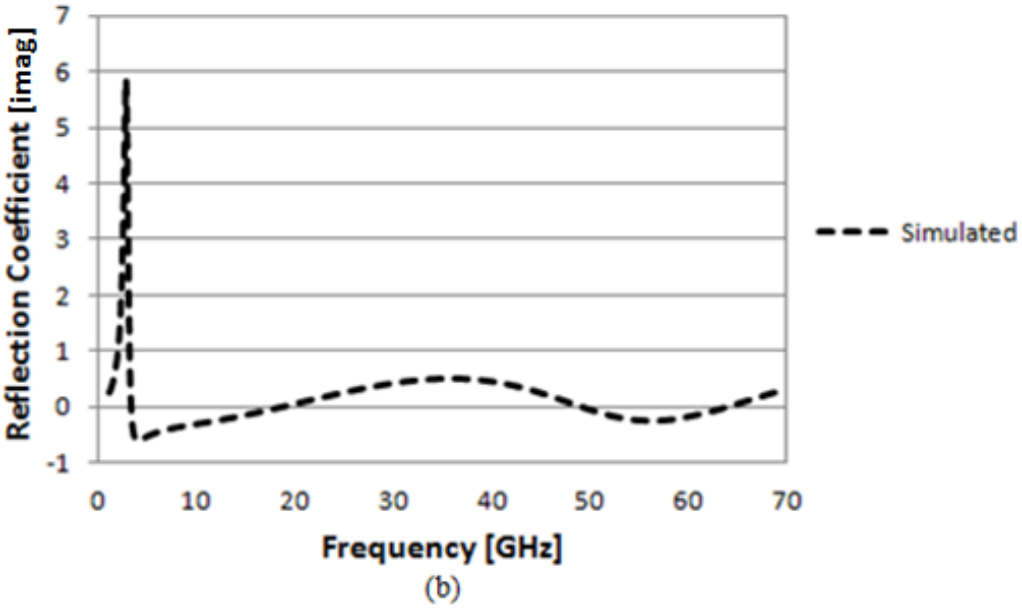

(b)

Figure 5.10 Simulated reflection coefficients of Silicon. (a) Real Part and (b) Imaginary Part.

The results above show the simulated reflection results of the unknown material Silicon, evaluated over a broad frequency range. It is important to note again that the simulated reflection values at low frequencies were non-physical possibly due to the material properties of Silicon in the software and/or results of the mesh convergence. Results demonstrate that from dc-to-10 GHz, the coaxial probe had trouble determining the reflection coefficient of Silicon which caused

inconsistencies in the data. This is again mainly due to the probe behaving as a shorted device at lower frequencies, which altered the reflectance results when characterizing the unknown material. However, the data started to level off and behave much better beyond the 10 GHz mark and at higher frequencies. This is true because at higher frequencies, the micro-coaxial probe itself achieved its best performance, which allowed the materials reflection to be easily determined.

5.5.2 Permittivity of Unknown Materials Using Simulated Reflection Coefficients

After the simulated reflection coefficients of the unknown materials were obtained, they were then inputted in the cross-ratio invariance coding technique to deduce its permittivity. This was done by using the measured permittivity values of the 3 known materials as measured calibration standards. By measuring the exact permittivities of these materials, it assisted in improving the accuracy of the results. Next, the simulated reflection coefficients of the 3 known materials were placed in the coding technique and served as simulated calibration standards closely related to the unknown materials. As mentioned earlier, the known materials were chosen in advanced due to their use in high frequency applications up to 77 GHz. Lastly, the simulated complex permittivity of the Silicon and PDMS was determined using the 3 known standards. This permittivity was not the actual value of the unknown materials, but served as a great base value for what was expected from the invariance coding technique that was used. Following obtaining the simulated permittivity values, it was then easier to determine the range of error when compared to the real permittivity. The figure below shows the deduced complex permittivity of PDMS when using the simulated reflection coefficient results and the measured calibration standards in the coding technique.

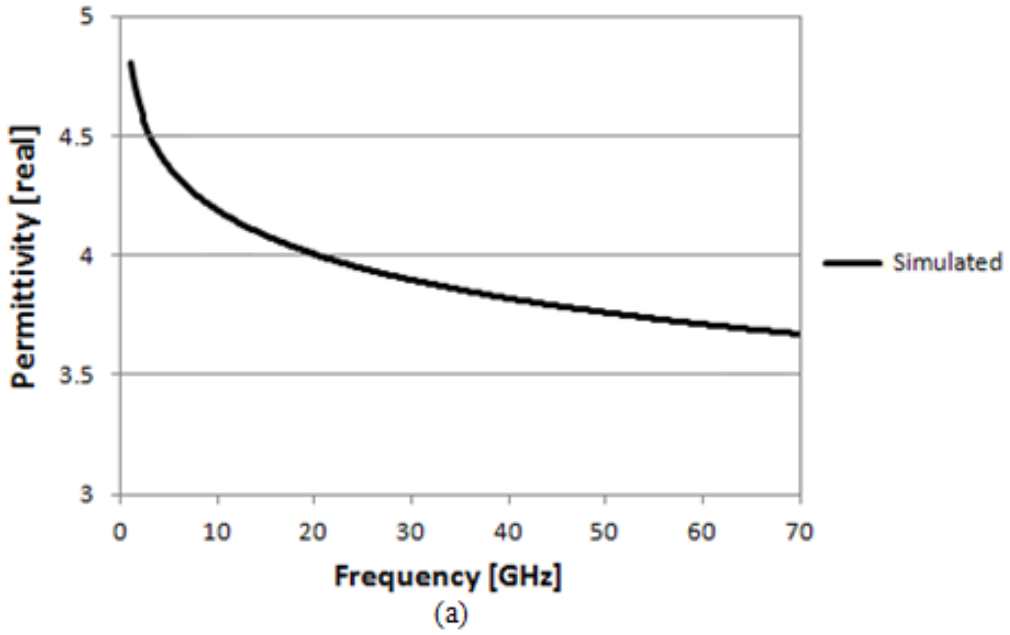

(a)

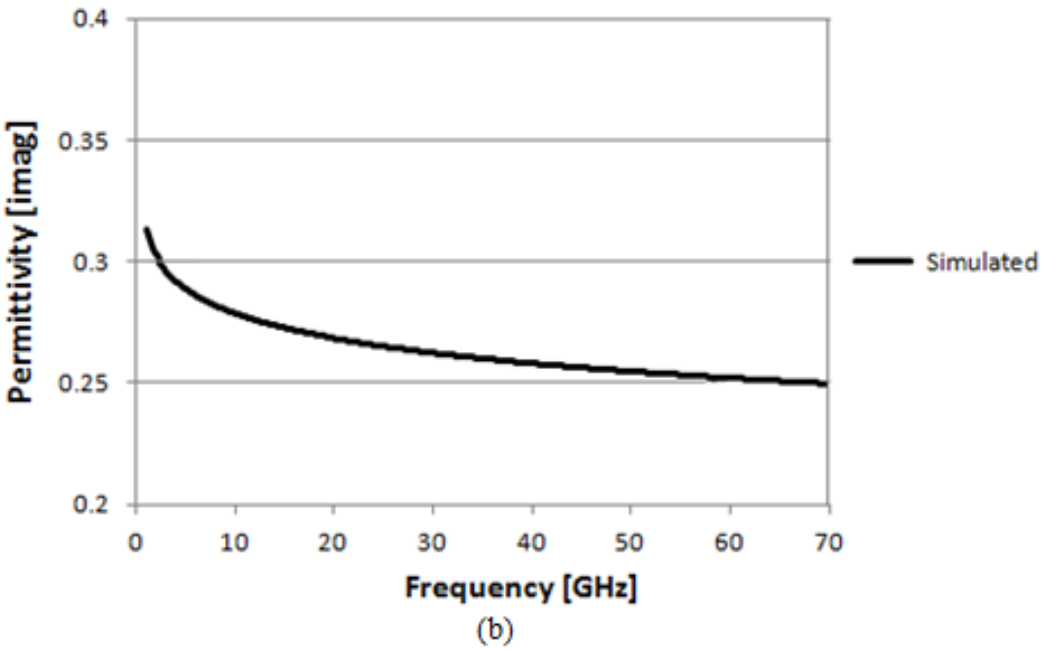

(b)

Figure 5.11 Simulated complex permittivity of PDMS using cross-ratio invariance coding technique. (a) Real Part and (b) Imaginary Part.

The figure above shows the complex permittivity results for PDMS when using the simulated reflection coefficient results in the cross-ratio invariance coding technique. In Figure 5.11 (a), it can be seen that the permittivity begins at a value of ~4.8 at dc and begins to decrease to 4.3 near 10 GHz. Once it approached higher frequencies, it continued to decrease to 3.9 at 30 GHz and then to 3.7 at 40 GHz. This patterned continued through the entire range of frequency up to 70 GHz and achieved a final value of **3.6**. The imaginary part of the permittivity is shown in Figure 5.11 (b) and it demonstrated a permittivity of 0.31 at dc and decreased to 0.27 at 10 GHz. As it approached higher frequencies, it decreased near 0.26 at 30 GHz, and then eventually leveled to **0.26** and **0.25** from 40 GHz-to-70 GHz.

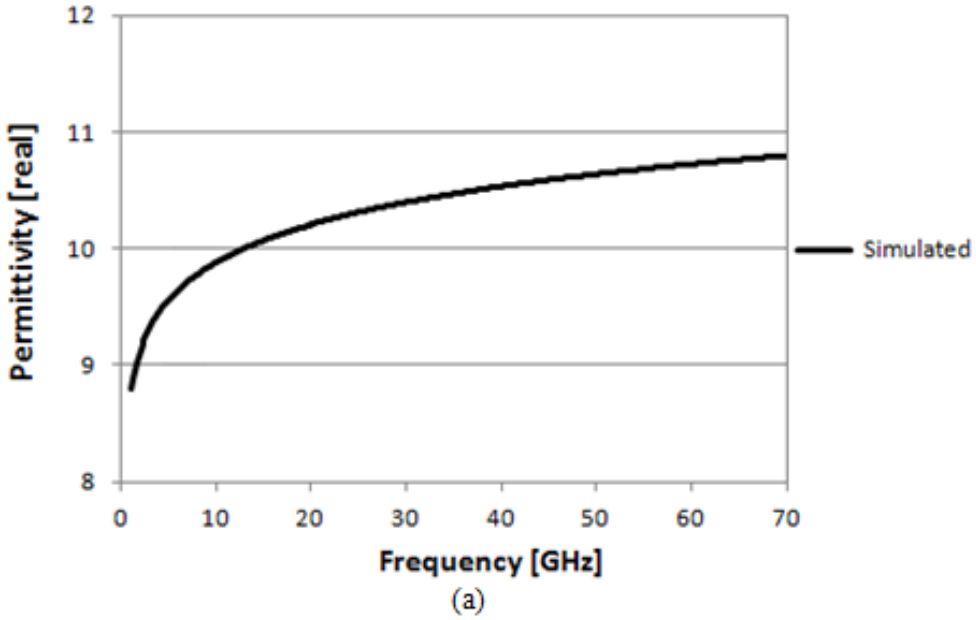

(a)

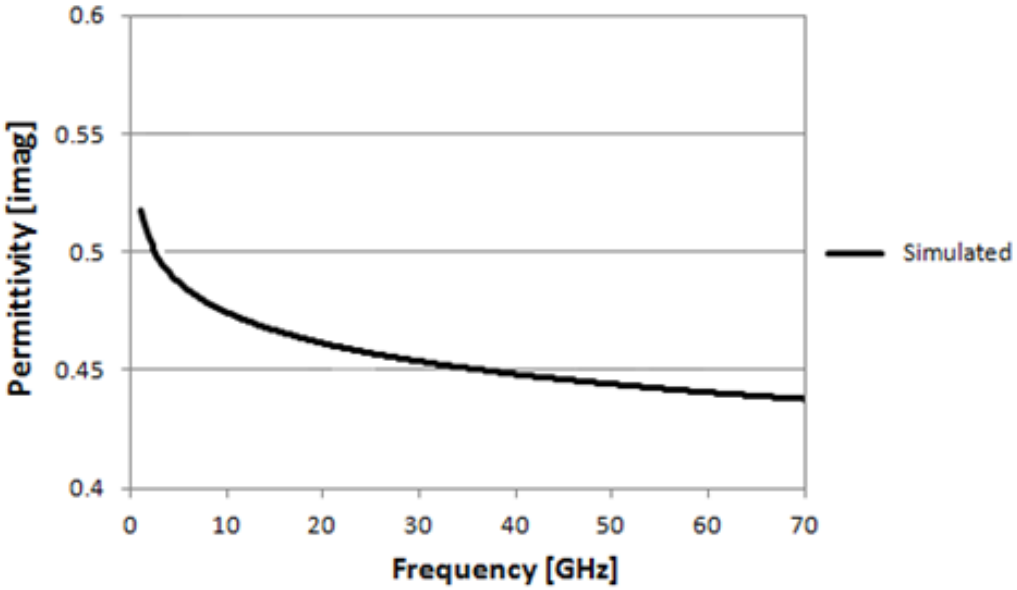

(b)

Figure 5.12 Simulated complex permittivity of Silicon using cross-ratio invariance coding technique. (a) Real Part and (b) Imaginary Part.

In Figures 5.12 (a) and (b) above, the complex permittivity results for Silicon are shown when using the simulated reflection coefficient results in the cross-ratio invariance coding technique. The results indicated that the permittivity (real part) initially had a value between 9 and 10 from dc-to-10 GHz. The permittivity then increased as the higher frequency levels were reached; demonstrating a value of 10.2-10.7 from 20 GHz-to-50 GHz. After the 50 GHz range, the permittivity appeared to demonstrate a constant value of ~**10.8** up to 70 GHz. Although the results only cover up to 70 GHz, it can be seen that the permittivity will eventually reach a constant value of 11 up to nearly 100 GHz. The results in Figure 5.12 (b) show the imaginary part of the permittivity, and it can be seen that it reached a value of 0.53 at dc and eventually decreased to 0.47 at 10 GHz. The data also shows that as it surpasses the 10 GHz mark, it reduces to a value of 0.45 at 30 GHz, 0.39 at 50 GHz, and levels off to 0.38 at 70 GHz. These values seemed steady after the 30 GHz level and proved that a more constant curve can be expected as the frequency level of characterization increases.

5.6 Characterization of Unknown Materials - Measured Results

In the previous section, the permittivity of the unknown materials PDMS and Silicon were determined using the simulated reflection coefficients of the 3 known materials and their measured calibration standards; along with the simulated reflection coefficients of the unknown materials. However, in this section, the permittivity of the unknown materials was determined by actually measuring the reflection coefficients of the 3 known materials and of the unknown materials (Silicon and PDMS). The measured calibration standards of the 3 known materials that were used in the previous section were also used in determining the permittivity of the unknown materials in this section. The difference in the coding technique when determining the permittivity of PDMS and Silicon in this section is that all reflection coefficient data implemented in the code was measured instead of simulated. It is important to note that the reflection coefficients of the known and unknown materials needed to be measured in order to deduce its permittivity over the desired range of frequency.

5.6.1 Material Characterization Setup

Similar to the measurement setup shown in Chapter 4, the high frequency material characterization was performed using the layout illustrated in Figure 5.13. The fabricated micro-coaxial probe was first placed on the Microtech probe station that contained 2 ports; however, only port 1 was necessary for the reflection measurements. Port 1 on the probe station was then connected to the ground-signal-ground CPW pitch probes using the high frequency V-band cable. Next, the V-band cable, capable of measuring up to 67 GHz, was connected from the CPW pitch probes to port 1 of the VNA. Then, a calibration was performed on the probe-to-cable connection using a CS-5 calibration kit to eliminate any parasitic effects that may affect the measurement results. Finally, the MUT was placed on the chuck of the probe station, and the micro-coaxial

probe was placed directly on top; making complete contact for high frequency material characterization. The reflection coefficients of each material (known and unknown) were then determined.

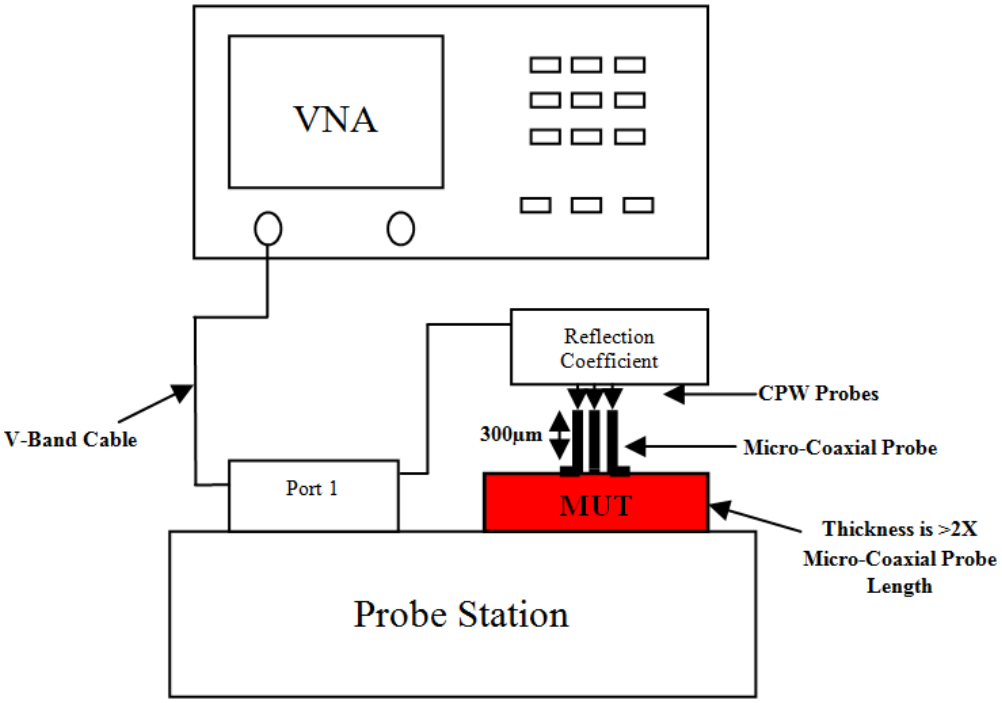

Figure 5.13 Illustration of Test Setup used for High Frequency Material Characterization.

5.6.2 Measured Reflection Coefficients of Known Materials

The reflection coefficients of the 3 known materials were first measured using the setup shown above. Each material was characterized over a wide frequency range from dc-to-70 GHz. It is important to note however, that the VNA only reached 65 GHz; therefore, the data shown beyond 60 GHz are expected results. The measured reflection coefficient results for Rogers FR-4 laminate board are shown in the figure below. The reflection coefficient of the Rogers board was also measured using the standard 150µm pitch probes to validate the accuracy of micro-coaxial probes and is also shown in the figure below.

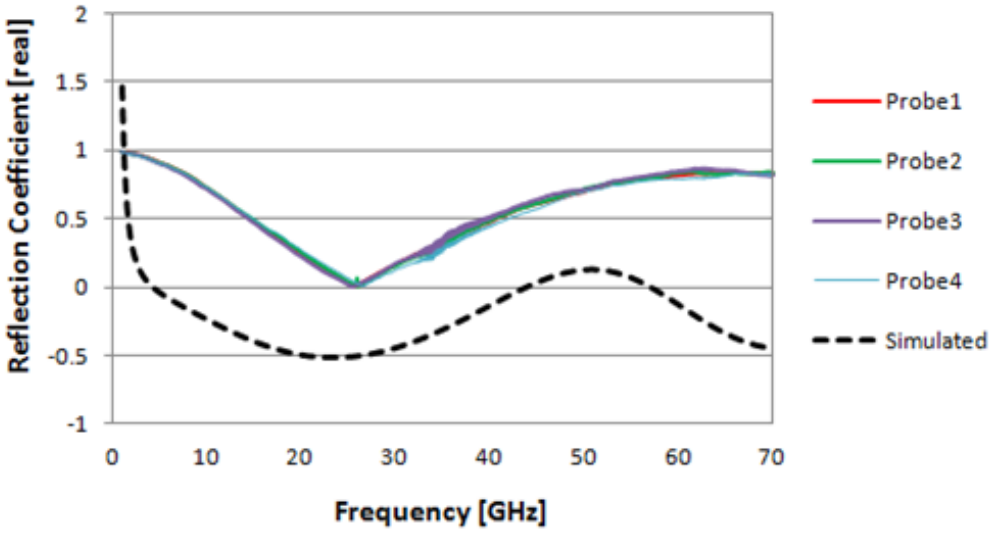
Reflection Coefficient [real]
2
1.5
1
0.5
0
-0.5
-1
0
10
20
30
40
50
60
70
Frequency [GHz]
Probe1
Probe2
Probe3
Probe4
Simulated

(a)

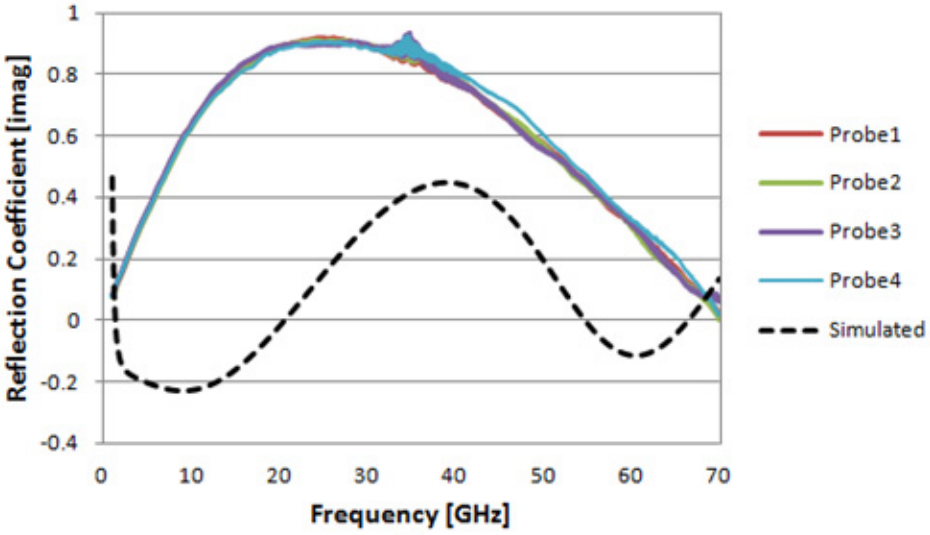
Reflection Coefficient [imag]
1
0.8
0.6
0.4
0.2
0
-0.2
-0.4
0
10
20
30
40
50
60
70
Frequency [GHz]
Probe1
Probe2
Probe3
Probe4
Simulated

(b)

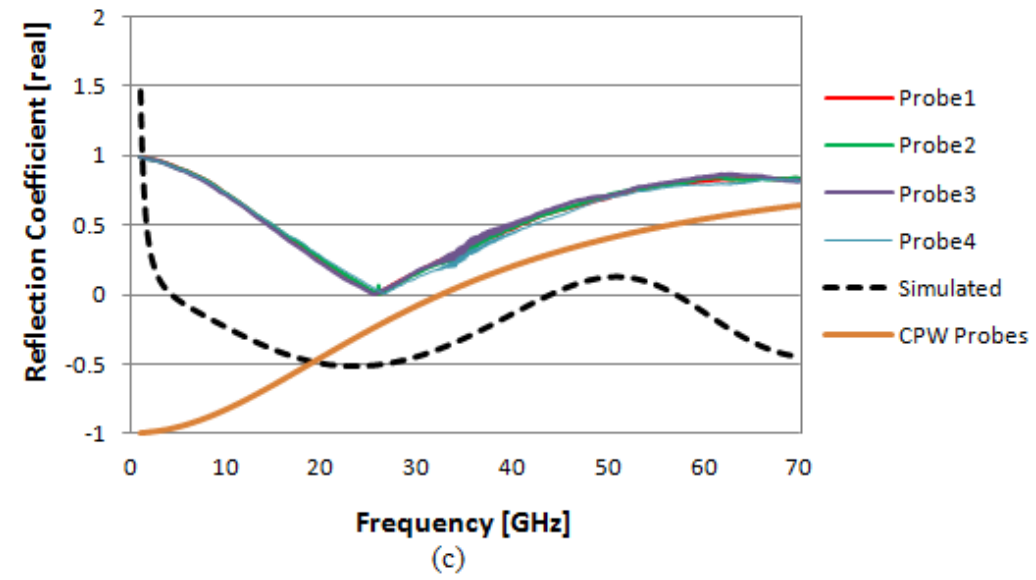

(c)

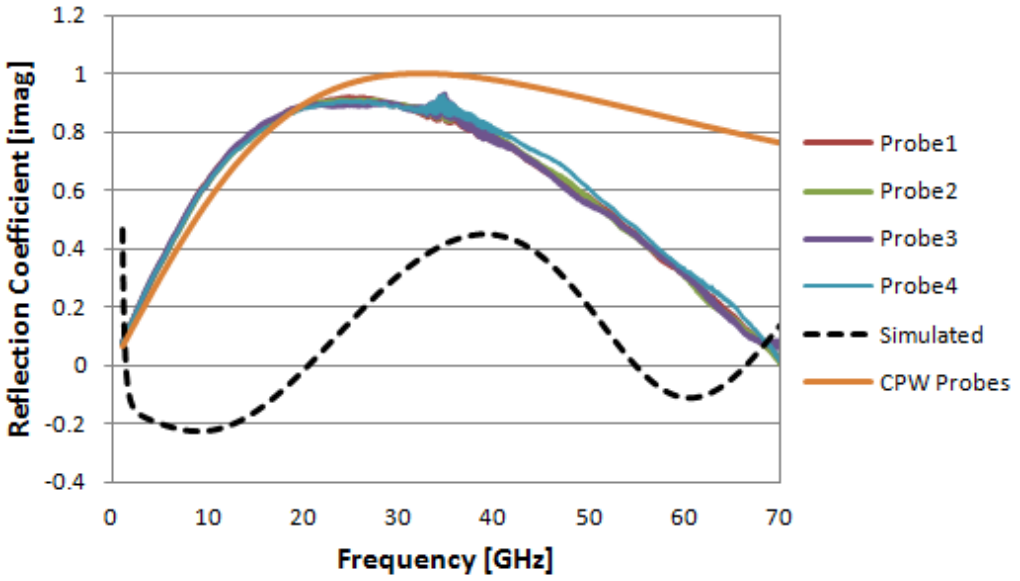

(d)

Figure 5.14 Measured reflection coefficients of Rogers FR-4 laminate board. (a) Real Part, (b) Imaginary Part, (c) Real Part with CPW probes, and (d) Imaginary Part with CPW probes.

The figure above illustrates the measured reflection coefficients for the FR-4 board compared to the simulated results. In both the measured and simulated results, the MUT was placed directly in contact with the micro-coaxial probe. During testing, four probes were measured to characterize the MUT at high frequencies. In Figure 5.14 (a), it can be seen that reflection values ranged between 1 and 0.1 from dc-to-25 GHz for all four probes. The results

continued between these values over the entire range of frequency. The results for the imaginary part demonstrated values between 0.1 and 0.9 from dc-to-20 GHz, and then decreases to ~0.1 while approaching the 70 GHz mark. These results however, differ from the simulated results by a factor of 0.5 for the real, and 0.6 for the imaginary part. This indication was mainly due to the simulation errors that occurred at low frequencies which eventually matriculated across the entire band impacting results at higher frequencies. The fact that the material was resting on the metal chuck could have also played a factor in the achieved results. Although the measured data was a bit off when compared to the simulated results, this material was only a measured standard used to in the code as a calibration standard; which means it slightly altered the final deduced permittivity of the unknown materials. The results in Figures 5.14 (c) and (d) show the measured results using the micro-coaxial probes compared to those when using the CPW probes. The comparison indicates a large difference at low and high frequencies for the real and imaginary parts, verifying that when the CPW probes were used the reflection data was not as accurate as the micro-coaxial probe results. This difference in reflection data could lead to an incorrect permittivity determination due to the lack of accuracy in the calibration standard data. Therefore, the micro-coaxial probe measurement would provide the highest level of accuracy for deducing the unknown permittivities. Figure 5.15 shows the real and imaginary measured reflection coefficients for Rogers 3006 High Frequency Laminates.

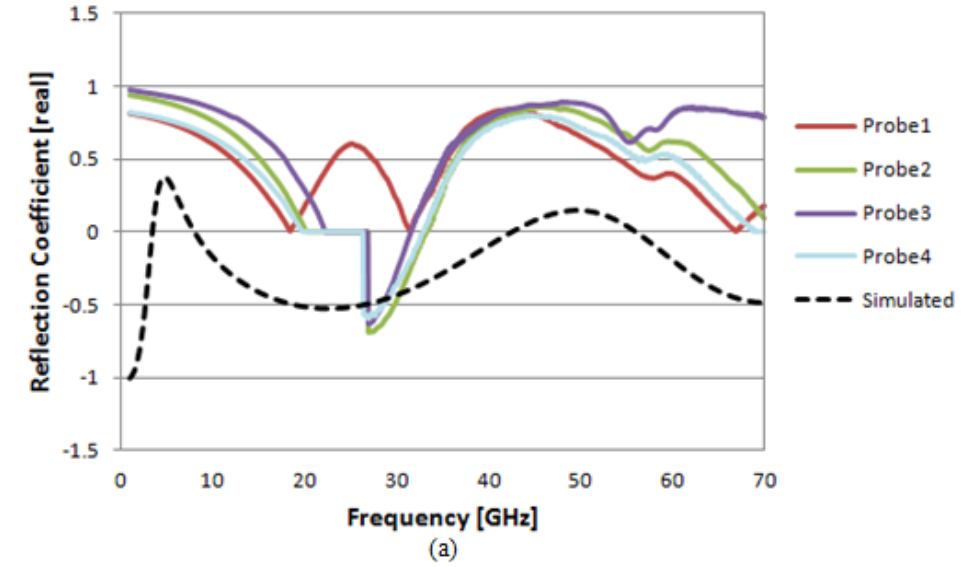

(a)

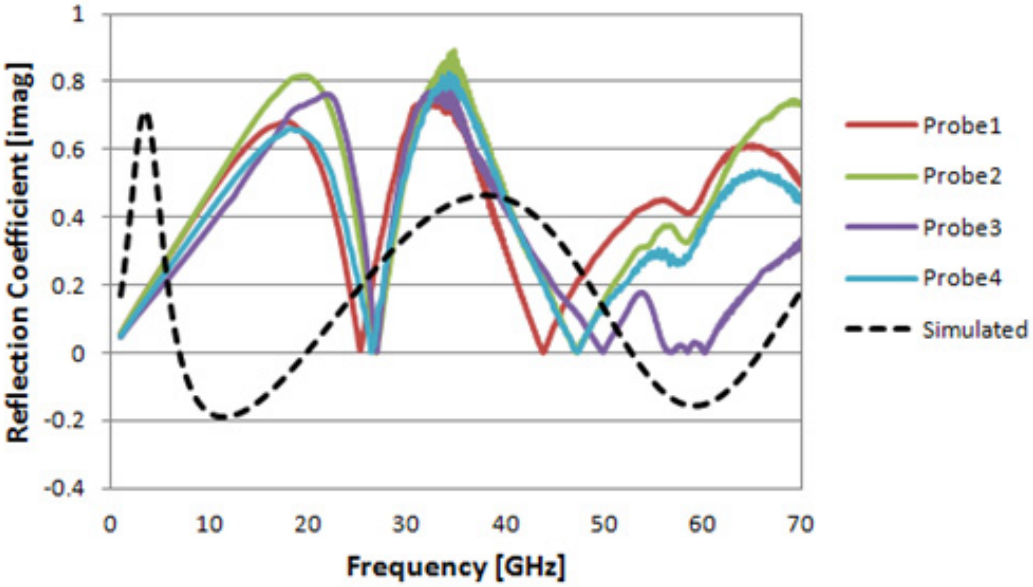

(b)

Figure 5.15 Measured reflection coefficient of Rogers 3006 High Frequency Laminate Sheet. (a) Real Part and (b) Imaginary Part.

The figure above illustrates the results obtained when measuring the reflection coefficient of the Rogers 3006 high frequency laminate sheet using 4 micro-coaxial probes. The results show that the real part behaved very similar for all probes, demonstrating a resonance of -0.5 near 30 GHz. The rest of the frequency band showed the measured results differing from the simulated by

a factor of nearly 0.6 and seeming to level off as it approached the 70 GHz range. For the imaginary part, the data nearly achieved very similar results crossing paths near a value of 0.2 at the 30 GHz and 50 GHz mark. The rest of the frequency band however, demonstrated a difference factor of about 0.4 between the measured and simulated results. The difference in the real and imaginary part is due to the capacitance between the material and micro-coaxial probe, and the metal chuck altering the reflection value of the material itself. Again, this material was used as a calibration standard in the coding technique and affected the results of the deduced permittivity of the unknown materials. The last known material was measured and the reflection coefficient data is provided in Figures 5.16 (a) and (b).

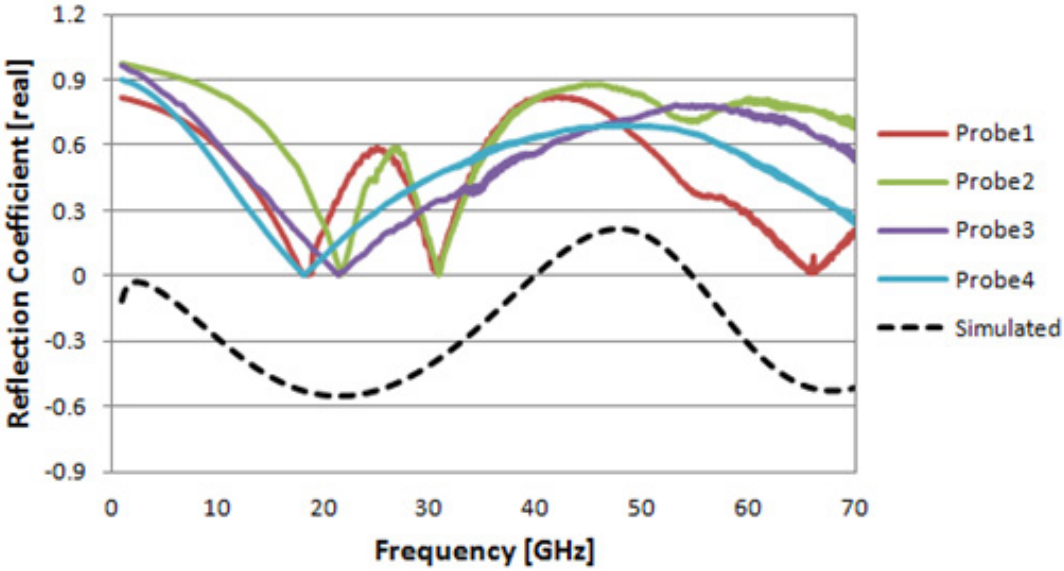

(a)

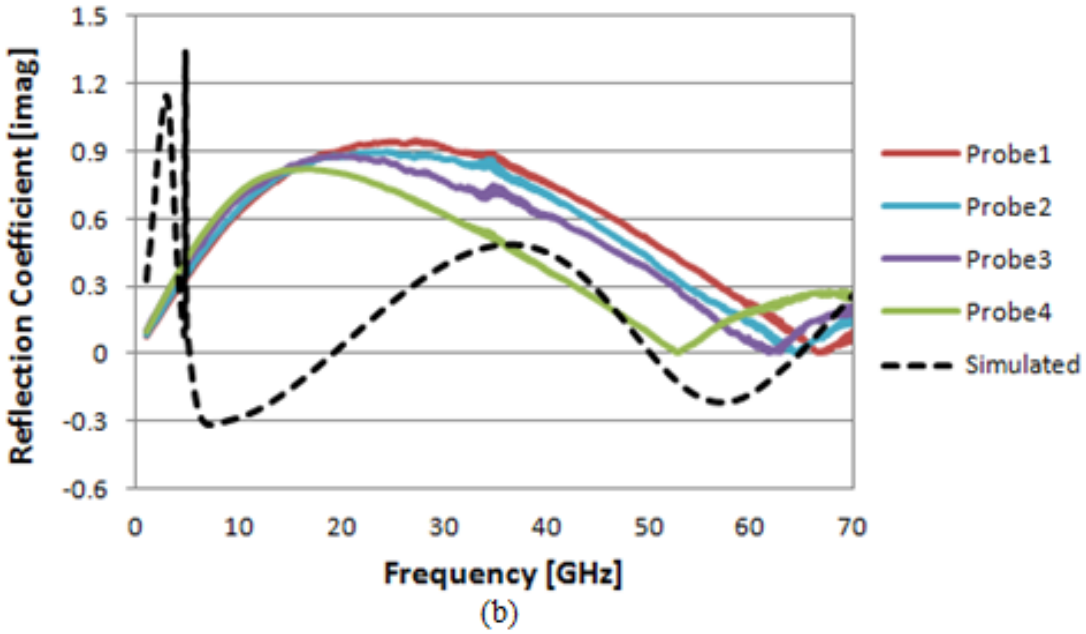

(b)

Figure 5.16 Measured reflection coefficient of Rogers 3010 High Frequency Laminate Sheet. (a) Real Part and (b) Imaginary Part.

The results for the measured reflection coefficient of the Rogers 3010 laminate sheet are shown in the figure above. The real part measurement demonstrated a few resonance values at 10, 20 and 30 GHz. This material also showed the largest difference between measured and simulated data with a variance by a factor of nearly 0.9 for the real part, and 0.8 for the imaginary. The imaginary part however, begin to show similarities as it approached higher frequencies, and the real part decreased to a difference factor of ~0.2. The variance between measured and simulated data can be contributed to material reflectance, behavior of the probe, and surface waves that played a factor from resting on the metal chuck. This material was also used as a calibration standard, and therefore affected the deduced permittivity results of the unknown materials. As mentioned before, the measured reflection coefficient comparisons to simulated were a bit off, but this was due to the simulation error occurring at lower frequencies. Further discussion on the difference in the reflection coefficient data of the known materials is provided in section 5.7.

Following the reflection coefficient measurements of the known materials, each data set was then implemented in the invariance coding technique where it replaced the simulated reflection coefficient values. Although four probes were used to measure each material, the probe data with the best performance on each material was used in the code.

5.6.3 Measured Reflection Coefficients of Unknown Materials

Along with the measured reflection coefficients presented above, the unknown materials reflection coefficients were also measured using the same characterization setup. This was necessary because the 3 known materials reflection data served as the calibration standards to the invariance coding system, but the unknown materials reflection data also needed to be measured in order to deduce their permittivity. The figure below shows the measured reflection coefficient data (real and imaginary) for PDMS.

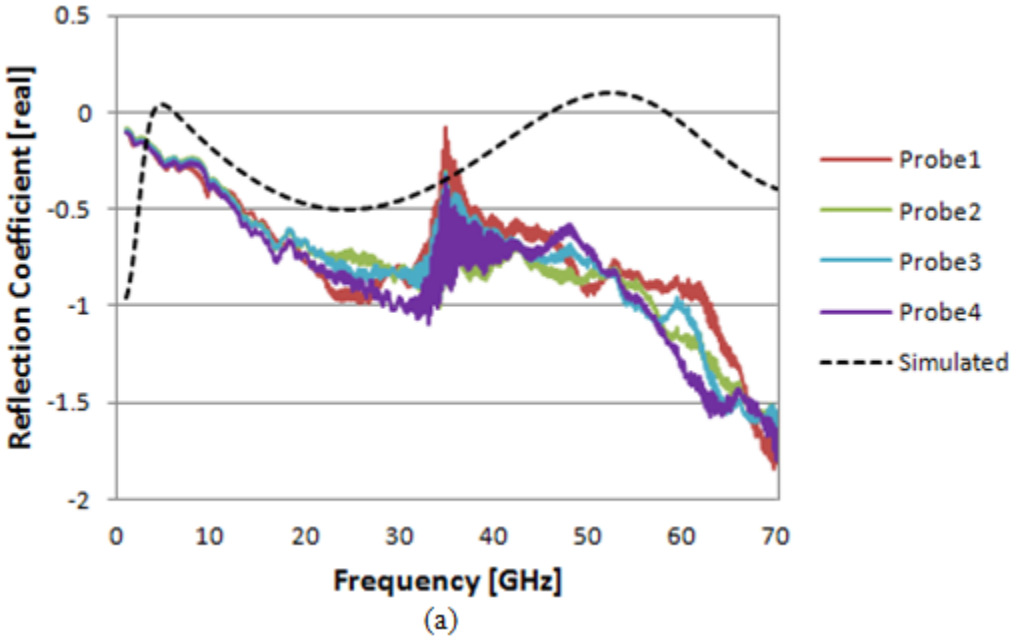

(a)

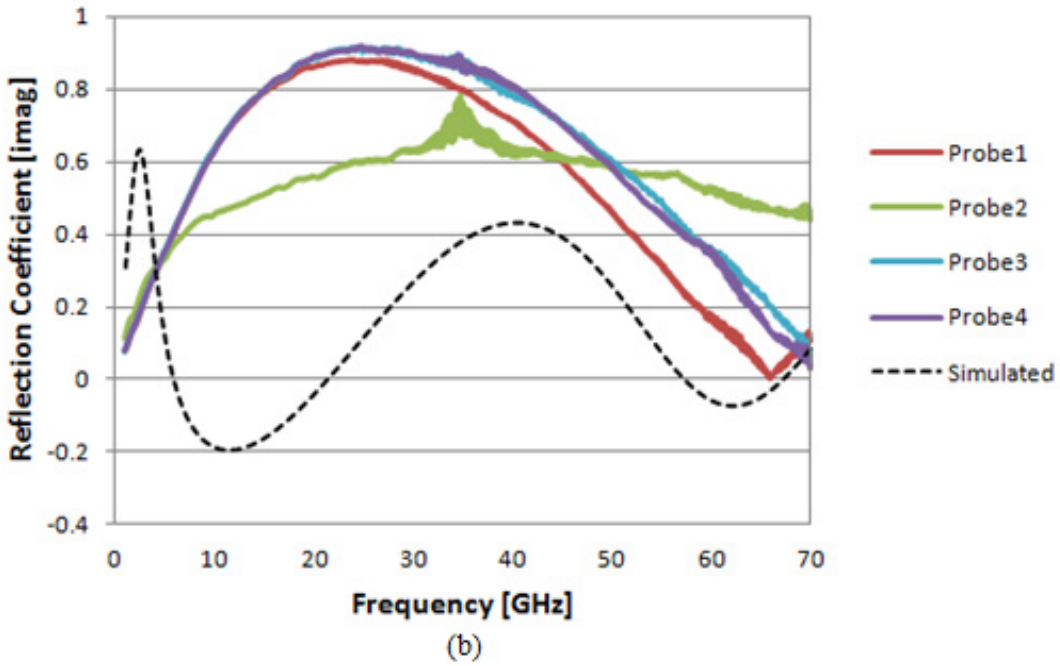

(b)

Figure 5.17 Measured reflection coefficient of Unknown material PDMS. (a) Real Part and (b) Imaginary Part.

In the figure above, the measured reflection coefficient data for PDMS is shown compared to the simulated results. The figure illustrates the real part of the reflection data slightly differing from the simulated data by a factor of ~ 0.5 at lower frequencies, and 0.8 as it approached higher frequencies. Four probes were again used to characterize the material and provided a reflection value of -0.2 to -0.9 from dc-to-30 GHz. As the curve approached higher frequencies, the reflection coefficient again increased to about -0.7 up to 50 GHz and leveled off near -1.5 while approaching the 70 GHz mark. In the imaginary data, the reflection data crosses at lower frequencies demonstrating very similar results. At higher frequencies, a difference factor of ~0.5 can be seen between the measured and simulated data from 30-to-45 GHz. As it continued across the frequency spectrum, the data begin to closely resemble the behavior of the simulated values with a difference factor of only 0.3. The above results did not exactly resemble the simulated values, but the data will still be used and implemented in the coding technique; therefore, the slight difference in reflection values was addressed when the permittivity of the

unknowns were determined. Figures 5.18 (a) and (b) illustrates the real and imaginary measured reflection coefficient results for Silicon. In Figures 5.18 (c) and (d), the measurement sensitivity of a single probe (Probe 2) was investigated by showing the difference in results after the micro-coaxial probe was placed in contact with Silicon multiple times simultaneously. This probe was chosen because it was in the best condition to be measured following the fabrication process.

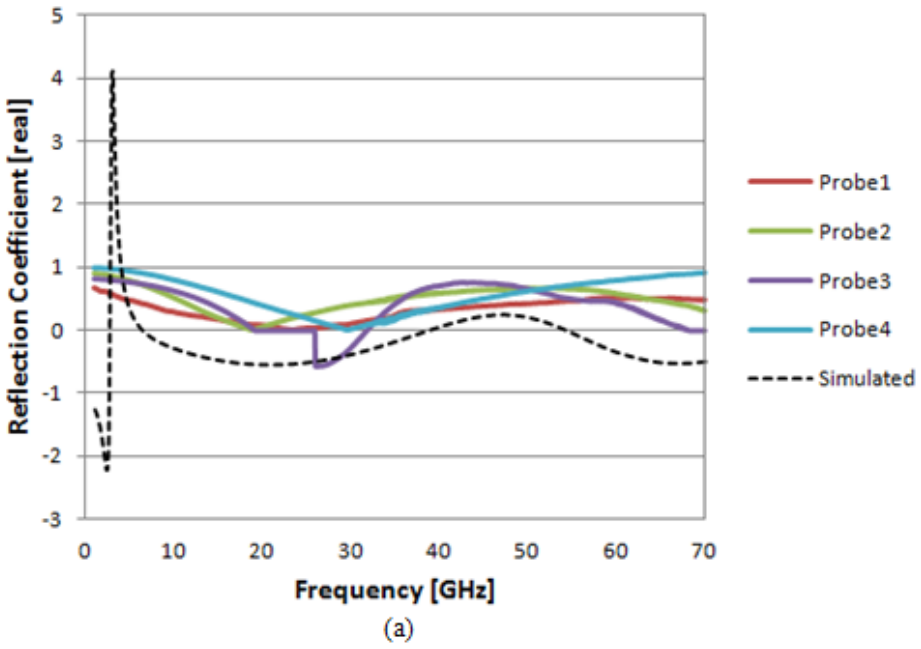

(a)

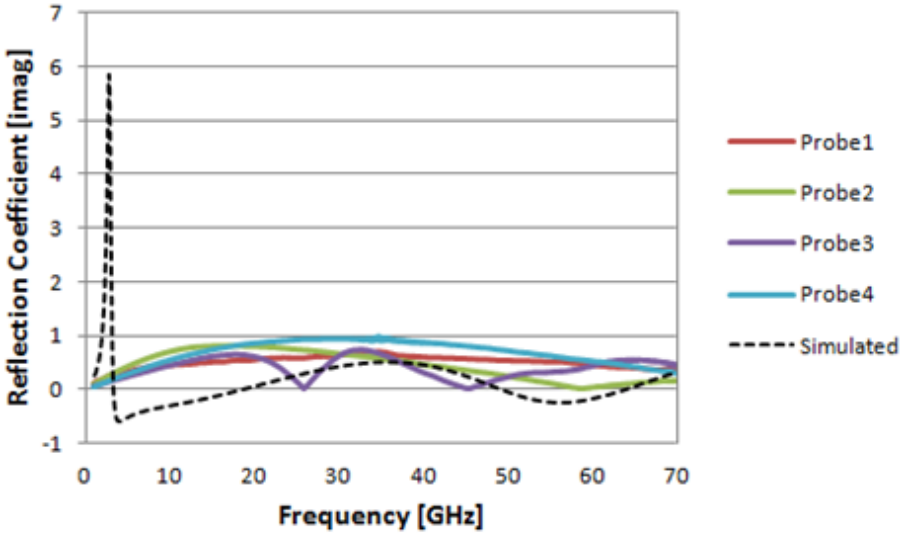

(b)

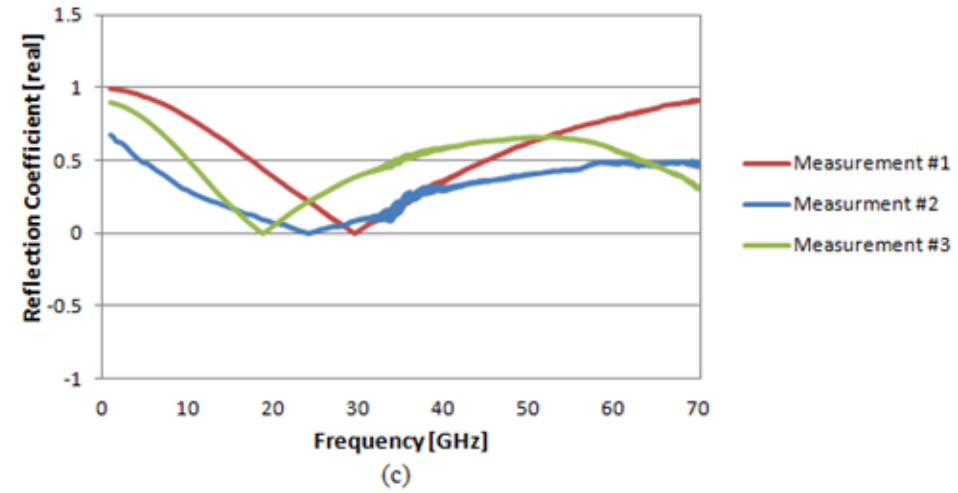

(c)

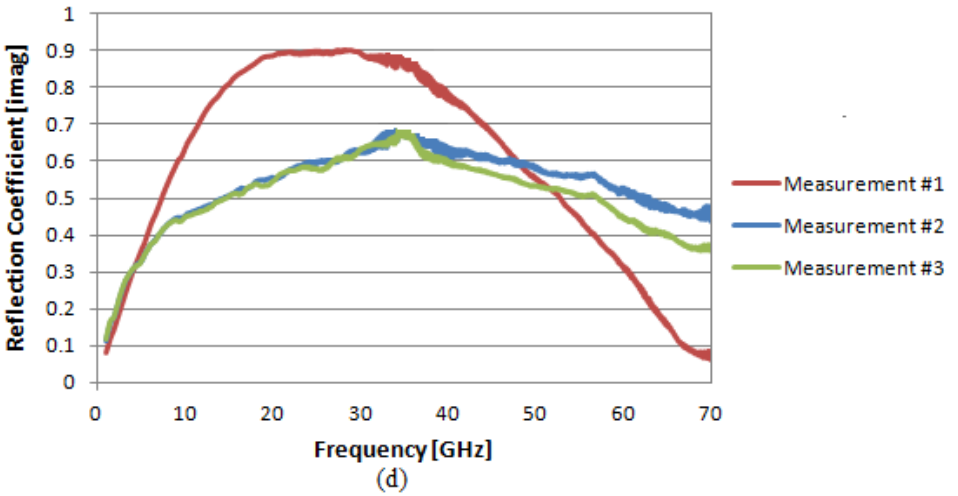

(d)

Figure 5.18 Measured reflection coefficient of Unknown material Silicon. (a) Real Part and (b) Imaginary Part and Measurement Sensitivity of (c) Real Part and (d) Imaginary Part.

The results above show the measured reflection coefficient results for Silicon. Again, four probes were used to characterize the behavior of the material at high frequencies. The real part results demonstrated a reflection value of 0.2 to 0.8 from dc-to-25 GHz. This value then leveled of between 0.5 and 0.7 from 40 GHz-to-70 GHz. This revealed a difference factor from the simulated results of ~0.4-0.6 over the wide frequency range. For the imaginary part, the measured data demonstrated a value of 0-0.8 from dc-to-45 GHz; this value then decreased to ~0.3 and 0.4 as it approached the 50-to-70 GHz range. These imaginary results revealed a difference factor of about 0.8 at lower frequencies but then decreased to ~ 0.2 from 50-to-70

GHz; while nearly crossing paths with the same value from 30-to-40 GHz. It is also important to note that the major difference between measured and simulated data from dc-to-8 GHz was again mainly due to the micro-coaxial probe's device error during simulations at lower frequencies. Results in Figures 5.18 (c) and (d) indicate that following multiple measurements, for the real part, the largest difference factor was ~0.2; and as large as ~0.25 for the imaginary part. These results proved that the measured results varied after multiple attempts but not in significant value that would impact the deduced permittivity results.

After both the reflection coefficients of the known and unknown materials were measured, they were implemented as calibration standards in the cross-ratio coding technique where the unknown permittivity's were then determined.

5.7 Permittivity of Unknown Materials Using Measured Reflection Coefficients

Following the measuring of the known and unknown materials reflection coefficients, the data was then used in the cross-ratio invariance coding technique to determine the permittivity of the unknown materials. The most important aspect of deducing the permittivity was being able to determine these values at high frequency ranges; which in this case was deduced up to 70 GHz. The results were compared to those obtained when the permittivity of the unknown materials was found using the simulated reflection data. Figures 5.19 (a) and (b) illustrates the permittivity of PDMS that was deduced using the cross-ratio code technique.

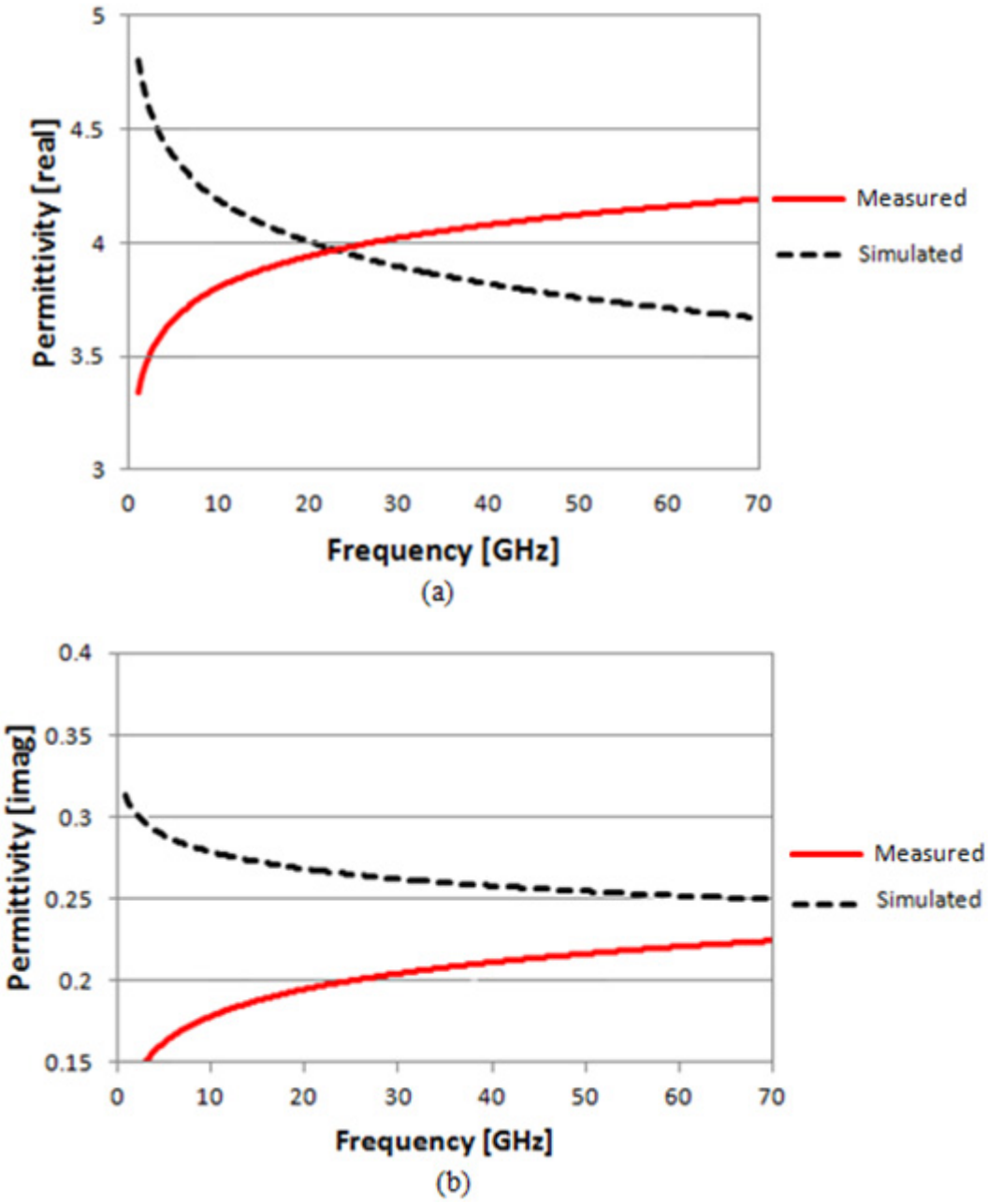

Figure 5.19 Complex Permittivity of PDMS using measured reflection coefficients in cross-ratio invariance coding technique. (a) Real Part and (b) Imaginary Part.

The results from the deduced permittivity of PDMS are shown in the figure above, when using the measured reflection coefficient data in the coding technique. A permittivity comparison was made to the results obtained when using the simulated reflection coefficient data. In the real part, the permittivity started at a value of ~3.4 and then reached 4 as it approached 35 GHz. It

then continued to increase to 4.1 and 4.2 as it neared 50-60 GHz, while leveling off to 4.3 at 70 GHz. These results differed from the simulated by a factor of 1 at lower frequencies, and then decreased to ~0.5 at higher frequencies. The imaginary part demonstrated a value of 0.15-0.18 from dc-to-20 GHz, and then increased to 0.23 as it approached higher frequencies. At the higher frequency level, the results only differed from the simulated values by a minimum factor of 0.02; whereas at lower frequencies a maximum difference factor of 0.15 was achieved. These results were due to the before mentioned simulation errors that occurred at lower frequencies when the reflection coefficient of PDMS was evaluated. Since majority of the simulation errors were seen at frequencies up to ~8 GHz, and then slowly affected higher frequencies, the lower frequency range produced the largest difference factor between measured and simulated data. However, it can be seen that this error became less of an impact on the permittivity results as the curves approached higher frequencies, where the measured permittivity agreed well with the simulated. Therefore, the deduced permittivity was close to the simulated values as it approached higher frequencies which allowed for a successful determination of the unknown material.

The permittivity of Silicon was then determined by implementing the measured reflection coefficient data in the invariance coding technique. The figure below illustrates the deduced complex permittivity of Silicon at high frequencies using measured reflection data.

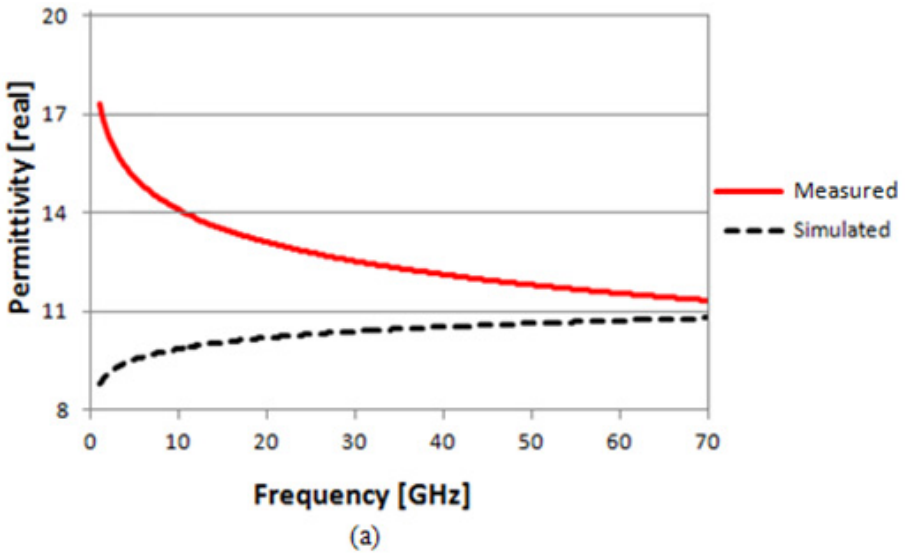

(a)

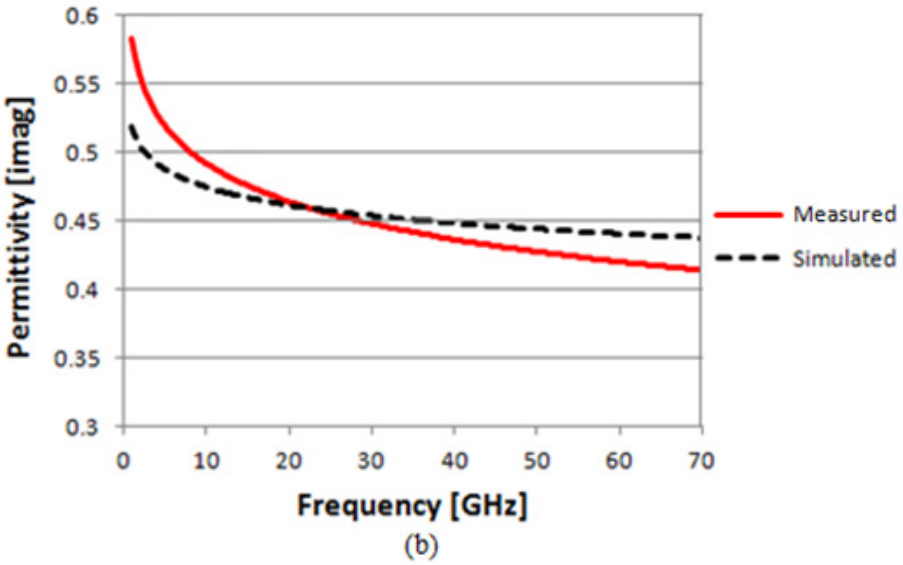

(b)

Figure 5.20 Complex Permittivity of Silicon using measured reflection coefficients in cross-ratio invariance coding technique. (a) Real Part and (b) Imaginary Part.

The above data shows the permittivity results for Silicon when using the measured reflection coefficient data in the coding technique. The data was compared to the results obtained when using the simulated reflection coefficient data in the coding technique. The results demonstrated the real part of the permittivity starting near a value of 17 and eventually decreasing to 12 as it approached 30 GHz. The curve then continued to decrease to approximately 11 as it neared the 70 GHz mark. The largest difference in this data from simulated results can be observed at lower frequencies (dc-to-15 GHz) by a maximum factor of 11; the difference factor however decreased and improved as it approached higher frequencies by reducing to a factor of nearly 0.7. Again, simulation errors that occurred at low frequencies when evaluating the reflection coefficient of Silicon caused the measured and simulated permittivity values to differ the most at the lower frequency range. The permittivity curves began to closely resemble at higher frequencies due to the simulation error having a reduced impact on the data as the frequency range increased. In the imaginary part, the behavior of the curve closely resembled that of the simulated data over the entire frequency range, where the largest difference factor obtained was 0.6; which was seen at low frequency levels close to dc.

Overall, the permittivity of the unknown materials that were deduced using the measured reflection data represented values close to those obtained with simulated results. Although larger difference factors in the data was seen at lower frequencies, this was expected due to the simulation error that occurred when the probe was in contact with the materials. Other discrepancies in the data were due to the capacitance that appeared between the materials and the coaxial probes. This caused each of the materials to behave differently than if they were simply resting in free space. Also, the metal chuck that the materials rested on during measuring also played a major role in determining accurate reflection data. Therefore, since the measured reflection data was slightly off from the simulated data, the deduced permittivity of each unknown was expected to differ. Lastly, after measuring the materials and finding the permittivity of the unknowns, it was realized that more accurate results could have been achieved if the permittivity values of the chosen calibration standards were closer to those of the unknown materials that were to be determined. This would have created a narrower calibration window for the unknown materials, and would have ultimately minimized any errors seen from their reflection coefficient data. However, in both cases, the permittivity values obtained could be used to determine the identity of each of the unknown materials if no other information was supplied.

5.7.1 Comparison of Permittivity Results Using Code vs. Measured Permittivity

To verify the accuracy of the determined permittivity when using the measured reflection coefficient data in the code technique, the results were then compared to the actual measured permittivity of the unknown material. Using the dielectric probe kit described in section 5.4, the permittivity of PDMS and Silicon were measured up to 14 GHz. Again, the system was first calibrated using air, an RF short, and in diluted water. Following the calibration, each material was placed in contact with the probe setup and the permittivities were retrieved from the software. Figure 5.21 shows the measured complex permittivity results of PDMS (up to 14 GHz)

compared to those obtained when implementing the reflection data in the cross-ratio invariance coding technique.

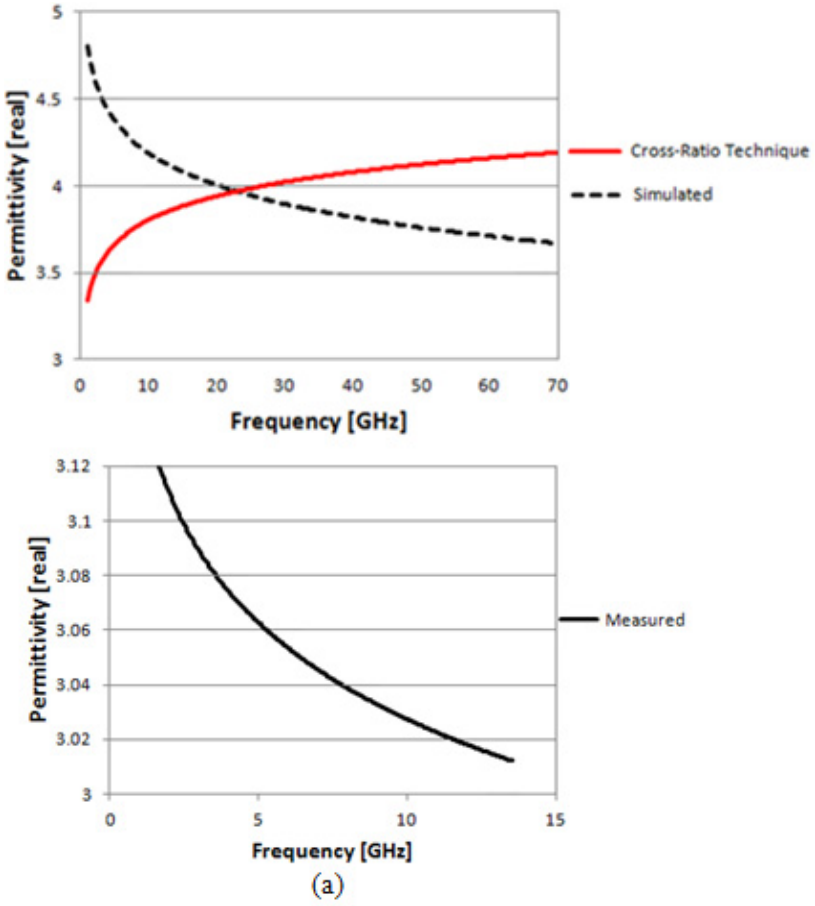

(a)

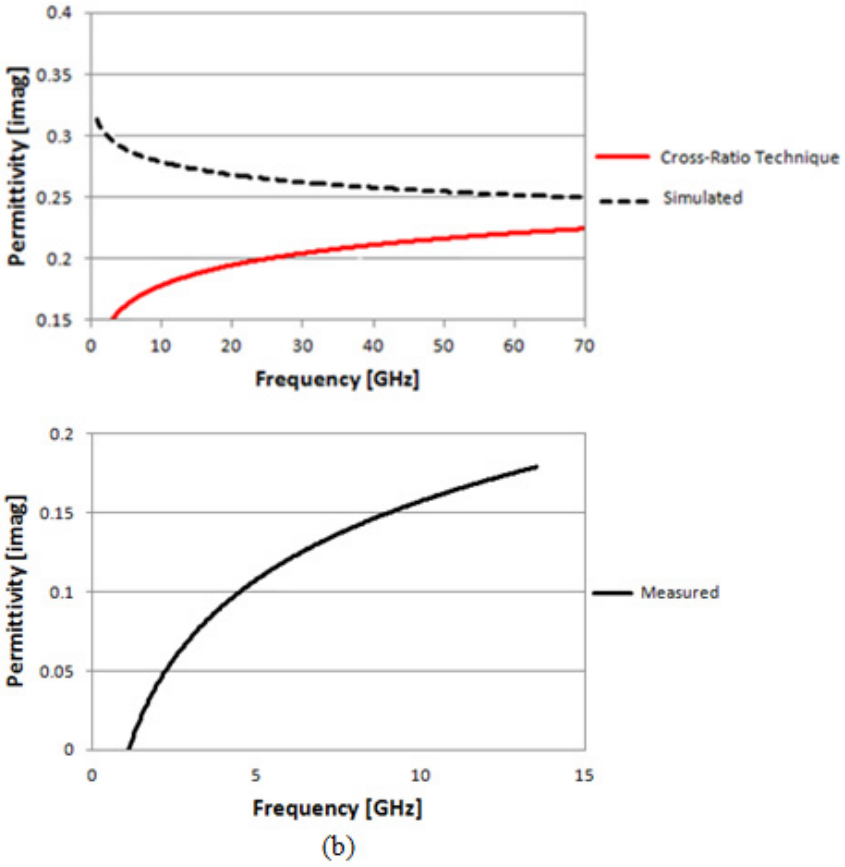

Figure 5.21 Results obtained using cross-ratio coding technique compared to measured complex permittivity of PDMS. (a) Real Part and (b) Imaginary Part.

The figure above illustrates a comparison of the results obtained using the coding technique and when the unknown material was actually measured. Due to limitations of the dielectric probe kit, results obtained were only capable of reaching up to 14 GHz. For the real part, it can be seen that the actual measured permittivity of PDMS reached a value of 3.12 at lower frequencies but then decreased to ~3.01 as it approached higher levels. It can be assumed that the curved leveled off near the 15 GHz mark and beyond since those values were unattainable. Therefore, the reference value for PDMS was 3.01, which differed from the coding technique values by ~ 0.8. For the imaginary, the measured value started near 0.05 and leveled off near 0.18 as it approached higher frequencies. Therefore, with a referenced imaginary value of 0.18, it differed from those values obtained using the coding technique by ~ 0.04.

The comparison of measured permittivity to results obtained using the coding technique for Silicon is shown in the figure below.

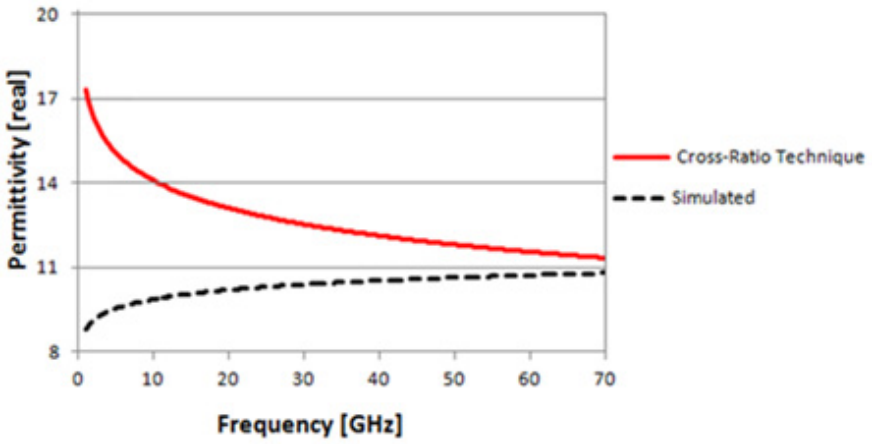

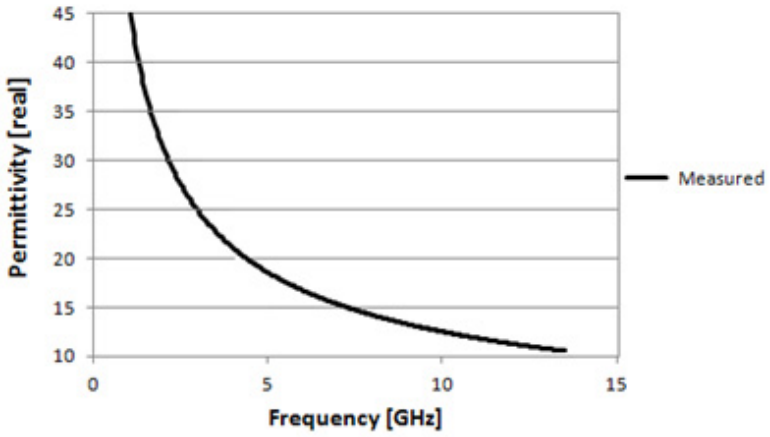

(a)

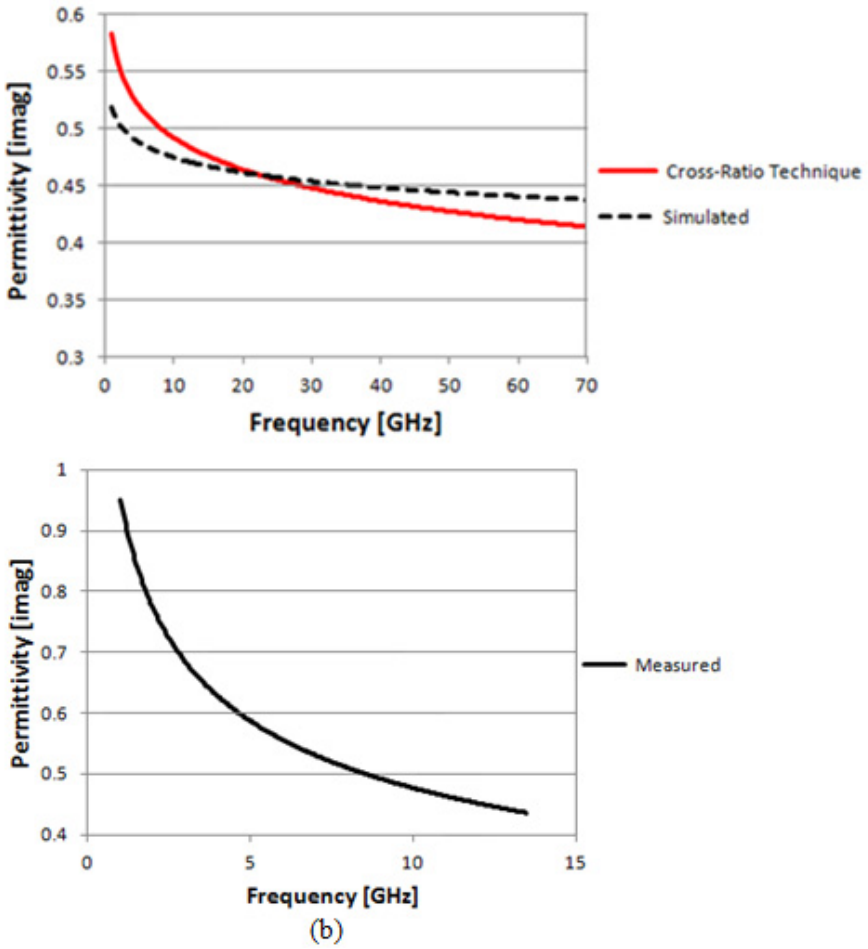

Figure 5.22 Results obtained using cross-ratio coding technique compared to measured complex permittivity of Silicon. (a) Real Part and (b) Imaginary Part.

In the figure above, the permittivity comparison of results obtained when using the coding technique and when measuring Silicon are shown. Again, the limitation of measuring equipment only allowed the measured permittivity to be determined up to 14 GHz. The real part showed that the probe system had a difficult time getting an accurate measurement of the Silicon at lower frequencies, with a value that started at 45; which is way beyond the expected value of any known silicon substrate. Several attempts were made to re-calibrate the system and repeat the measurement, but the probe system generated the same results. As the frequency range increased, it decreased and leveled off at ~10.7-11, which was assumed to be the reference value of Silicon. The measured value of silicon at lower frequencies compared poorly to the results obtained in the

code with a difference factor as high as 28. This major difference was due to discrepancies with the probe system being able to make good contact with a silicon substrate. At higher frequencies however, the coding technique behaved well compared to the measured results, only demonstrating a difference factor of ~0.4. For the imaginary part, the value started at 1 over a lower frequency range, and decreased to 0.45 as it approached higher frequencies. Therefore, the reference value for the imaginary part of Silicon was assumed to be 0.45. The results obtained when using the coding technique compared well to these results at higher frequencies, demonstrating a difference factor of 0.03. At lower frequencies however, the difference factor was greater reaching a value of ~0.4.

5.8 Coding Technique Difference Factor in Terms of Percentage Error

Lastly, the coding technique results for PDMS and Silicon using the simulated reflection coefficients were compared to those obtained using the measured reflection data. These results showed the difference factor between the simulated coding technique and the measured coding technique results of the unknown materials in terms of a percentage. Using the permittivity results above, the percent error was calculated for each difference factor at every 10 GHz of data over the entire frequency band up to 70 GHz. The equation below was used to calculate the percentage error between the coding technique results and the actual measured permittivity.

$$\frac{\left|Approximat\,eValue - Exact\ Value\right|}{\left|Exact\ Value\right|} \times 100 \qquad 5.1$$

In Equation 5.1, the results obtained using the simulated cross-ratio coding technique represented the approximate value, and the actual measured data used in the coding technique represented the exact value. The tables below represent the difference factor in terms of calculated percentage error at each range of frequency for PDMS and Silicon.

Table 5.1 Difference Factor of PDMS in Terms of Percentage Error

Frequency [GHz]	Simulated Coding Technique (real/imag)	Measured Coding Technique (real/imag)	Difference Factor (real/imag)	Percentage Error (real/imag)
dc	4.8/0.31	3.4/0.14	1.4/0.17	41%/121%
10	4.2/0.27	3.7/0.14	0.5/0.13	13.5%/93%
20	4/0.26	3.9/0.19	0.1/0.07	2.6%/36.8%
30	3.9/0.255	4/0.2	0.1/0.055	2.5%/27.5%
40	3.8/0.252	4.1/0.21	0.3/0.042	7.3%/20%
50	3.7/0.251	4.2/0.22	0.5/0.031	14%/14.1%
60	3.65/0.25	4.25/0.23	0.6/0.02	14.11%/8.7%
70	3.6/0.25	4.27/0.235	0.67/0.015	15.7%/6.4%

The table above shows the comparison of permittivity results obtained when using the simulated reflection coefficient data and the measured. The difference factor between the complex permittivity of PDMS at each frequency range is also shown. As seen above, once the difference factor was determined, the percentage error at each frequency range was then calculated. The results showed that for the real part of PDMS, the highest difference in percent error seen was at dc; this was again due to the micro-coaxial probe's behavior at lower frequencies. The best percentage error was seen from 20-to-30 GHz, but also behaved well as it approached the highest frequency range. In the real part, a big difference in percent error can be seen from dc-to-20 GHz, due to micro-coaxial probe inaccuracies during measuring. The percentage error performance did increase however; as it reached the 70 GHz mark.

The difference factor in terms of calculated percentage error for Silicon is shown in Table 5.2. From the table it can be seen that for Silicon, at majority of the frequency marks, the percentage error calculation proved that the measured and simulated coding technique results were closely related. For the real part, the largest percentage error was again seen at dc; reaching up to 50%. However, as it approached higher frequencies, an error as low as 1.8% was achieved, which demonstrated a good comparison between each set of data. The imaginary portion also

behaved very well across the wide frequency range. The highest percent error calculated was 10.3% at dc; and actually achieved a 0% percentage error from 20-to-30 GHz. This meant that the simulated and measured coding results were actually identical at those specific points on the curve.

Table 5.2 Difference Factor of Silicon in Terms of Percentage Error

Frequency [GHz]	Simulated Coding Technique (real/imag)	Measured Coding Technique (real/imag)	Difference Factor (real/imag)	Percentage Error (real/imag)
dc	8.8/0.52	17.5/0.58	8.7/0.06	49.7%/10.3%
10	10/0.47	14/0.5	4/0.03	28.6%/6%
20	10.8/0.46	13/0.46	2.2/0.0	16.9%/0%
30	10.85/0.45	12/0.45	1.15/0.0	9.6%/0%
40	10.9/0.45	11.7/0.44	0.8/0.01	6.8%/2.3%
50	10.95/0.44	11.5/0.43	0.55/0.01	4.8%/2.3%
60	10.97/0.44	11.3/0.42	0.33/0.02	2.9%/4.8%
70	10.99/0.44	11.2/0.41	0.21/0.03	1.88%/7.3%

5.9 Permittivity of Additional Unknown Material using Measured Reflection Coefficients

Following the development of the micro-coaxial probe flushed in silicon, the idea of attempting a parallel design using a Low temperature co-fired ceramic (LTCC) substrate was discussed. Although the design was not completed in this work, being able to determine its permittivity at high frequencies for the future probe design was critical. Therefore, the cross-ratio technique discussed in previous sections was also used to characterize the LTCC substrate that will be used to develop a micro-coaxial probe. The material under test was DuPont's 951 Green Tape, which had a dielectric constant of 7.8 at 3 GHz according to specifications [97]; however, if the substrate is to be used to develop a micro-coaxial probe, the permittivity at higher frequencies up to 70 GHz needed to be determined. This material was made of a thin sheet material (250μm) and was then fired in an oven to form a thicker and durable substrate (660μm). This was done by cycling the oven temperature every 90 minutes at ~800˚C. By firing the LTCC

substrate, the material was made thicker than the length of the micro-coaxial probe, which was recommended to help prevent any wave disruptions from penetrating the surface.

To determine the permittivity of the LTCC substrate, the reflection coefficients of the material were first measured and then compared to the simulated results. The figure below illustrates the measured reflection coefficients of the LTCC substrate in comparison with the simulated results.

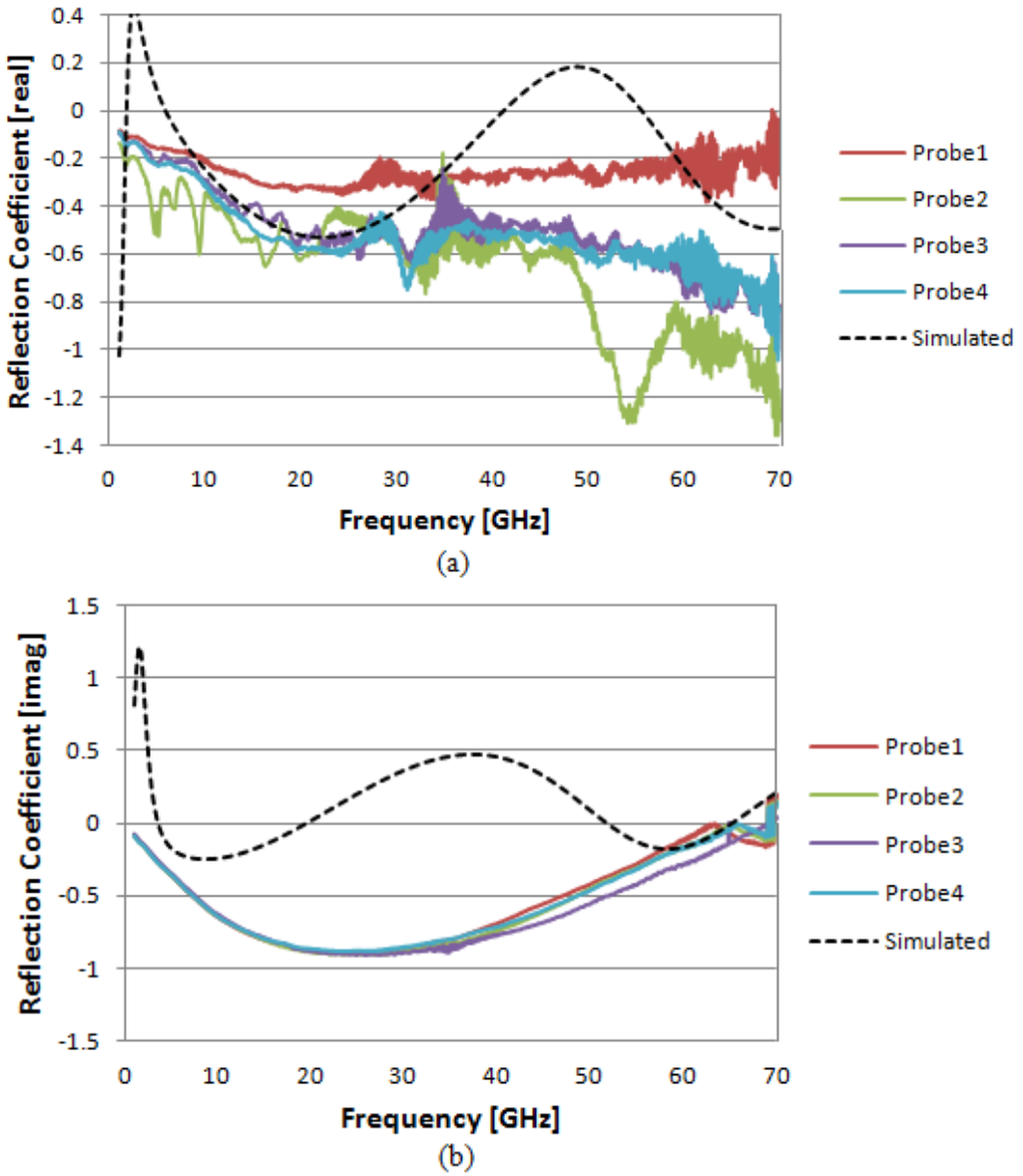

Figure 5.23 Measured reflection coefficients of Unknown material LTCC compared to simulated results. (a) Real Part and (b) Imaginary Part.

The results above show the measured reflection coefficient results compared to those simulated for LTCC. The real part demonstrated a reflection value of -0.1 to -0.3 from dc-to-25 GHz. This value then increased to -0.2 as it approached 50 GHz. Once it passed 50 GHz, it continued to increase to nearly -0.1 up to 70 GHz. This revealed a difference factor from the simulated results of ~0.03 at lower frequencies and ~1 as it approached the higher range. For the imaginary part, the measured data demonstrated a value of -0.1 to -0.8 from dc-to-25 GHz; this value then increased to -0.5 as it approached 50 GHz. Once it passed 50 GHz, it continued to increase to -0.1 up to 70 GHz. These imaginary results revealed a difference factor of about 0.4 at lower frequencies but then increased to ~ 1.2 from 50-to-70 GHz. The variance in measured to simulated data is again mostly due to the simulation error that occurred at lower frequencies when the probe was in contact with LTCC. Next, since Probe 1 data resembled the simulated reflection coefficient results the closest, it was then used to deduce the permittivity of the MUT. Figure 5.24 illustrates the complex permittivity of the LTCC substrate deduced using the cross-ratio technique at high frequencies.

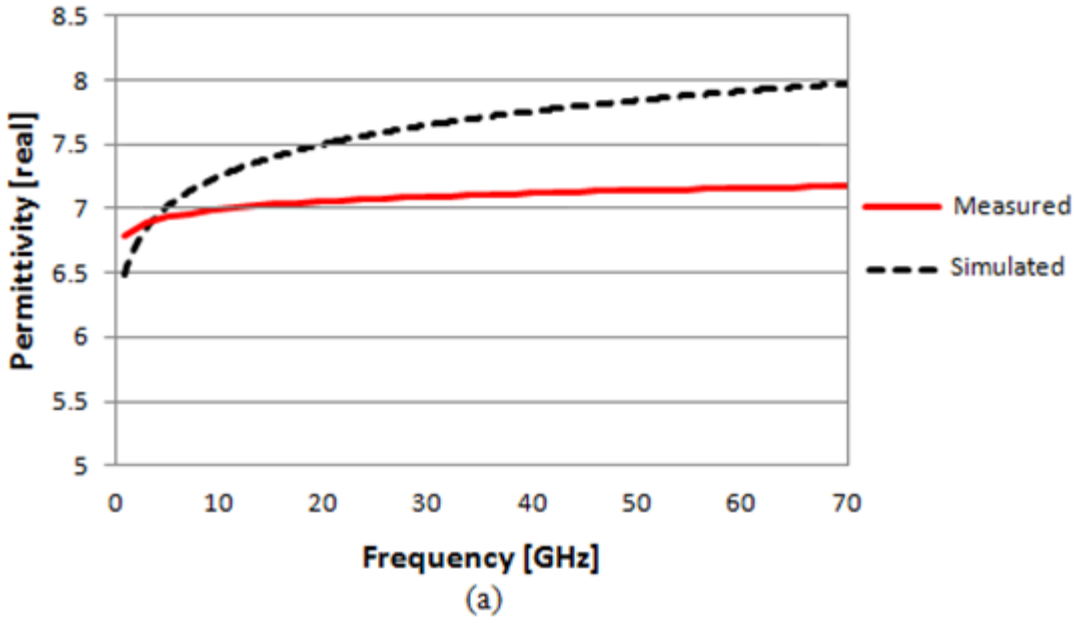

(a)

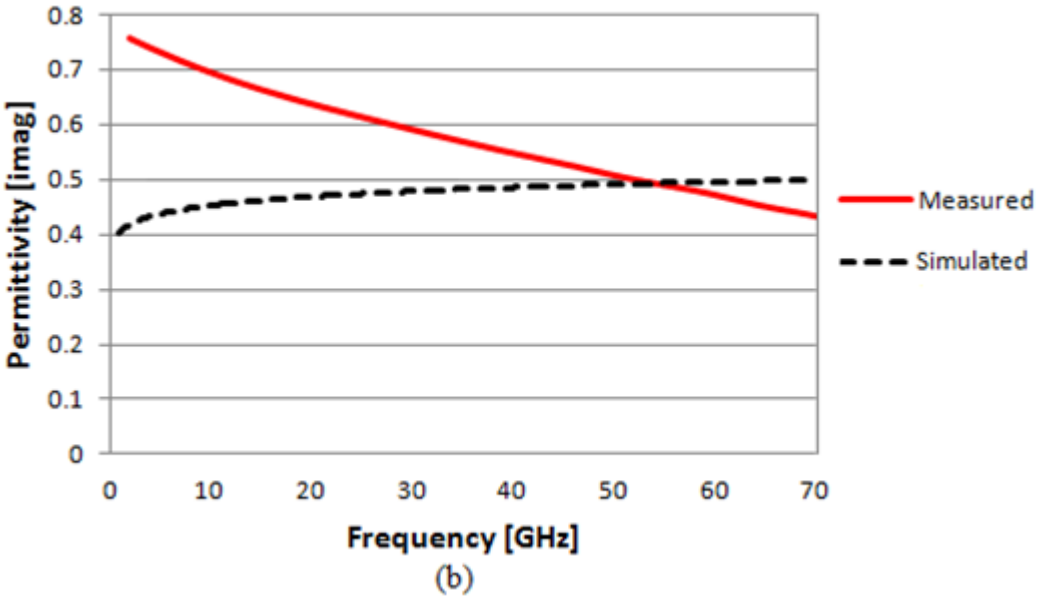

(b)

Figure 5.24 Complex Permittivity of LTCC using measured reflection coefficients in cross-ratio Invariance coding technique. (a) Real Part and (b) Imaginary Part.

The above data shows the complex permittivity results for LTCC when using the measured reflection coefficient data in the coding technique. The data was compared to the results obtained when using the simulated reflection coefficient data in the coding technique. Results demonstrated that for the real part, the measured permittivity values agreed well with the simulated, with a difference factor of 0.5 from dc-to-35 GHz and then only increasing to 0.8 as it approached 70 GHz. The imaginary part however, demonstrated variance with a difference factor of ~0.5 at lower frequencies, which was caused by the simulation error, but then decreases to 0.2 at higher frequencies as the errors begin to have less of an impact on the results. Lastly, the difference factors for the real and imaginary parts were utilized to determine the percent error at every 10 GHz. The error was calculated using the simulated permittivity as an approximate value, and the measured permittivity as the exact value. The table below shows the difference factor in terms of calculated percentage error for LTCC.

Table 5.3 Difference Factor of LTCC in Terms of Percentage Error

Frequency [GHz]	Simulated Coding Technique (real/imag)	Measured Coding Technique (real/imag)	Difference Factor (real/imag)	Percentage Error (real/imag)
dc	6.5/0.4	6.8/0.75	0.3/0.35	4.4%/46.6%
10	7.2/0.45	7/0.7	0.2/0.25	2.8%/35.7%
20	7.4/0.47	7.1/0.62	0.3/0.15	4.22%/24.2%
30	7.6/0.48	7.1/0.6	0.5/0.12	7%/20%
40	7.7/0.49	7.2/0.55	0.5/0.06	6.9%/10.9%
50	7.8/0.495	7.2/0.5	0.6/0.005	9%/1%
60	7.9/0.5	7.25/0.48	0.65/0.02	8.9%/4.2%
70	8/0.5	7.25/0.42	0.75/0.08	10.3%/19%

The difference factor in terms of calculated percentage error for LTCC is shown in Table 5.3 above. From the table it can be seen that for LTCC, the percentage error calculation proved that the measured and simulated coding technique results were somewhat related. For the real part, the largest percentage error was again seen at 70 GHz; reaching only 10%. At lower frequencies, an error as low as 2.8% was achieved, which demonstrated a good comparison between each set of data. The imaginary portion however, didn't agree as well as the real part. The highest percent error calculated was 46.6% at dc; and reached values of 19% and 20% at higher frequencies. This discrepancy in the data was expected seeing that the measured reflection coefficient values were different than the simulated values. Although a slight variance is seen for the exact permittivity and the approximate, the material can still be determined using the achieved value from the coding technique.

In summary, the unknown materials that were characterized using simulated and measured reflection coefficient data were accurate enough to determine what material was actually under test. Using the cross-ratio coding technique allowed the reflection data to be collected and deduced into a permittivity value. By simulating the material in contact with the micro-coaxial probe first, reference values were obtained for the expected permittivity values of

the unknown materials. These reference values were then compared to the actual permittivity values obtained using the measured reflection coefficient results and agreed well with the expected results. After comparing the permittivity results, the difference factor between each data set was determined at every 10 GHz mark over the entire dc-to-70 frequency band. These values were then used to determine the difference between measured and simulated code technique results in terms of percentage error. Following the calculation of percentage error, it was observed that results were poor at the dc-to-20 GHz range for the real and imaginary parts of each material. However, as the frequency range increased, the results improved and began to agree well with each other. These results prove that the micro-coaxial probe can successfully determine the permittivity of unknown materials at high frequencies with the highest percentage error only reaching 49%.

CHAPTER 6

CONCLUSIONS AND RECOMMENDATIONS FOR FUTURE RESEARCH

Through-wafer vertical micro-coaxial probes with inner and outer diameters of 100 and 300μm were developed for high frequency material characterization and millimeter wave packaging systems. These probes were developed using standard photolithography techniques, deep reactive ion etching, and a one step e-beam lithography process. The probes through holes were metalized using a novel filling method that allowed silver paste to be coursed into the miniaturized holes. The signal transmission capabilities of the probes were evaluated from port-to-port to verify their ability to characterize materials at high frequencies.

The signal transmission capability of several micro-coaxial probes was determined using high frequency RF characterization. By applying a signal (matched to 50 ohm) from the VNA directly to the micro-coaxial probes, their reflection coefficients from dc-to-70 GHz was measured using CPW pitch probe tips. The micro-coaxial probes demonstrated good signal transmission when the reflection coefficient was measured at port 1. At a center frequency of 60 GHz, a reflection coefficient of -18dB was observed, and at lower frequencies, values as low as -22dB were also obtained. An additional substrate was included on the bottom side of the coaxial probe which contained extended CPW lines used to verify its transducer gain capabilities. Following this, the coaxial probes demonstrated transducer gain less than -1.8dB over the entire range of frequency. Therefore, a three-dimensional micro-coaxial probe designed flush in silicon, capable of successful signal transmission at high frequencies, was developed for the first time.

In addition, the silicon based vertical micro-coaxial probes were used to characterize unknown materials at high frequencies by determining their permittivity using microwave measurements. Three known materials were chosen as calibration standards to be used in the cross-ratio invariance coding technique. The reflection coefficients of the 3 known materials were then measured and uploaded in the coding technique. The reflection coefficients of the unknown

materials were then measured and implemented in the code, where the permittivity of Silicon, PDMS, and LTCC was determined. The permittivity results from the measured reflection data was compared to results obtained when using the simulated reflection coefficients. When using several probes to characterize majority of the MUT's surface, the measured results agreed well with the simulated for both materials; demonstrating a maximum percentage error of 15% for PDMS 17% for Silicon, and 10.3% for LTCC at high frequencies beyond 20 GHz.

As a result of using the vertical micro-coaxial probe to characterize materials at high frequencies and to transmit signals in millimeter wave packaging systems, the probe device demonstrated its excellent dual capabilities for a variety of future commercial application. Implementing it in high frequency multi-level packaging systems as interconnects/transitions, as well as integrating it with unknown materials to determine their permittivity, this work introduced a useful and cost effective silicon based two-fold application developed for the first time. By designing the micro-coaxial probe in a silicon substrate, the compatibility with other high frequency RF modules and such is highly increased.

6.1 Recommendations for Future Research

The vertical micro-coaxial probe demonstrated good results during testing and could be useful when implemented in both applications. However, some design issues that were discovered during fabrication could affect the behavior of the probe device in the future. For example, the CPW lines on the front and backside on the coaxial probe were designed with a 5μm gap between signal and ground. This caused major issues when the probes were fabricated because the through holes that were etched in the silicon substrate created a non-uniform surface which prevented the photoresist from being evenly distributed for the CPW line pattern. Therefore, when the CPW line pattern was developed, some areas in between the signal and ground lines were poorly covered with photoresist. This caused an immediate device shortage because following the gold

deposition of the lines, areas not covered with resists contained gold after liftoff. Although the resist spin recipe was adjusted to achieve the desired results, a slight adjustment to increase the CPW line gap distance would reduce fabrication issues. This adjustment can improve the reflection coefficient results obtained for the micro-coaxial probe.

The inclusion of the additional substrate to extend the CPW lines can also be altered to improve the probe's signal transmission results, because the extended CPW lines were designed a little short of the required length. This was realized after the lines were fabricated and then integrated with the original substrate. It was then determined that even after dicing the micro-coaxial probes into smaller components, the extended lines were barely reachable after the local holes and cross hairs were aligned to one another. This caused issues when trying to measure the s-parameters at port 2 because the additional substrate had to be slightly shifted to the left to create more contact area for the probes to land. During the shift, it was assumed that the CPW lines on the backside and the additional substrate were misaligned which reduced the signal transmission abilities of the micro-coaxial probe. Therefore, increasing the length of the extended CPW lines would improve the transducer gain performance.

The same micro-coaxial probes were used to characterize materials at high frequencies, and the permittivity results when using measured reflection data agreed well with the simulated data. However, the cross-ratio coding technique would have provided more accurate permittivity results if more known materials were used to calibrate the system. This would have created more data for the code to use when compiling the measured reflection coefficients, improving its overall accuracy. Also, the chosen known materials had permittivity values of 4.2, 6.5, and 10.2, which were not in the range of the unknowns. Therefore, to further improve the accuracy of the coding technique, the chosen known materials should have permittivity values that cover the permittivity range from highest to lowest of the unknown materials permittivity that is to be determined. Furthermore, when the unknown materials reflection coefficients were measured,

they were resting on a metal chuck, which also affected the outcome of the permittivity results. Reducing the contact of the measured materials with the chuck would have to be included to increase reflection accuracy.

Additionally, with the characterization of the LTCC material, more progress can be made to develop the parallel micro-coaxial probe design. By determining the permittivity of LTCC at high frequencies, it has helped improve the overall performance of the device by providing it with a more accurate description of the material to be used. Also, further studies can be done on replacing the silver paste with nano-silver to metalize the through-holes; which could provide a better metallic connection between the probe and CPW lines. Using this type of metal could allow its temperature to be optimized for curing at a low temperature.

Finally, with the development of the vertical micro-coaxial probe, it was discovered that in future work, it could also be used to characterize the behavior of a millimeter wave device; for example a high frequency antenna. The antenna that could be used for this work has been published and is a CPW-fed folded dipole slot with a center frequency of 60 GHz, and can be reviewed for further detail in Appendix D [98]. However, the CPW feed of the antenna needs to be redesigned into a circular coaxial feed in order to electrically connect with the coaxial probe. Thus, as a next step towards proving the vertical micro-coaxial probe can characterize millimeter wave passive devices, the probe has to be integrated with the 60 GHz folded dipole slot antenna and evaluated.

REFERENCES

[1] L. F. Chen*, et al.*, *Microwave electronics: measurement and materials characterization*: Wiley Chichester, UK, 2004.

[2] D. I. Amey*, et al.*, "High frequency electrical characterization of electronic packaging materials: environmental and process considerations," in *Advanced Packaging Materials, 1998. Proceedings. 1998 4th International Symposium on*, 1998, pp. 123-128.

[3] I. C. Jeng*, et al.*, "Characterization of low loss materials for high frequency PCB application," in *Microsystems, Packaging, Assembly and Circuits Technology, 2007. IMPACT 2007. International*, 2007, pp. 373-376.

[4] R. Shaw*, et al.*, "The radio frequency characterization of conductive textile materials: a preliminary step for accurate antenna modeling," in *Antennas and Propagation Society International Symposium, 2005 IEEE*, 2005, pp. 431-434 vol. 4B.

[5] H. Yi and A. Sarri, "GPR Absorbing Material Characterisation Using an Open-Ended Coaxial Probe," in *Antennas and Propagation, 2007. EuCAP 2007. The Second European Conference on*, 2007, pp. 1-4.

[6] F. Declercq and H. Rogier, "Characterization of electromagnetic properties of textile materials for the use in wearable antennas," in *Antennas and Propagation Society International Symposium, 2009. APSURSI '09. IEEE*, 2009, pp. 1-4.

[7] T. Yilmaz*, et al.*, "Characterization and Testing of a Skin Mimicking Material for Implantable Antennas Operating at ISM Band (2.4 GHz-2.48 GHz)," *Antennas and Wireless Propagation Letters, IEEE,* vol. 7, pp. 418-420, 2008.

[8] S. Lambot*, et al.*, "Modeling of ground-penetrating Radar for accurate characterization of subsurface electric properties," *Geoscience and Remote Sensing, IEEE Transactions on,* vol. 42, pp. 2555-2568, 2004.

[9] L. V. Gaetano Panariello, and Gaetano Vitolo, "Efficient and Accurate Full-Wave Analysis of the Open-Ended Coaxial Cable," *IEEE Transactions on Microwave Theory and Techniques,* vol. 49, 2001.

[10] J. Krupka, "Frequency domain complex permittivity measurements at microwave frequencies," *Measurement Science and Technology,* vol. 17, 2006.

[11] J. Krupka and C. Weil, "Recent advances in metrology for the electromagnetic characterization of materials at microwave frequencies," in *Microwaves and Radar, 1998. MIKON '98., 12th International Conference on*, 1998, pp. 243-253 vol.4.

[12] J. Krupka*, et al.*, "Measurements of the complex permittivity of microwave circuit board substrates using split dielectric resonator and reentrant cavity techniques," in *Dielectric Materials, Measurements and Applications, Seventh International Conference on (Conf. Publ. No. 430)*, 1996, pp. 21-24.

[13] W. J. Ellison and J. M. Moreau, "Open-Ended Coaxial Probe: Model Limitations," *Instrumentation and Measurement, IEEE Transactions on,* vol. 57, pp. 1984-1991, 2008.

[14] M. Moukanda*, et al.*, "A Coaxial Probe Fixture Used for Extracting Complex Permittivity of Thin Layers," in *Wireless and Microwave Technology Conference, 2006. WAMICON '06. IEEE Annual*, 2006, pp. 1-4.

[15] D. L. Gershon*, et al.*, "Open-ended coaxial probe for high-temperature and broad-band dielectric measurements," *Microwave Theory and Techniques, IEEE Transactions on,* vol. 47, pp. 1640-1648, 1999.

[16] *Ansys HFSS*. Available: http://www.ansys.com/Products/Simulation+Technology/Electromagnetics/High-Performance+Electronic+Design/ANSYS+HFSS

[17] M. W. Hyde and M. J. Havrilla, "Design of an open-ended coaxial probe for broadband, low-footprint nondestructive characterization of PEC-backed materials," in *Instrumentation and Measurement Technology Conference (I2MTC), 2012 IEEE International*, 2012, pp. 1599-1602.

[18] D. Popovic*, et al.*, "Precision open-ended coaxial probes for in vivo and ex vivo dielectric spectroscopy of biological tissues at microwave frequencies," *Microwave Theory and Techniques, IEEE Transactions on,* vol. 53, pp. 1713-1722, 2005.

[19] O. Yisok and K. Yeon-Geon, "Analysis of wave reflection from open-ended coaxial lines and application to the measurement of soil moisture and salinity," in *Antennas and Propagation Society International Symposium, 1998. IEEE*, 1998, pp. 2010-2013 vol.4.

[20] S. O. Nelson*, et al.*, "Study of Fruit Permittivity Measurements for Quality Detection," in *Instrumentation and Measurement Technology Conference Proceedings, 2008. IMTC 2008. IEEE*, 2008, pp. 1009-1011.

[21] M. Bedouani, "Electrical characterization of printed circuit board materials for high frequency applications," in *Electronic Manufacturing Technology Symposium, 1992. IEMT 1992. 12th International*, 1992, pp. 253-262.

[22] M. N. Afsar*, et al.*, "Direct broadband microwave characterization of biological tissues using the coaxial probe technique," in *Precision Electromagnetic Measurements Digest, 2008. CPEM 2008. Conference on*, 2008, pp. 530-531.

[23] M. Obol*, et al.*, "Using Coaxial Probe for Broadband Microwave Characterization of Biological Tissues," in *Microwave Conference, 2008. EuMC 2008. 38th European*, 2008, pp. 416-419.

[24] T. W. Athey*, et al.*, "Measurement of Radio Frequency Permittivity of Biological Tissues with an Open-Ended Coaxial Line: Part I," *Microwave Theory and Techniques, IEEE Transactions on,* vol. 30, pp. 82-86, 1982.

[25] J. Fitzpatrick, "Error Models for Systems Measurements," *Microwave Journal,* vol. 21, pp. 63-66, 1978.

[26] D. M. Hagl*, et al.*, "Sensing volume of open-ended coaxial probes for dielectric characterization of breast tissue at microwave frequencies," *Microwave Theory and Techniques, IEEE Transactions on,* vol. 51, pp. 1194-1206, 2003.

[27] F. Jaspard and M. Nadi, "Open ended coaxial line for electrical characterization of human blood," in *Engineering in Medicine and Biology Society, 2001. Proceedings of the 23rd Annual International Conference of the IEEE*, 2001, pp. 3121-3123 vol.3.

[28] H. Hyeonseok*, et al.*, "110 GHz broadband measurement of permittivity on human epidermis using 1 mm coaxial probe," in *Microwave Symposium Digest, 2003 IEEE MTT-S International*, 2003, pp. 399-402 vol.1.

[29] S. O. Nelson and P. G. Bartley, "Measuring frequency- and temperature-dependent permittivities of food materials," *Instrumentation and Measurement, IEEE Transactions on,* vol. 51, pp. 589-592, 2002.

[30] D. L. C. a. S. M. Lesch, "Apparent soil electrical conductivity measurements in agriculture," *Computers and Electronics in Agriculture,* vol. 46, pp. 11-43, 2005.

[31] W. E. Wightman, "Application of Geophysical Methods to Highway Related Problems," *Federal Highway Administration,* 2003.

[32] E. D. Lynch, "Experimental HF radar for sub-surface sensing," in *Seventh International Conference on Ground Penetrating Radar*, Lawrence, Kansas, 1998.

[33] C. Ming and C. Chi-Chih, "Wideband in-situ soil permittivity coaxial probe," in *Antennas and Propagation (APSURSI), 2011 IEEE International Symposium on*, 2011, pp. 346-349.

[34] Y. Hyoung-sun*, et al.*, "In-situ broadband soil measurements: Dielectric and magnetic properties," in *Geoscience and Remote Sensing Symposium (IGARSS), 2010 IEEE International*, 2010, pp. 4483-4486.

[35] R. Xinhua*, et al.*, "Characterization of high-temperature ceramic materials at microwave frequencies for MEMS applications," in *Wireless and Microwave Technology Conference, 2009. WAMICON '09. IEEE 10th Annual*, 2009, pp. 1-4.

[36] S. Dalmia*, et al.*, "Characterization of thin film organic materials at high frequency," in *Electrical Performance of Electronic Packaging, 2001*, 2001, pp. 133-136.

[37] D. I. Amey*, et al.*, "High frequency electrical characterization of electronic packaging materials: environmental and process considerations," in *Advanced Packaging Materials, 1998. Proceedings. 1998 4th International Symposium on*, 1998, pp. 123-128.

[38] J. Audet and N. Nanju, "High frequency loss characterization of FCPBGA package materials with humidity and temperature variation," in *Electrical Performance of Electronic Packaging, 2008 IEEE-EPEP*, 2008, pp. 221-224.

[39] W. Shoujun, *et al.*, "A new technique for measuring electromagnetic properties of materials with an open-ended coaxial probe," in *Microwave Conference Proceedings, 1997. APMC '97, 1997 Asia-Pacific*, 1997, pp. 921-924 vol.3.

[40] Y. Sung-Ku, *et al.*, "Quasi-Coaxial Vertical via Transitions for 3-D Packages Using Anodized Aluminum Substrates," *Microwave and Wireless Components Letters, IEEE,* vol. 19, pp. 365-367, 2009.

[41] R. Crunelle, *et al.*, "Vertical coaxial transitions for MM-waves 3D integration technologies," in *Microwave Conference (EuMC), 2010 European*, 2010, pp. 101-104.

[42] W. Wei-Cheng, *et al.*, "Design, Fabrication, and Characterization of Novel Vertical Coaxial Transitions for Flip-Chip Interconnects," *Advanced Packaging, IEEE Transactions on,* vol. 32, pp. 362-371, 2009.

[43] B. J. LaMeres, *et al.*, "Novel 3-D Coaxial Interconnect System for Use in System-in-Package Applications," *Advanced Packaging, IEEE Transactions on,* vol. 33, pp. 37-47, 2010.

[44] J. Boone, "Silicon Based Vertical Micro-Coaxial Transition for High Frequency Packaging Technologies," *Progress In Electromagnetics Research B,* vol. 50, pp. 1-17, 2013.

[45] G. Hilson, "Small-scale mining and its socio-economic impact in developing countries," *Natural Resources Forum,* vol. 26, pp. 3-13, 2002.

[46] J. Martinez-Alier, "Mining conflicts, environmental justice, and valuation," *Journal of Hazardous Materials,* vol. 86, pp. 153-170, 2001.

[47] A. Müezzinogˇlu, "A Review of Environmental Considerations on Gold Mining and Production," *Critical Reviews in Environmental Science and Technology,* vol. 33, pp. 45-71, 2003/01/01 2003.

[48] G. HILSON, "PUTTING THEORY INTO PRACTICE: HOW HAS THE GOLD MINING INDUSTRY INTERPRETED THE CONCEPT OF SUSTAINABLE DEVELOPMENT?," *Mineral Resources Engineering,* vol. 10, pp. 397-413, 2001.

[49] G. M. Mudd, "Global trends in gold mining: Towards quantifying environmental and resource sustainability," *Resources Policy,* vol. 32, pp. 42-56, 2007.

[50] S. Durucan, *et al.*, "Mining life cycle modelling: a cradle-to-gate approach to environmental management in the minerals industry," *Journal of Cleaner Production,* vol. 14, pp. 1057-1070, 2006.

[51] S. H. Castro and M. Sánchez, "Environmental viewpoint on small-scale copper, gold and silver mining in Chile," *Journal of Cleaner Production,* vol. 11, pp. 207-213, 2003.

[52] S. M. Kambani, "Small-scale mining and cleaner production issues in Zambia," *Journal of Cleaner Production,* vol. 11, pp. 141-146, 2003.

[53] M. M. Veiga*, et al.*, "Mining with communities," *Natural Resources Forum,* vol. 25, pp. 191-202, 2001.

[54] J. Howard*, et al.*, "Total mercury loadings in sediment from gold mining and conservation areas in Guyana," *Environmental Monitoring and Assessment,* vol. 179, pp. 555-573, 2011/08/01 2011.

[55] G. M. Hilson, "The future of small-scale mining: environmental and socioeconomic perspectives," *Futures,* vol. 34, pp. 863-872, 2002.

[56] L. D. Lacerda, "Global Mercury Emissions from Gold and Silver Mining," *Water, Air, and Soil Pollution,* vol. 97, pp. 209-221, 1997/07/01 1997.

[57] W. Salomons, "Environmental impact of metals derived from mining activities: Processes, predictions, prevention," *Journal of Geochemical Exploration,* vol. 52, pp. 5-23, 1995.

[58] A. M. Esteves, "Mining and social development: Refocusing community investment using multi-criteria decision analysis," *Resources Policy,* vol. 33, pp. 39-47, 2008.

[59] P. T. Anastas and J. B. Zimmerman, "Peer Reviewed: Design Through the 12 Principles of Green Engineering," *Environmental Science & Technology,* vol. 37, pp. 94A-101A, 2003/03/01 2003.

[60] *End of Life*. Available: http://www.gdrc.org/uem/lca/g-fiv.html

[61] W. Rifer and D. Stitzhal, "Electronic product design for end-of-life management: a policy perspective," in *Electronics and the Environment, 2002 IEEE International Symposium on*, 2002, pp. 284-289.

[62] J. Grosinger*, et al.*, "Determining the Dielectric Properties of a Car Tire for an Advanced Tire Monitoring System," in *Vehicular Technology Conference Fall (VTC 2009-Fall), 2009 IEEE 70th*, 2009, pp. 1-5.

[63] D. M. Pozar, *Microwave Engineering*, 3rd ed.: John Wiley & Sons, 2005.

[64] G. Gonzalez, *Microwave Transistor Amplifiers*, 2nd ed.: Prentice Hall, 1996.

[65] S. E. S. D. B. Rutledge, and A. T. Adams, "Infrared Phys.," vol. 18, p. 713, 1978.

[66] K. M. Strohm*, et al.*, "Silicon Micromachined CPW Transmission Lines," in *Microwave Conference, 2002. 32nd European*, 2002, pp. 1-4.

[67] *Optical Lithography*. Available: http://www.ece.gatech.edu/research/labs/vc/theory/photolith.html

[68] *Photolithography*. Available: http://www.photoresists.eu/photoresist_1622.html

[69] J. S. Albert Folch, Joan Esteve, and Javier Tejada, "High-vaccum versus "environmental" electron beam deposition," *Journal of Vaccum Science and Technology B,* vol. 14, 1996.

[70] *E-beam Image*. Available: http://www.engr.uky.edu/~cense/images/ebeam2.gif

[71] C. Kuo-Shen, *et al.*, "Effect of process parameters on the surface morphology and mechanical performance of silicon structures after deep reactive ion etching (DRIE)," *Microelectromechanical Systems, Journal of,* vol. 11, pp. 264-275, 2002.

[72] *Cascade Probe Station*. Available: http://www.cmicro.com/products/probe-systems/

[73] *Probe Tips*. Available: http://www.micromanipulator.com/products/product.php?item=157&cat=161

[74] *IEEE GPIB Cables*. Available: http://cp.literature.agilent.com/litweb/pdf/5989-1889EN.pdf

[75] *AutoCAD*. Available: http://usa.autodesk.com/autocad/

[76] A. Cenanovic, Martius, S., Kilian, A., Schur, J., Schmidt, L. P., "Non destructive complex permittivity determination of glass material with planar and convex surface," in *Microwave Conference (GeMIC), 2011 German*, 2011, pp. 1-4.

[77] A. M. Paz, *et al.*, "Measurement of the Dielectric Properties of Sawdust Between 0.5 and 15 GHz," *Instrumentation and Measurement, IEEE Transactions on,* vol. 60, pp. 3384-3390, 2011.

[78] E. C. Burdette, *et al.*, "In Vivo Probe Measurement Technique for Determining Dielectric Properties at VHF through Microwave Frequencies," *Microwave Theory and Techniques, IEEE Transactions on,* vol. 28, pp. 414-427, 1980.

[79] T. Michiyama, *et al.*, "Obliquely cut open ended coaxial probe for obtaining complex permittivity of lossy materials," in *Microwave Conference, 2006. APMC 2006. Asia-Pacific*, 2006, pp. 587-590.

[80] M. Dionigi, *et al.*, "A new resonant probe for dielectric permittivity measurement," in *Microwave Conference, 2004. 34th European*, 2004, pp. 673-676.

[81] RO3000. Available: http://www.rogerscorp.com/acm/products/15/RO3000-RO3200-series-and-RO3730-High-Frequency-Laminates-PTFE-Ceramic.aspx

[82] FR-4. Available: http://www.rogerscorp.com/acm/products/16/RO4000-Series-High-Frequency-Circuit-Materials-Woven-glass-reinforced-ceramic-filled-thermoset.aspx

[83] J. U. Knickerbocker, *et al.*, "3-D Silicon Integration and Silicon Packaging Technology Using Silicon Through-Vias," *Solid-State Circuits, IEEE Journal of,* vol. 41, pp. 1718-1725, 2006.

[84] N. S. Tambe and B. Bhushan, "Micro/nanotribological characterization of PDMS and PMMA used for BioMEMS/NEMS applications," *Ultramicroscopy,* vol. 105, pp. 238-247, 2005.

[85] J. M. Anderson*, et al.*, "Dielectric measurements using a rational function model," *Microwave Theory and Techniques, IEEE Transactions on,* vol. 42, pp. 199-204, 1994.

[86] A. M. Grishin and V. P. Denysenkov, "Broad band microwave probe for nondestructive test of dielectric coatings," in *Applications of Ferroelectrics, 2002. ISAF 2002. Proceedings of the 13th IEEE International Symposium on*, 2002, pp. 91-93.

[87] A. Kraszewski*, et al.*, "ANA Calibration Method for Measurements of Dielectric Properties," *Instrumentation and Measurement, IEEE Transactions on,* vol. 32, pp. 385-387, 1983.

[88] D. K. Misra, "A Quasi-Static Analysis of Open-Ended Coaxial Lines (Short Paper)," *Microwave Theory and Techniques, IEEE Transactions on,* vol. 35, pp. 925-928, 1987.

[89] J. R. Mosig*, et al.*, "Reflection of an open-ended coaxial line and application to nondestructive measurement of materials," *Instrumentation and Measurement, IEEE Transactions on,* vol. IM-30, pp. 46-51, 1981.

[90] A. Nyshadham*, et al.*, "Permittivity measurements using open-ended sensors and reference liquid calibration-an uncertainty analysis," *Microwave Theory and Techniques, IEEE Transactions on,* vol. 40, pp. 305-314, 1992.

[91] M. A. Stuchly and S. S. Stuchly, "Equivalent circuit of an open-ended coaxial line in a lossy dielectric," *Instrumentation and Measurement, IEEE Transactions on,* vol. IM-31, pp. 116-119, 1982.

[92] P. De Langhe*, et al.*, "Measurement of low-permittivity materials based on a spectral-domain analysis for the open-ended coaxial probe," *Instrumentation and Measurement, IEEE Transactions on,* vol. 42, pp. 879-886, 1993.

[93] M. Grady*, et al.*, "Improvements in cross ratio invariance techniques for coaxial probe dielectric measurements," in *Microwave Measurement Conference (ARFTG), 2012 79th ARFTG*, 2012, pp. 1-7.

[94] K. F. Staebell and D. Misra, "An experimental technique for in vivo permittivity measurement of materials at microwave frequencies," *Microwave Theory and Techniques, IEEE Transactions on,* vol. 38, pp. 337-339, 1990.

[95] O. S. Gefle*, et al.*, "The field dependence of the complex permittivity of filled composites," in *Power Tech, 2005 IEEE Russia*, 2005, pp. 1-3.

[96] M. Grady, "Coaxial Probe for High Temperature Dielectric Characterization," Electrical Engineering, Auburn University 2010.

[97] *LTCC*. Available: http://www2.dupont.com/MCM/en_US/assets/downloads/prodinfo/951LTCCGreenTape.pdf

[98] J. Boone*, et al.*, "Coplanar-waveguide-fed folded dipole slot antenna for wireless local area network applications and V-band frequency operations," *Microwaves, Antennas & Propagation, IET,* vol. 6, pp. 583-587, 2012.

APPENDICES

Appendix A: Process Flow for Fabrication of Micro-Coaxial Probe

Step 1: Substrate Cleaning

Rinse in DI water and N_2 dry

Step 2: Photolithography

Layer 1- Coaxial Vias

Spin coat – HMDS; spin speed – 3000RPM; time – 30 seconds

Spin coat – AZ4620 positive photoresist; (1) spin speed – 500 RPM; time – 10 seconds; (2) spin speed – 1000 RPM; time – 60 seconds

Soft bake – Oven; T=100˚C for 20 minutes

Rehydration – Leave in open air for 24 hours

Expose – Karl Suss Mask aligner; 13 seconds exposure to UV at 25mW/cm^2

Develop – AZ 400K 1:4 developer; Constant immersion developing at room temperature for 4-5 minutes

Rinse in Di water and N_2 dry

Pattern check: Optical Microscope

Hard bake – Oven; T=100˚C for 30 minutes

Step 3: Deep Reactive Ion Etching (DRIE)

Run oxide clean in the chamber to remove any debris from previous etching

Perform temporization in chamber and heat the substrate holder to -15˚C

Season the chamber by running the 30 minute silicon etching recipe that will be used (should only need to run for 20 minutes)

Load sample onto substrate holder by applying fambling oil to backside for bonding.

Run 30 minute silicon etching recipe to etch 300μm deep through the silicon substrate (etch rate ~10μm/min)

Through-hole check: Remove substrate from chamber and verify that etching is complete using optical microscope.

Note: If etching is not complete, run silicon etching recipe again for 5 minutes and remove substrate.

Step 4: Removal of fambling oil

Place substrate in Plasma reactive ion etcher with the side covered in fambling oil facing up; Power – 200mW; Etch Time – 5 minutes

Step 5: Metallization of Coaxial Vias

Carefully rest substrate in one hand and apply diluted silver paste onto sharp razor blade. Take razor blade and gently apply to surface of silicon substrate by sweeping blade across the holes continuously, evenly coursing the paste into the formed through holes. Repeat this process until silver paste can be seen leaking out of through holes from the backside of the wafer.

Step 6: Removal of excess silver paste

Immerse substrate with filled through holes in Acetone until all photoresist is removed.

Rinse in DI water and N_2 dry

Step 7: Photolithography

Layer 2- Top side CPW Lines

Spin coat – Futurrex 3000 PY negative resist; spin speed – 1000 RPM; time – 30 seconds

Soft bake – Hot plate; T=150˚C for 60 seconds

Expose – Karl Suss Mask aligner; 23 seconds exposure to UV light at 17mW/cm^2 and hard bake on hot plate; T=100˚C for 60 seconds

Develop – RD 6 developer; Immersion developing at room temperature for 17 seconds

Rinse in DI water and N_2 dry

Pattern check: Optical Microscope

Step 8: Metal Deposition

Electron Beam – Cr and Au

Pressure – 5e^{-6} Torr, Current – .014 A and 0.15 A for Cr and Au, respectively; Deposition rate – 0.3Å/sec for Cr and 1.5Å/sec for Au.

Step 9: Metal Lift-Off

Immerse the substrate in Acetone until all the unwanted metal peels off from the substrate.

Rinse in DI water and N_2 dry

Deposition pattern check: Optical Microscope

Step 10: Photolithography

Layer 3- Bottom side CPW Lines

Repeat step 7

Step 11: Metal Deposition (Bottom side CPW Lines)

Repeat step 8

Step 12: Metal Lift-Off (Bottom side CPW Lines)

Repeat step 9

Step 13: Photolithography

Layer 4- Local Alignment Holes (Top Side)

Repeat step 2

Step 14: DRIE of Local Alignment Holes

Repeat step 3

Immerse substrate with etched local alignment holes in Acetone until all photoresist is removed.

Rinse in DI water and N_2 dry

Appendix B: Process Flow for Fabrication of Extended CPW Lines (Additional Substrate)

Step 1: Substrate Cleaning

Rinse in DI water and N_2 dry

Step 2: Photolithography

Layer 1- Extended CPW Lines

Spin coat – Futurrex 3000 PY negative resist; spin speed – 1000 RPM; time – 30 seconds

Soft bake – Hot plate; T=150˚C for 60 seconds

Expose – Karl Suss Mask aligner; 23 seconds exposure to UV light at 17mW/cm^2

Develop – RD 6 developer; Immersion developing at room temperature for 17 seconds

Rinse in DI water and N_2 dry

Pattern check: Optical Microscope

Step 3: Metal Deposition

Electron Beam – Cr and Au

Pressure – 5e^{-6} Torr, Current – .014 A and 0.15 A for Cr and Au, respectively; Deposition rate – 0.3Å/sec for Cr and 1.5Å/sec for Au.

Step 4: Metal Lift-Off

Immerse the substrate in Acetone until all the unwanted metal peels off from the substrate.

Rinse in DI water and N_2 dry

Deposition pattern check: Optical Microscope

Appendix C: Cross-Ratio Invariance Coding Technique Used to Deduce Permittivity of Unknown Materials (MATLAB)

```
clear all
clc
close all
format long

t_total=tic;

cmTOin =(1/(2.54*1e-2));
inTOcm=(2.54*1e-2);

%% -------------radius of probe--------------------
b=150e-6; %outer rad or dia
a=50e-6; %inner rad or diametr
eps_c=11.7; %permmitivty of probe dielcetroc

%% ----------------------------------------------

 %% -----------TAKE INTEGRALS----------------------------

%takes about 20 seconds for original I1 so.....DONT USE
% F = @(phiP,rhoP,rho) (cos(phiP))./(rho.^2 + rhoP.^2 -
2*rho.*rhoP.*cos(phiP)).^(1/2);
% I1 = triplequad(F,pi/967,pi,a,b,a,b,[],@quadv);

%use this I1 instead
N=2;
M=@(rho,rhoP)
(pi/2).*[1+(1/(2)).^2.*((4.*rho.*rhoP)./((rho+rhoP).^2)).^2+...
    (doublefact(2*N-
1)./(doublefact(2*N))).^2.*((4.*rho.*rhoP)./((rho+rhoP).^2)).^(2*N)+...
    (doublefact(3*N-
1)./(doublefact(3*N))).^2.*((4.*rho.*rhoP)./((rho+rhoP).^2)).^(3*N)+...
    (doublefact(4*N-
1)./(doublefact(4*N))).^2.*((4.*rho.*rhoP)./((rho+rhoP).^2)).^(4*N)+...
    (doublefact(5*N-
1)./(doublefact(5*N))).^2.*((4.*rho.*rhoP)./((rho+rhoP).^2)).^(5*N)+...
    (doublefact(6*N-
1)./(doublefact(6*N))).^2.*((4.*rho.*rhoP)./((rho+rhoP).^2)).^(6*N)+...
    (doublefact(7*N-
1)./(doublefact(7*N))).^2.*((4.*rho.*rhoP)./((rho+rhoP).^2)).^(7*N)+...
    (doublefact(8*N-
1)./(doublefact(8*N))).^2.*((4.*rho.*rhoP)./((rho+rhoP).^2)).^(8*N)+...
    (doublefact(9*N-
1)./(doublefact(9*N))).^2.*((4.*rho.*rhoP)./((rho+rhoP).^2)).^(9*N)+...
    (doublefact(10*N-
1)./(doublefact(10*N))).^2.*((4.*rho.*rhoP)./((rho+rhoP).^2)).^(10*N)+.
..
```

```
    (doublefact(11*N-
1)/(doublefact(11*N))).^2.*((4.*rho.*rhoP)./((rho+rhoP).^2)).^(11*N)+..
.
    (doublefact(12*N-
1)/(doublefact(12*N))).^2.*((4.*rho.*rhoP)./((rho+rhoP).^2)).^(12*N)+..
.
    (doublefact(13*N-
1)/(doublefact(13*N))).^2.*((4.*rho.*rhoP)./((rho+rhoP).^2)).^(13*N)+..
.
    (doublefact(14*N-
1)/(doublefact(14*N))).^2.*((4.*rho.*rhoP)./((rho+rhoP).^2)).^(14*N)+..
.
    (doublefact(15*N-
1)/(doublefact(15*N))).^2.*((4.*rho.*rhoP)./((rho+rhoP).^2)).^(15*N)+..
.
    (doublefact(16*N-
1)/(doublefact(16*N))).^2.*((4.*rho.*rhoP)./((rho+rhoP).^2)).^(16*N)+..
.
    (doublefact(17*N-
1)/(doublefact(17*N))).^2.*((4.*rho.*rhoP)./((rho+rhoP).^2)).^(17*N)+..
.
    (doublefact(18*N-
1)/(doublefact(18*N))).^2.*((4.*rho.*rhoP)./((rho+rhoP).^2)).^(18*N)+..
.
    (doublefact(19*N-
1)/(doublefact(19*N))).^2.*((4.*rho.*rhoP)./((rho+rhoP).^2)).^(19*N)+..
.
    (doublefact(20*N-
1)/(doublefact(20*N))).^2.*((4.*rho.*rhoP)./((rho+rhoP).^2)).^(20*N)]..
.
    ./(rho+rhoP); %numerator is elliptic integral of 1st kind

I1a=2*dblquad(M,a,b,a,b,[],@quadv);
F1 = @(phiP,rhoP,rho) (cos(phiP)-1).*(rho.^2 + rhoP.^2 -
2*rho.*rhoP.*cos(phiP)).^((1-2)/2);
I1b = triplequad(F1,2.00585285,pi,a,b,a,b,[],@quadv);
I1=I1a+I1b;


G = @(phiP,rhoP,rho) (cos(phiP)).*(rho.^2 + rhoP.^2 -
2*rho.*rhoP.*cos(phiP)).^((3-2)/2);
I3 = triplequad(G,0,pi,a,b,a,b,[],@quadv);

% I1=0.011408150843872;
% I3=-3.699764668971378e-07;

 %--------for 10 terms------------------
G2 = @(phiP,rhoP,rho) (cos(phiP)).*(rho.^2 + rhoP.^2 -
2*rho.*rhoP.*cos(phiP)).^((2-2)/2);
I2 = triplequad(G2,0,pi,a,b,a,b,[],@quadv);
```

```
G4 = @(phiP,rhoP,rho) (cos(phiP)).*(rho.^2 + rhoP.^2 -
2*rho.*rhoP.*cos(phiP)).^((4-2)/2);
I4 = triplequad(G4,0,pi,a,b,a,b,[],@quadv);

G5 = @(phiP,rhoP,rho) (cos(phiP)).*(rho.^2 + rhoP.^2 -
2*rho.*rhoP.*cos(phiP)).^((5-2)/2);
I5 = triplequad(G5,0,pi,a,b,a,b,[],@quadv);

G6 = @(phiP,rhoP,rho) (cos(phiP)).*(rho.^2 + rhoP.^2 -
2*rho.*rhoP.*cos(phiP)).^((6-2)/2);
I6 = triplequad(G6,0,pi,a,b,a,b,[],@quadv);

G7 = @(phiP,rhoP,rho) (cos(phiP)).*(rho.^2 + rhoP.^2 -
2*rho.*rhoP.*cos(phiP)).^((7-2)/2);
I7 = triplequad(G7,0,pi,a,b,a,b,[],@quadv);

G8 = @(phiP,rhoP,rho) (cos(phiP)).*(rho.^2 + rhoP.^2 -
2*rho.*rhoP.*cos(phiP)).^((8-2)/2);
I8 = triplequad(G8,0,pi,a,b,a,b,[],@quadv);

G9 = @(phiP,rhoP,rho) (cos(phiP)).*(rho.^2 + rhoP.^2 -
2*rho.*rhoP.*cos(phiP)).^((9-2)/2);
I9 = triplequad(G9,0,pi,a,b,a,b,[],@quadv);

G10 = @(phiP,rhoP,rho) (cos(phiP)).*(rho.^2 + rhoP.^2 -
2*rho.*rhoP.*cos(phiP)).^((10-2)/2);
I10 = triplequad(G10,0,pi,a,b,a,b,[],@quadv);

G11 = @(phiP,rhoP,rho) (cos(phiP)).*(rho.^2 + rhoP.^2 -
2*rho.*rhoP.*cos(phiP)).^((11-2)/2);
I11 = triplequad(G11,0,pi,a,b,a,b,[],@quadv);

G12 = @(phiP,rhoP,rho) (cos(phiP)).*(rho.^2 + rhoP.^2 -
2*rho.*rhoP.*cos(phiP)).^((12-2)/2);
I12 = triplequad(G12,0,pi,a,b,a,b,[],@quadv);

G13 = @(phiP,rhoP,rho) (cos(phiP)).*(rho.^2 + rhoP.^2 -
2*rho.*rhoP.*cos(phiP)).^((13-2)/2);
I13 = triplequad(G13,0,pi,a,b,a,b,[],@quadv);

G14 = @(phiP,rhoP,rho) (cos(phiP)).*(rho.^2 + rhoP.^2 -
2*rho.*rhoP.*cos(phiP)).^((14-2)/2);
I14 = triplequad(G14,0,pi,a,b,a,b,[],@quadv);

G15 = @(phiP,rhoP,rho) (cos(phiP)).*(rho.^2 + rhoP.^2 -
2*rho.*rhoP.*cos(phiP)).^((15-2)/2);
I15 = triplequad(G15,0,pi,a,b,a,b,[],@quadv);

G16 = @(phiP,rhoP,rho) (cos(phiP)).*(rho.^2 + rhoP.^2 -
2*rho.*rhoP.*cos(phiP)).^((16-2)/2);
I16 = triplequad(G16,0,pi,a,b,a,b,[],@quadv);
```

```
G17 = @(phiP,rhoP,rho) (cos(phiP)).*(rho.^2 + rhoP.^2 -
2*rho.*rhoP.*cos(phiP)).^((17-2)/2);
I17 = triplequad(G17,0,pi,a,b,a,b,[],@quadv);

G18 = @(phiP,rhoP,rho) (cos(phiP)).*(rho.^2 + rhoP.^2 -
2*rho.*rhoP.*cos(phiP)).^((18-2)/2);
I18 = triplequad(G18,0,pi,a,b,a,b,[],@quadv);

G19 = @(phiP,rhoP,rho) (cos(phiP)).*(rho.^2 + rhoP.^2 -
2*rho.*rhoP.*cos(phiP)).^((19-2)/2);
I19 = triplequad(G19,0,pi,a,b,a,b,[],@quadv);

G20 = @(phiP,rhoP,rho) (cos(phiP)).*(rho.^2 + rhoP.^2 -
2*rho.*rhoP.*cos(phiP)).^((20-2)/2);
I20 = triplequad(G20,0,pi,a,b,a,b,[],@quadv);

G21 = @(phiP,rhoP,rho) (cos(phiP)).*(rho.^2 + rhoP.^2 -
2*rho.*rhoP.*cos(phiP)).^((21-2)/2);
I21 = triplequad(G21,0,pi,a,b,a,b,[],@quadv);
%% ---------------------------------------------------

 %% -----------LOAD FILES S11 and Permittivty file --------------
% % freq = importdata('C:\Users\gradym\Documents\coax probe\1-19-12\s11
data\DATA01.D1', ' ', 6);
int = 1:126;
Range_s11=int;
Range=Range_s11;
Range_perm=1:801;


L1a=importdata('J:\PhD Research Under Shake Daddy\Antenna and Probe Sim
and Meas Results\Micro-Coaxial Probe\Sim Probe Data\Characterizing
Materials\Air.csv', ',', 1);

freq=L1a.data(:,:);
freq=freq(Range,1);
freq2=linspace(min(freq),max(freq),801);
w=2*pi.*freq2*1e9;

Air1_1=L1a.data(:,:); %load s11

L2a=importdata('J:\PhD Research Under Shake Daddy\Antenna and Probe Sim
and Meas Results\Micro-Coaxial Probe\Sim Probe Data\Characterizing
Materials\R03006m.csv', ',', 1);
Styr1_1=L2a.data(:,:); %load S11




L3a=importdata('J:\PhD Research Under Shake Daddy\Antenna and Probe Sim
and Meas Results\Micro-Coaxial Probe\Sim Probe Data\Characterizing
Materials\R03010m.csv', ',', 1);
Tef1_1=L3a.data(:,:); %s11
```

```
L4a=importdata('J:\PhD Research Under Shake Daddy\Antenna and Probe Sim
and Meas Results\Micro-Coaxial Probe\Sim Probe Data\Characterizing
Materials\PDMSm.csv', ',', 1);
Meas_1=L4a.data(:,:); %s11

L1a=importdata('J:\Cal Standards2\measured perm\FR-4_1_a.s1p', ' ', 1);
Air1_1p=L1a.data(:,:); %load permittivty
L1b=importdata('J:\Cal Standards2\measured perm\RO3006_1_a.s1p', ' ',
1);
Tef1_1p=L1b.data(:,:); %load permittivty
L2a=importdata('J:\Cal Standards2\measured perm\RO3010_1_a.s1p', ' ',
1);
Styr1_1p=L2a.data(:,:); %load permittivty

%% -------random constants--------------------------
c=3e8;
k = w./c;
eps_0=8.854e-12;
mu_0=4*pi*10^-7;
eta=sqrt(mu_0/eps_0);
k0=w*sqrt(mu_0*eps_0);
% eps_c=2;
Yo=2*pi/(log(b/a)*sqrt(mu_0/(eps_c*eps_0)));
Zo=1./Yo;
% Zo=50;
% Yo=1/Zo;
 %%-------------------------------------------------------
 %% ---------------NAME REFS MEAS S11 and permittivty-------------
%---------S11---------
Air1_1=Air1_1(Range,1)+j.*Air1_1(Range,2);
Styr1_1=Styr1_1(Range,1)+j.*Styr1_1(Range,2);
Tef1_1=Tef1_1(Range,1)+j.*Tef1_1(Range,2);
Meas_1=Meas_1(Range,1)+j.*Meas_1(Range,2);

pp1r = spline(freq,real(Air1_1))
yy1r = ppval(pp1r, linspace(min(freq),max(freq),801));
pp1i = spline(freq,imag(Air1_1))
yy1i = ppval(pp1i, linspace(min(freq),max(freq),801));

pp2r = spline(freq,real(Styr1_1))
yy2r = ppval(pp2r, linspace(min(freq),max(freq),801));
pp2i = spline(freq,imag(Styr1_1))
yy2i = ppval(pp2i, linspace(min(freq),max(freq),801));

pp3r = spline(freq,real(Tef1_1))
yy3r = ppval(pp3r, linspace(min(freq),max(freq),801));



pp3i = spline(freq,imag(Tef1_1))
yy3i = ppval(pp3i, linspace(min(freq),max(freq),801));

ppmr = spline(freq,real(Meas_1))
yymr = ppval(ppmr, linspace(min(freq),max(freq),801));
```

```
ppmi = spline(freq,imag(Meas_1))
yymi = ppval(ppmi, linspace(min(freq),max(freq),801));

Air1_1=yy1r-j.*yy1i;
Styr1_1=yy2r-j.*yy2i;
Tef1_1=yy3r-j.*yy3i;
Meas_1=yymr-j.*yymi;

% -----REFS S11----------------
GamRef1=Air1_1; %real +j*imag
GamRef2=Tef1_1;    %real +j*imag
GamRef3=Styr1_1;   %real +j*imag

%----MEASURED S11-------------
GamMeas1 = Meas_1; %real +j*imag

%---------permittivyty--------------
Air1_1p=Air1_1p(Range_perm,2)-j.*Air1_1p(Range_perm,3);
Styr1_1p=Styr1_1p(Range_perm,2)-j.*Styr1_1p(Range_perm,3);
Tef1_1p=Tef1_1p(Range_perm,2)-j.*Tef1_1p(Range_perm,3);

%--------REFS permittivty-----------------
epsRef1=Air1_1p.';
epsRef2=Styr1_1p.';
epsRef3=Tef1_1p.';
%% ---------------------------------

 %% --------CALCULATING ADMITTANCE EXPRESSION--------------------
%%----------for newtonral-------only 3 terms--------
const1= (1i.*w.*2)./((log(b/a))^2);
const2= const1.*(w.^2).*mu_0./2;
const3=(pi/12)*w.^4.*mu_0^(3/2).*((b^2-a^2)/(log(b/a))).^2;
A=const3*eps_0.^(5/2);
B=const2.*I3*eps_0.^2;
C=const1.*I1*eps_0;
%%-------------------------------------

%%----------for newtonral_full-------10 terms--------
C0=(2.*w)./((log(b/a))^2);
C1 = 1i.*I1.*w.^0.*mu_0^0.*eps_0^1;
C3 =(1i.*I3.*w.^2.*mu_0^1.*eps_0^2)./(2*1);
C5 =(1i.*I5.*w.^4.*mu_0^2.*eps_0^3)./(4*3*2*1);
C7 =(1i.*I7.*w.^6.*mu_0^3.*eps_0^4)./(6*5*4*3*2*1);
C9 =(1i.*I9.*w.^8.*mu_0^4.*eps_0^5)./(8*7*6*5*4*3*2*1);
C11=(1i.*I11.*w.^10.*mu_0^5.*eps_0^6)./(10*9*8*7*6*5*4*3*2*1);



C13=(1i.*I13.*w.^12.*mu_0^6.*eps_0^7)./(12*11*10*9*8*7*6*5*4*3*2*1);
C15=(1i.*I15.*w.^14.*mu_0^7.*eps_0^8)./(14*13*12*11*10*9*8*7*6*5*4*3*2*
1);
C17=(1i.*I17.*w.^16.*mu_0^8.*eps_0^9)./(16*15*14*13*12*11*10*9*8*7*6*5*
4*3*2*1);
```

```
C19=(1i.*I19.*w.^18.*mu_0^9.*eps_0^10)./(18*17*16*15*14*13*12*11*10*9*8
*7*6*5*4*3*2*1);
C21=(1i.*I21.*w.^20.*mu_0^10.*eps_0^11)./(20*19*18*17*16*15*14*13*12*11
*10*9*8*7*6*5*4*3*2*1);
C2=(I2.*w.^1.*mu_0.^(1/2).*eps_0^(3/2))./(1);
C4=(I4.*w.^3.*mu_0.^(3/2).*eps_0^(5/2))./(3*2*1);
C6=(I6.*w.^5.*mu_0.^(5/2).*eps_0^(7/2))./(5*4*3*2*1);
C8=(I8.*w.^7.*mu_0.^(7/2).*eps_0^(9/2))./(7*6*5*4*3*2*1);
C10=(I10.*w.^9.*mu_0.^(9/2).*eps_0^(11/2))./(9*8*7*6*5*4*3*2*1);
C12=(I12.*w.^11.*mu_0.^(11/2).*eps_0^(13/2))./(11*10*9*8*7*6*5*4*3*2*1)
;
C14=(I14.*w.^13.*mu_0.^(13/2).*eps_0^(15/2))./(13*12*11*10*9*8*7*6*5*4*
3*2*1);
C16=(I16.*w.^15.*mu_0.^(15/2).*eps_0^(17/2))./(15*14*13*12*11*10*9*8*7*
6*5*4*3*2*1);
C18=(I18.*w.^17.*mu_0.^(17/2).*eps_0^(19/2))./(17*16*15*14*13*12*11*10*
9*8*7*6*5*4*3*2*1);
C20=(I20.*w.^19.*mu_0.^(19/2).*eps_0^(21/2))./(19*18*17*16*15*14*13*12*
11*10*9*8*7*6*5*4*3*2*1);

%% ------------------------------------

 %% -------CALCULATE PERMITTIVITY----------------

% % % %%%-----------------3 standards-----FULL ADMITTANCE FORMULA------
------------
% % % % %
[D]=Stand_3(A,B,C,epsRef1,epsRef2,epsRef3,GamMeas,GamRef1,GamRef2,GamRe
f3)
% % %
[D,Y1,Y2,Y3]=Stand_3_full(C0,C1,C2,C3,C4,C5,C6,C7,C8,C9,C10,C11,C12,C13
,C14,C15,C16,C17,C18,C19,C20,C21,epsRef1,epsRef2,epsRef3,GamMeas1,GamRe
f1,GamRef2,GamRef3)
% % % x_guess=300+1i*400; errorNUM=1e-12;
% % % % [x_new]=newtonral(A,B,C,D,x_guess,errorNUM);
% % %
[x_new,f,error]=newtonral_full2(C0,C1,C2,C3,C4,C5,C6,C7,C8,C9,C10,C11,C
12,C13,C14,C15,C16,C17,C18,C19,C20,C21,D,x_guess,errorNUM)
% % % % x_new1=x_new;
% % % plotfig(x_new,w)

%%%%-----------------3 standards-----------------------
% %
[D]=Stand_3(A,B,C,epsRef1,epsRef2,epsRef3,GamMeas,GamRef1,GamRef2,GamRe
f3)
[D,Y1,Y2,Y3]=Stand_3(A,B,C,epsRef1,epsRef2,epsRef3,GamMeas1,GamRef1,Gam
Ref2,GamRef3)
x_guess=300+1i*400; errorNUM=1e-20;
[x_new]=newtonral(A,B,C,D,x_guess,errorNUM);
%
[x_new]=newtonral_full(C0,C1,C2,C3,C5,C6,C7,C8,C9,C10,D,x_guess,errorNU
M)
% plotfig(x_new,w)
figure
```

```
plot(freq2,real(x_new))
title('freq vs real permittivyt')
figure
plot(freq2,-imag(x_new))
title('freq vs imag permittivyt')

Get_Data=[freq2.' real(x_new) (-imag(x_new))]
%% --------------------------
```

Appendix D: CPW-Fed Folded Dipole Slot Antenna Used for Millimeter Wave Device Characterization

D1. ANTENNA DESIGN

D1.1 Antenna Layout

The layout of the folded dipole slot antenna is shown in Figure D1. The design and simulation of the antenna structure was performed using Agilent's Momentum Electromagnetic Simulator, which combines full-wave and quasi-static electromagnetic solvers for antenna modeling. A high resistive silicon substrate with infinite surface area was assumed for simulation purpose.

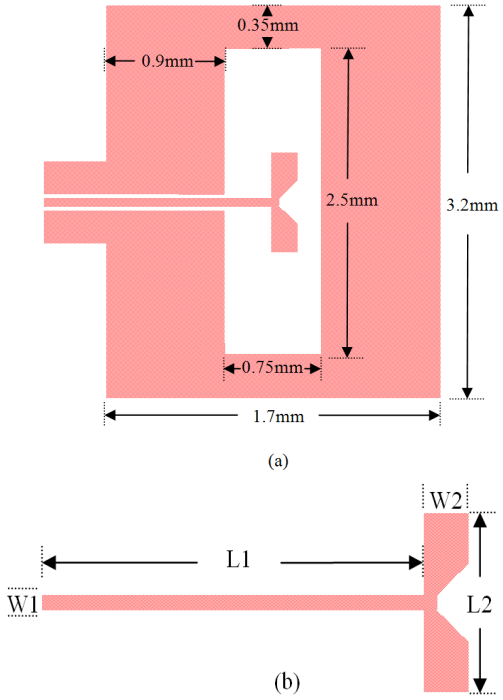

Figure D.1 Momentum layout of (a) 60 GHz slot antenna in membrane and (b) folded dipole antenna.

The dimensions of the ground plane are 2.2 λ_{eff} x 1.78 λ_{eff} or 3.2 mm x 2.6 mm; where λ_{eff} is the effective wavelength of silicon at 60 GHz. By adjusting these dimensions, the antenna can be scaled down to achieve resonance at higher frequencies. The slot antenna was designed 0.24

λ_{eff} (0.35 mm) x 0.63 λ_{eff} (0.9 mm) deep inside the ground plane to include the folded dipole structure (Figure D1a). The dimensions of the slot are 2.5 mm (1.7 λ_{eff}) long and 0.75 mm (0.5 λ_{eff}) wide. These dimensions were chosen in the final design because they provided the best performance and allowed the antenna to resonate at 60 GHz. The slot was adjusted to match the input impedance to 50 Ω and to control the additional resonances that appeared at higher frequencies. Although this design was focused on a single frequency operation, additional resonances could also be achieved by changing the dimension for systems requiring multiband operations [19].

D1.2 Folded Dipole

Figure D1 (b) illustrates the layout of the folded dipole and its dimensions. The folded dipole structure was integrated in the slot to improve the bandwidth of the antenna. By designing the dipole to operate at 60 GHz and altering the dimensions of the slot, the radiation was compressed and the antenna achieved wideband performance. The dimensions of the dipole are L1 = 1.8mm, L2 = 0.8mm, W1 = .07mm, and W2 = 0.2mm; where W1 is the width of the dipole leg, W2 is the width of the dipole arm, and L1 and L2 is the length of the arm and leg. The V-groove in the center of the dipole arm is 0.2mm in length at 45˚ angles. The groove was designed by adjusting its length and angle to achieve a wider bandwidth. The width of the dipole leg also served as the width of the CPW signal line. The length was adjusted to determine the optimal distance needed between the slot edge and the dipole arm; which allowed the signal to propagate through the dipole and not along the edges of the slot, as confirmed by the simulation results.

D1.3 CPW-to-CPW Line Transition

To reduce the propagation of surface waves present in the substrate at mm-wave frequencies, the antenna was fabricated on a 50 μm silicon membrane. This method helped improve the bandwidth and efficiency of the antenna. However, it developed the need for a CPW transition from a thicker part of the substrate to the membrane, in this case a 250 μm to 50 μm, to enable any device testing. Figure D2 illustrates the layout of the line transition. The CPW's gap distance decreased as the substrate thickness changed from 250 μm to 50 μm, since the CPW dimensions are based on the thickness of the substrate. The dimensions of the feed line are G = 37.3 μm and W = 70 μm, corresponding to a characteristics impedance of 50 Ω, where G is the gap distance between lines and W is the width of the signal line. The dimensions of the CPW in the membrane are G = 31.3 μm and W = 70 μm corresponding to a characteristics impedance of 50 Ω. To account for the etch profile of the silicon membrane, the ground planes of the CPW line included a step topology as shown in Figure D2 to minimize the reflections present at the discontinuity. These reflections can give birth to higher order modes, which are undesirable at the measurement's reference plane.

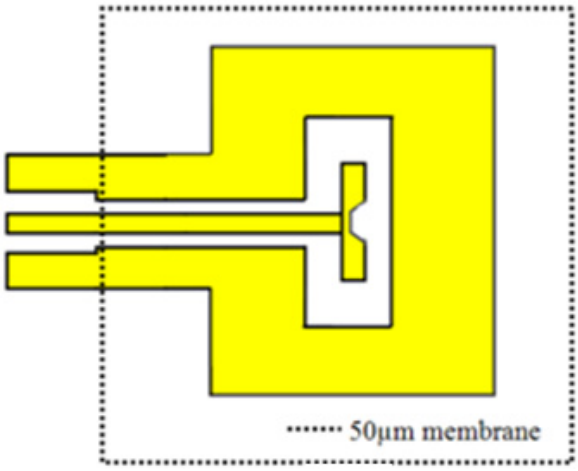

Figure D.2 60 GHz elements on a 50 μm silicon membrane including folded dipole slot antenna with transition.

D2. Fabrication Methods

The folded dipole slot antennas were realized on a 4" and a 250 μm thick silicon substrate. Figure D3 illustrates the steps involved in fabricating the mm-wave antenna. Initially, silicon substrate was thermally oxidized to grow a 1 μm thick SiO_2 layer. Since the oxidation layer was required only on the membrane etch side, the oxide layer was chemically etched on the other side. While the oxidized side provided as an etch protective layer during the micromachining process, the un-oxidized side served as the ground plane for the antenna. Following the oxide etch process, a photolithography step was performed to pattern the antenna and CPW configuration pads on the substrate. Then, a thin layer of chromium (Cr) and gold (Au) were deposited on the substrate. Cr was deposited with a thickness of ~ 30 nm and acted as an adhesion layer for the top Au (~300 nm) layer. After the contact pads were made, photolithography was performed on the backside of the substrate and windows were opened underneath the devices. The substrate was then subjected to a dry etching process, to micro-machine the backside from 250 μm to 50 μm. Figure D4 (a) and (b) shows the microscopic image of the fabricated antenna and the membranes etched beneath the antenna in silicon, respectively.

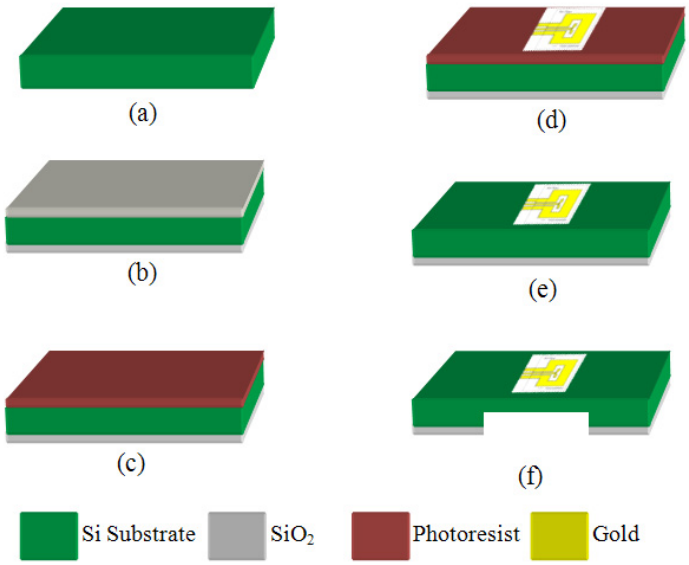

Figure D.3 Schematic of the process sequence followed to develop the slot antenna on a silicon membrane. (a) Si substrate, (b) SiO2 grown on the substrate, (c) photoresist deposited for patterning, (d) Pattern transfer by photolithography, (e) Thermal evaporation and photoresist removal, (f) create a window and dry etch bulk silicon.

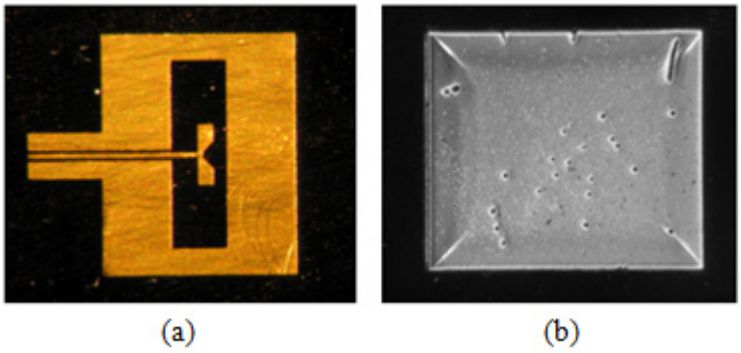

Figure D.4 Schematic representing (a) a 60 GHz folded dipole slot antenna on silicon and (b) a view of the silicon membrane etched beneath the antenna structure.

D3. MEASUREMENT TECHNIQUES AND RESULTS

D3.1 Test Set-up

The antenna was measured using a Karl Suss PA200 probe station with 150 μm pitch probes. The reflection coefficient was determined using an Anritsu 37397 vector network

analyzer (VNA), capable of measuring up to 64 GHz. A V-band cable was used to connect the VNA to the probe station and to communicate the reflection data. The V-cable was calibrated using a CS-5 calibration kit.

D3.2 Reflection Measurement

The simulated vs. measured reflection coefficient data of the antenna is illustrated in Figure D5. The figure shows that at 62 GHz, the antenna is well matched to 50Ω with a reflection coefficient of -45 dB. An additional resonance appeared at 55 GHz, which is contributed, to the antenna structure achieving multi-band operations. By minimizing the membrane thickness, additional surface waves were reduced and the antenna achieved a bandwidth of 25% at S11<-10 dB; improving the performance of previous silicon micromachined antennas [17, 18]. The antenna operates over a wideband from 50 to 64 GHz, proving its ability to be used in WLAN and V-band frequency applications. The discrepancy between data can be contributed to a variance in membrane thickness and losses caused by surface waves present during measuring.

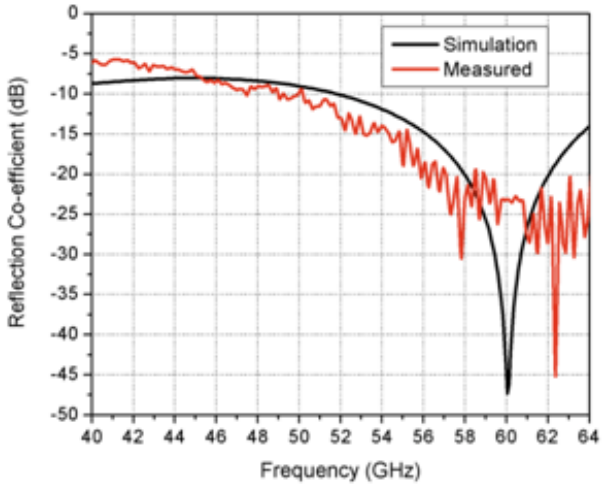

(a)

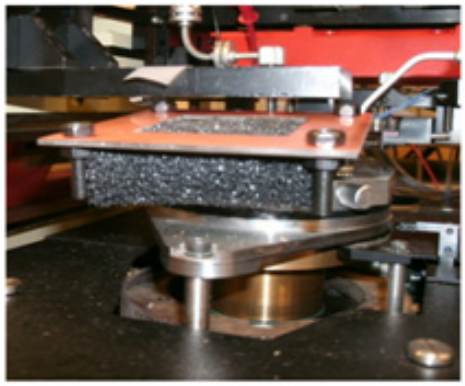

(b)

Figure D.5 (a) Measured vs. simulated reflection coefficient of the folded dipole slot antenna with CPW-to-CPW transition and (b) setup using high frequency absorber to separate the antenna from the metal chuck.

Figure D5 (b) shows the broadband absorber [20] used during measurement to reduce any wave disruptions caused by the antenna resting on the metal chuck of the probe station. The substrate was removed from the chuck by placing it on a lifted FR-4 board that included an air gap directly under the membrane. The absorber was then placed in between the membrane and chuck to close the gap. By creating space between the substrate and metal, the fabricated antenna operated at the desired frequency.

D3.3 Effect of Eccosorb™ on Metal Chuck

When the antenna was measured directly on the metal chuck, its performance decreased causing it to resonate at a lower frequency. This occurred due to the effects of side lobes which surfaced as the antenna became vulnerable to wave disruption caused by the metal chuck. These side lobes forced the antenna to radiate with a lesser degree of accuracy and directivity. To ensure the antenna achieved maximum radiation, ECCOSORB™ HR-25 was recommended to eliminate all reflections produced by the metal chuck [21]. This broadband microwave absorber helped reduce interference between metals and eliminated all side lobes. Figure D6 below illustrates the variation in reflection co-efficient measurement of the antenna on the metal chuck as compared to the antenna 9645 ured with Eccosorb™.

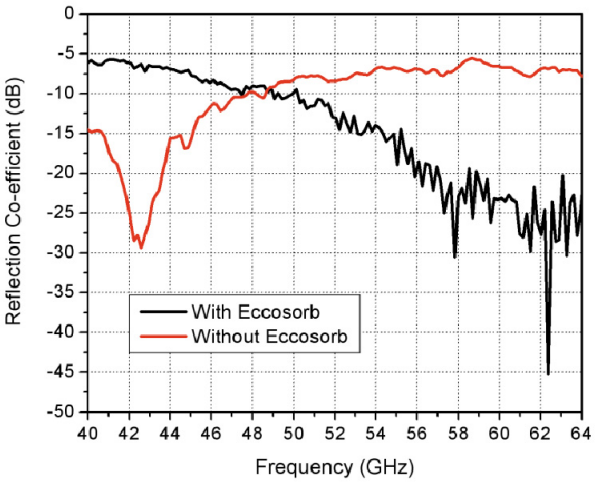

Figure D.6 Measured reflection coefficient with and without eccosorb placed on the metal chuck.

It can be observed from Figure D6 that without the absorber, the antenna resonated at ~42 GHz proving the metal disrupted the antennas behavior at high frequencies. However, when implementing the setup shown in Figure D5 (b), the frequency shifted from 42 to ~62 GHz. Therefore, by resting the antenna on a linear surface and placing the absorber directly under the antenna, a better impedance match at the desired frequency was achieved.

D3.4 Radiation Pattern

The antenna's radiation pattern was measured using a portable probe station. The fabricated antenna was fed by a 60 GHz Gunn oscillator, which provided the radiation source. The Gunn oscillator was operated using an external power source. A standard horn antenna operating from 50 – 75 GHz was used as the receiving antenna. The horn antenna was connected to an Agilent 8565EC Spectrum Analyzer using a HP11970V harmonic mixer extending the frequency range of the spectrum analyzer from 50 to 75 GHz. A custom made semi-circular guiding fixture was used to track the radiation of the fabricated antenna from 0° to 180°, while supporting the receiving horn antenna and the mixer. The horn antenna was placed parallel to the antenna feed line to trace the co-polarized radiation pattern. The power received by the horn was

recorded in the spectrum analyzer at every 10°. Figure D7 below illustrates the setup used to measure the radiation pattern. The pattern was measured in an anechoic chamber but the image was taken outside of it for proper lighting.

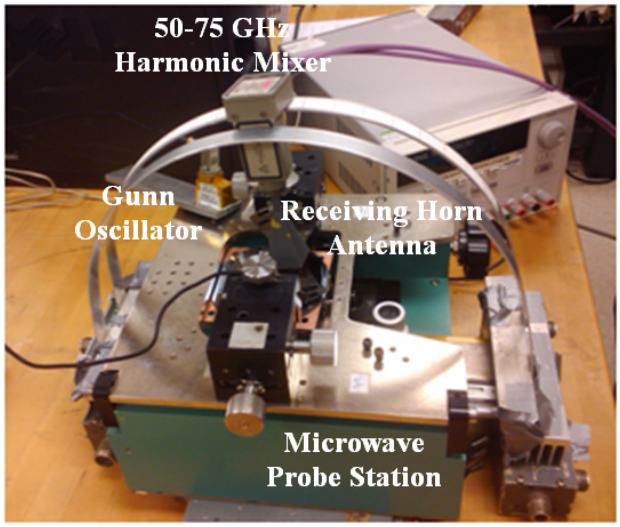

Figure D.7 Radiation pattern measurement setup used for folded dipole slot antenna.

Results obtained during the radiation pattern measurement are shown in Figure D8 below. The measured results are in good agreement with those achieved during simulation. The maximum co-polarization magnitude achieved was -8 dB at 0° with a gain of 4.1 dBi. This pattern behaves as a dipole because the pattern achieves maximum radiation at 0˚ and drops off to minimum radiation on the antenna's axis. However, the slight difference in magnitudes of the measured vs. simulated patterns is due to inaccuracies during the measuring setup which requires precise positioning of the receiving antenna and stability in the angle guiding structure.

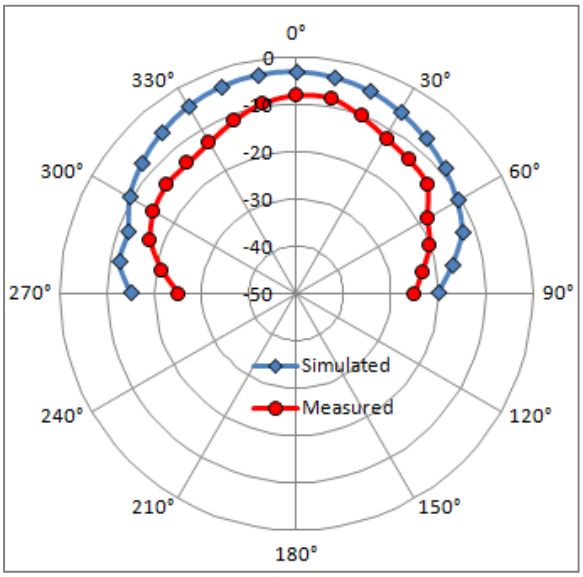

Figure D.8 Measured vs. Simulated Co-Polarized E-plane radiation pattern (dB) of the 60 GHz antenna.

D4. Conclusion

A 60 GHz CPW-fed folded dipole slot antenna micromachined on a 50 µm silicon membrane was presented. By fabricating the 60 GHz antenna on a thin substrate, the propagation of surface waves and dominating side lobes were reduced. The antenna provided excellent results by achieving a reflection coefficient of -45 dB with a bandwidth of 25% at -10 dB. The inclusion of a high frequency absorber (Eccosorb™) eliminated wave disruptions created by the metal surface. The antenna demonstrated an omnidirectional radiation pattern, which agreed well the behavior of a dipole antenna. These results indicate the antenna's ability to be scaled down and used in extremely high frequency operations and integrate with current wireless networking systems.

VITA

JUSTIN BOONE

Born, Port Arthur, Texas

2005-2009	B.S., Electrical Engineering Southern University A&M College Baton Rouge, Louisiana
2009-2011	M.S., Electrical Engineering University of South Florida Tampa, Florida
2011-2013	Doctoral Candidate Florida International University Miami, Florida

PUBLICATIONS AND PRESENTATIONS

Justin Boone, Subramanian Krishnan, Shekhar Bhansali, "Development of a through wafer 3D vertical micro-coaxial probe." J. Micromech. Microeng. 23 (2013) 075029.

Justin Boone, Subramanian Krishnan, Shekhar Bhansali**.** "Silicon Based Vertical Micro-Coaxial Transition for High Frequency Packaging Technologies." *Progress in Electromagnetics Research B*, vol. 50, pp. 1-17, 2013.

J. Boone, S. Krishnan, Shekhar Bhansali, Elias Stefanakos, Yogi Goswami, "CPW-fed Folded Dipole Slot Antenna for WLAN Applications and V-band Frequency Operations." *IET Journals-Microwave Antennas & Propagation,* vol. 6, pp. 583-587, 2012.

S. Krishnan, **J. Boone**. "Membrane Supported CPW-Fed Wideband Slot Antenna for Millimeter Wave Applications." *Progress in Electromagnetics Research C*, vol. 28, 15-26, 2012.